Scuola Superiore Meridionale

University of Naples Federico II

Ph. D. in Molecular Sciences for Earth and Space

SSM

Scuola Superiore Meridionale

Stability and interaction determinants of biomolecules in the harsh conditions of the solar system

Supervisors

Prof. Concetta Giancola

Prof. Luigi Petraccone

Ph.D candidate

Attila Tortorella

XXXVII Cycle

Summary

Life's persistence depends on the ability of biomolecules to preserve structure, stability, and function under variable physicochemical conditions. Investigating how these processes occur in environments beyond terrestrial standards provides critical insight into the molecular boundaries of habitability. This PhD thesis examines how temperature, ionic composition, hydration and pressure affect the organization and energetics of biological macromolecules under Martian-like aqueous conditions, with the goal of identifying the physicochemical principles that enable molecular adaptation in extreme or extraterrestrial environments. Chapter 2 focuses on the behaviour of model bacterial membranes composed of phosphatidylethanolamine (PE) and phosphatidylglycerol (PG) in the presence of perchlorate and sulphate salts, both abundant in the Martian regolith. Using spectroscopic and calorimetric techniques, the effects of these salts on bilayer stability, phase behaviour, and fluidity were characterized. The results revealed that perchlorates favour the physiologically relevant fluid phase in the presence of high pressure, suggesting that a prototypical bacterium could thrive in such conditions. Remarkably, even in concentrated brines, PE/PG membranes maintained their integrity and exhibited reversible thermotropic transitions, demonstrating that simple phospholipid bilayers can remain stable under saline conditions analogous to those expected for Mars. Chapter 3 explores molecular recognition processes through a detailed thermodynamic characterization of the lysozyme–NAG3 complex as a model of protein–ligand interaction. Isothermal titration calorimetry and complementary spectroscopic analyses revealed that Martian-relevant salts modulate binding energetics primarily through hydration effects. Perchlorate ions weaken binding affinity by competitive inhibition, whereas other salts preserve binding. In all cases, a pronounced enthalpy–entropy

compensation was observed, indicating that hydration rearrangements mitigate environmental perturbations and confer molecular resilience in high-salinity media. Finally, Chapter 4 investigates the interactions between model lipid membranes and G-quadruplex (G4) nucleic acid structures. These non-canonical nucleic acids were selected because of their exceptional thermodynamic stability under harsh conditions, including elevated temperature and high ionic strength. Given their intrinsic robustness, it is reasonable to hypothesize that such structures could have persisted in prebiotic environments and interacted with primitive membranes, potentially contributing to the molecular organization processes that preceded the emergence of microbial life. Experimental analyses demonstrated that both DNA and RNA G4s associate with zwitterionic membranes, while only RNA G4s display measurable binding to anionic membranes. Isothermal titration calorimetry revealed distinct thermodynamic mechanisms for DNA and RNA binding, reflecting differences in backbone chemistry and hydration dynamics. Furthermore, G4s preferred gel-phase membranes over fluid-phase ones, underscoring the role of membrane phase in this type of interaction. These findings suggest that prototypical biological membranes could have actively modulated the structure, stability, and organization of nucleic acids, influencing molecular evolution at the interface between chemistry and biology. In summary, this PhD thesis demonstrates that essential biological processes, compartmentalization, molecular recognition, and information storage, can persist under a wide range of non-terrestrial conditions. The results delineate the molecular strategies that underlie thermodynamic resilience and highlight membrane-associated systems as robust chemical frameworks capable of sustaining life in extraterrestrial aqueous environments.

Contents

Chapter 1 - Introduction

The study of biomolecular behaviour under varying physical and chemical conditions constitutes a central objective of contemporary biophysics[1–8]. Proteins, nucleic acids, and membranes are dynamic assemblies whose structural and functional integrity arises from a finely balanced interplay of electrostatic, hydrophobic, hydrogen-bonding, and van der Waals interactions. These forces determine molecular stability and activity and, consequently, the ability of living systems to persist across diverse environmental conditions. From the scale of single molecules to entire ecosystems, the persistence of biological function under extreme conditions illustrates the capacity of matter to organize itself into adaptive systems [4,9–12]. Investigations of biomolecules in non-standard environments, characterized by low temperatures, high salt concentrations, high pressure, non-neutral pH or intense radiation, clarify the molecular basis of this adaptability and delineate the physicochemical limits compatible with life[13–20]. Such analyses serve dual purposes: they provide insight into the molecular mechanisms that enable survival in terrestrial extreme habitats and supply analogue frameworks for astrobiology, defining the possible biochemical boundaries of life beyond Earth. sBiological membranes and protein–ligand interactions occupy a central role in this context: they form the physical interfaces that mediate exchange, recognition, and communication at the cellular level [21–23]. For this reason, the following paragraphs will provide a detailed description of both systems. Moreover, the early Earth presented environmental conditions that can be considered extreme by modern standards. Thus, under such circumstances, the role of prototypical biological membranes in modulating the structure and stability of nucleic acids

could have been relevant, providing protection, compartmentalization, and organization within primitive environments. This hypothesis will be discussed in a dedicated paragraph.

1.1 Extreme Environments and Adaptation Mechanisms

1.1.1 Boundaries of life

Life on Earth exists across an extensive range of physical and chemical parameters[8,17,24–27]]. Microorganisms have been identified in hydrothermal systems exceeding 100 °C[28], in polar ice at subzero temperatures[29,30], in hypersaline lakes with salt concentrations above 30 % [31], and in acidic or alkaline waters with pH values below 1[32] or above 10[33,34]. These extremophiles redefine the known biochemical limits and demonstrate that molecular systems can maintain stability and activity under conditions once thought to be incompatible with life. Organisms are tipically classified according to the dominant environmental stress they tolerate: *thermophiles* and *psychrophiles* adapt to high and low temperatures, respectively; *halophiles* thrive in hypersaline settings; *acidophiles* and *alkaliphiles* in extreme pH; *barophiles* (or *piezophiles*) in high-pressure habitats; and *radiophiles* in high-radiation environments[3,35]. Each group exhibits specific molecular adaptations that preserve the balance between structural stability and functional flexibility. The biochemical limits of life are determined not by a single factor but by the interaction of multiple stressors[36]. On Mars, for example, low temperature, desiccation, high pressure, high salinity, and ultraviolet radiation act simultaneously, producing an extreme multi-stress

regime under which only highly specialized molecular adaptations could sustain biochemical activity[37,38]. Analysis of these adaptations provides a biophysical framework for assessing the potential of extraterrestrial environments to support life.

1.1.2 Molecular mechanisms of adaptation

Adaptation at the molecular level relies on several strategies that preserve structure and function under stress while maintaining the dynamic properties required for catalysis and regulation. A summary of typical adaption mechanisms is presented below.

Protein stability. Temperature and salinity strongly influence protein folding. In thermophilic organisms, stability arises from increased numbers of ionic interactions, enhanced hydrophobic packing, and more compact cores. Psychrophilic proteins display greater flexibility, achieved through a higher proportion of glycine and serine residues and reduced hydrophobicity, which maintain catalytic activity at low temperatures. Halophilic proteins must remain soluble in highly concentrated salt solutions that disrupt hydration shells and electrostatic interactions. Their surfaces are typically enriched in acidic residues, producing strong hydration and electrostatic compatibility with surrounding ions[39–41].

Membrane fluidity and lipid composition. Environmental parameters such as temperature, pressure, and ionic strength directly affect membrane phase behaviour. To maintain proper viscosity and permeability, cells adjust the ratio of saturated to unsaturated fatty acids and alter the headgroup composition of

phospholipids. Psychrophiles incorporate unsaturated and short-chain fatty acids to prevent solidification of membranes, whereas thermophiles employ longer, more saturated chains or ether-linked lipids to avoid excessive fluidity. Archaeal membranes composed of isoprenoid ether lipids frequently form monolayers that remain stable at temperatures above 100 °C [1,42–45].

Compatible solutes and chaperones. Small organic molecules such as trehalose, glycine betaine, and proline accumulate in extremophiles as protective solutes that stabilize proteins and membranes without interfering with metabolism. Molecular chaperones and heat-shock proteins similarly prevent aggregation and assist in refolding, preserving proteostasis under stress [46,47].

Nucleic-acid protection. Extreme temperature, radiation, and chemical stress threaten genomic integrity. Thermophiles stabilize DNA through specialized binding proteins, whereas radiophiles such as *Deinococcus radiodurans* employ efficient DNA-repair systems supported by manganese-dependent antioxidant mechanisms. These mechanisms illustrate a universal adaptive principle: evolutionary selection favours physicochemical robustness achieved through dynamic flexibility, enabling biological macromolecules to function despite environmental variability[48–50].

1.2 Biological Membranes

1.2.1 Structure and organization

Biological membranes form the fundamental physical and functional boundaries of cells. They enable compartmentalization, regulate molecular transport, and serve as dynamic platforms for energy conversion and signal transduction. Despite compositional diversity, membranes share a common organizational principle: a self-assembled lipid bilayer containing embedded proteins and carbohydrates (Fig. 1.1).[51]

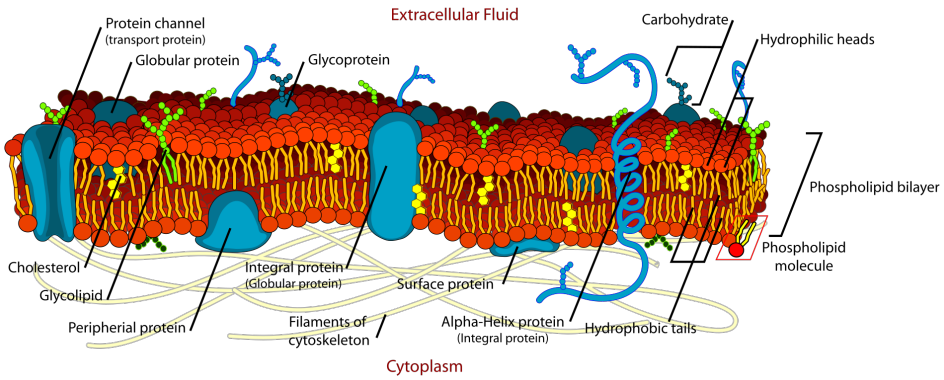

Figure 1.1 Schematic representation of a biological membrane illustrating the lipid bilayer, membrane proteins, and associated carbohydrates (adapted from [52]).

Phospholipids, the principal structural components, possess hydrophilic headgroups and hydrophobic acyl tails. In aqueous media they spontaneously arrange into bilayers that minimize free energy by segregating hydrophobic moieties from water. The bilayer is selectively permeable, allowing diffusion of

small non-polar molecules while restricting ions and large polar solutes. Membrane composition reflects cellular function. Eukaryotic plasma membranes typically contain approximately equal masses of lipids and proteins, whereas mitochondrial membranes may contain up to 70 % protein, consistent with high metabolic activity. Carbohydrate chains covalently attached to lipids and proteins constitute the glycocalyx, which mediates cell–cell recognition and immune responses.

1.2.2 Membrane components

Biological membranes are dynamic and asymmetric molecular assemblies composed primarily of lipids, proteins, and carbohydrates. Each class performs specific yet interdependent functions: lipids provide the structural matrix and define permeability and phase behaviour; proteins confer functionality and selectivity; carbohydrates mediate recognition, communication, and protection. Although these components are ubiquitous across life, their proportions and molecular details differ markedly between eukaryotic, bacterial, and archaeal systems, reflecting adaptation to diverse environments and evolutionary pressures.

1.2.2.1 Lipids

Lipids are the most abundant membrane constituents and are characterized by their amphiphilic nature: they contain both hydrophilic and hydrophobic regions and self-assemble spontaneously into bilayers or monolayers in aqueous environments. They can be grouped into four major classes: phospholipids, sphingolipids, sterols, and glycolipids.

Phospholipids. Phospholipids are the principal structural lipids of cellular membranes. Each molecule consists of a hydrophilic phosphate-containing headgroup and one or two hydrophobic acyl chains. Depending on the core scaffold, two subclasses exist: glycerophospholipids and ether-linked archaeal lipids.

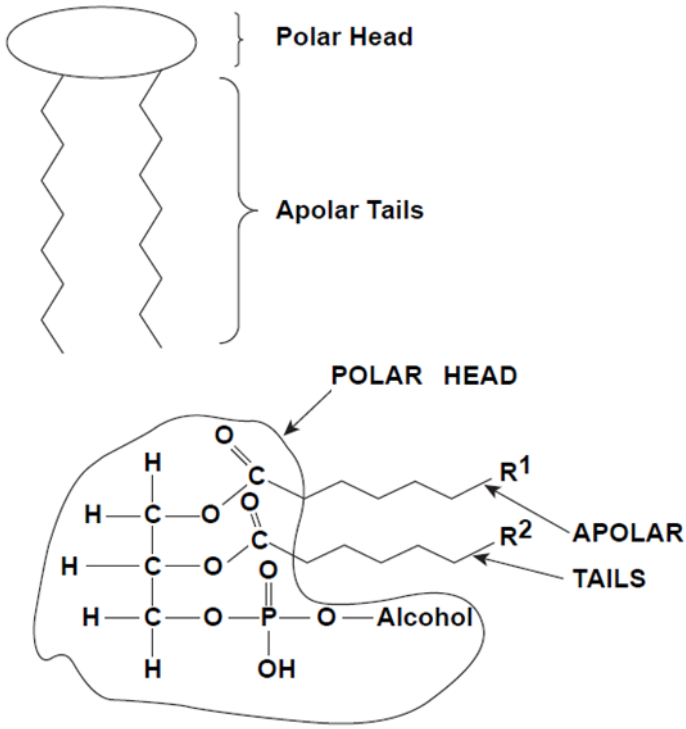

Figure 1.2. Schematic representation of a glycerophospholipid. R1 and R2 indicate the fatty acids and X represents the functional group (adapted from [9]).

Glycerophospholipids dominate in bacterial and eukaryotic membranes. Their basic structure comprises a glycerol backbone esterified at the *sn-1* and *sn-2*

positions to fatty acids and at *sn-3* to a phosphate group (Figure 1.2). The acyl chains usually contain 14–24 carbons and may be saturated or unsaturated; their composition regulates bilayer fluidity. The polar headgroup determines the charge and chemical behaviour of the lipid (Fig. 1.3). Phosphatidylcholine (PC) is zwitterionic, having a positively charged choline balanced by the phosphate group. Phosphatidylethanolamine (PE), the dominant phospholipid in many bacteria, is slightly negative due to partial amine deprotonation. Phosphatidylserine (PS), phosphatidylglycerol (PG), and phosphatidylinositol (PI) carry a net charge of –1. Phosphatidic acid (PA), lacking an esterified alcohol, is a minor but metabolically crucial anionic lipid.

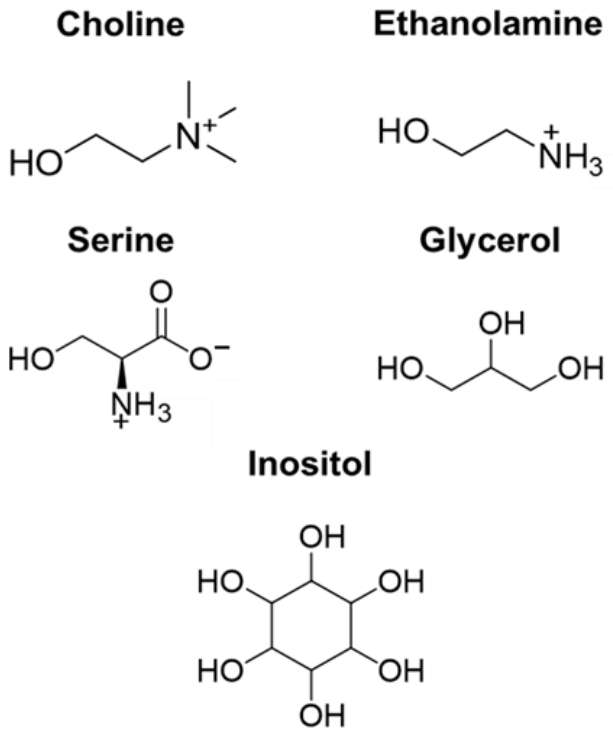

Figure 1.3 Structure of the most common lipid headgroups.

Phospholipid distribution differs among organisms: in most eukaryotic plasma membranes, PC is predominant, followed by PE, PS, and PI[53,54]. On the contrary, in Gram-negative bacteria such as *Escherichia coli*, PE and PG account for approximately 75% and 20% of total phospholipids, respectively, while cardiolipin forms about 5%, concentrated at the cell poles and division sites where high curvature is required [55–57]. Moreover, Gram-positive bacteria share a similar phospholipid composition but often contain higher proportions of PG and diphosphatidylglycerol (cardiolipin) due to their thick peptidoglycan layer [58].

In contrast, archaea employ an entirely distinct lipid architecture: their membranes are composed of ether-linked isoprenoid chains rather than ester-linked fatty acids, conferring enhanced resistance to hydrolysis and oxidation[59]. Archaeal backbones are built from glycerol-1-phosphate (G1P), the enantiomer of the bacterial/eukaryotic glycerol-3-phosphate (G3P), indicating an independent evolutionary lineage[60]. Many thermophilic archaea form monolayer membranes of bipolar tetraether lipids (e.g., caldarchaeol)[61], which remain stable at temperatures above 100 °C and across wide pH ranges.

Sphingolipids. Sphingolipids are amphipathic molecules composed of a sphingosine backbone, an 18-carbon amino alcohol with a trans double bond at C4, amide-linked to a fatty acid at C2 and carrying a polar substituent at C1[62]. Structural diversity arises from two variables: (i) the length and saturation of the acyl chain (6–25 carbons), and (ii) the chemical nature of the headgroup. Sphingolipids are generally absent in most prokaryotes, but they occur in certain Bacteroidetes and Planctomycetes, where they may confer enhanced membrane rigidity and resilience under environmental stress[63]. In eukaryotes, sphingomyelins interact strongly with cholesterol, promoting the formation of

lipid rafts: ordered microdomains implicated in signalling, trafficking, and protein sorting [64,65].

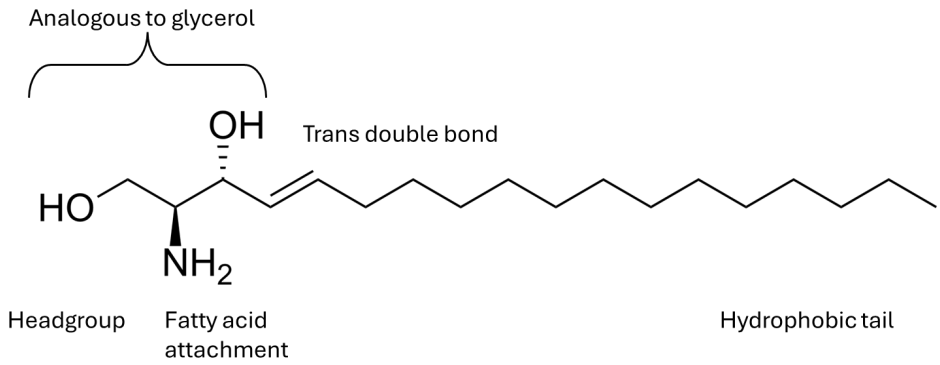

Figure 1.4 Sphingosine structure

Sterols. Sterols are weakly amphiphilic molecules derived from the cyclopentanoperhydrophenanthrene core. The hydroxyl group at C3 contributes limited polarity, while the hydrophobic rings and side chain facilitate packing among acyl chains. In animals, cholesterol represents up to 40 mol % of plasma membrane lipids and regulates both fluidity and permeability, preventing extremes of order or disorder. Plants and fungi utilize sitosterol and ergosterol, respectively, which play analogous structural roles[66,67]. On the contrary, bacterial membrane lack sterols[68].

Glycolipids. Glycolipids consist of a carbohydrate moiety attached via a glycosidic bond to a lipid backbone. They can derive from glycerophospholipids or sphingolipids. In bacteria, glycolipids such as monoglucosyldiacylglycerol and diglucosyldiacylglycerol contribute to outer membrane stability and environmental sensing. In eukaryotes, glycosphingolipids and gangliosides

perform structural and recognition roles, particularly in immune interactions and neural communication[69].

1.2.2.2 Proteins

Membrane proteins account for approximately half the mass of most cellular membranes and mediate nearly all biological functions, transport, signal transduction, catalysis, and energy conversion. They are classified as integral, peripheral, or lipid-anchored, depending on their mode of membrane association[70]:

- Integral (intrinsic) proteins contain one or more segments embedded within the hydrophobic core. Transmembrane domains typically adopt α-helical (in most membranes) or β-barrel (in bacterial outer membranes) conformations. Examples include ion channels, transporters, and G protein-coupled receptors (GPCRs). The latter comprise seven transmembrane helices and link extracellular stimuli to intracellular signalling cascades via activation of peripheral G-proteins associated with the cytoplasmic surface.

- Peripheral (extrinsic) proteins bind electrostatically or through hydrogen bonding to the membrane surface or to integral proteins. They function as enzymes, redox partners, or structural linkers (e.g., cytoskeletal anchoring).

- Lipid-anchored proteins are covalently attached to fatty acids (myristate, palmitate) or prenyl groups on the cytoplasmic side, or via

glycosylphosphatidylinositol (GPI) anchors on the extracellular side. Such attachments regulate localization and mobility.

In prokaryotes, membrane proteins perform crucial roles in bioenergetics, as the plasma membrane substitutes for eukaryotic organelles. It hosts the electron transport chain, ATP synthase, and numerous transport systems. Gram-negative bacteria add a secondary outer membrane, rich in porins and lipopolysaccharides (LPS), which serves as a selective permeability barrier and a determinant of pathogenicity.

1.2.2.3 Carbohydrates

Carbohydrates form the most external component of cellular membranes and are covalently attached to lipids or proteins, generating glycolipids and glycoproteins. Together, these structures constitute the glycocalyx: a hydrated, negatively charged network essential for cell recognition, adhesion, and protection. Carbohydrate residues commonly found in membranes include glucose, galactose, mannose, fucose, arabinose, xylose, N-acetylglucosamine, N-acetylgalactosamine, and N-acetylneuraminic acid (sialic acid)[9]. They may be linear or branched, forming short oligosaccharides (<15 units) with diverse linkage patterns. This variability creates immense structural and informational complexity, supporting the concept of a “carbohydrate code” for cell–cell communication and immune signalling.

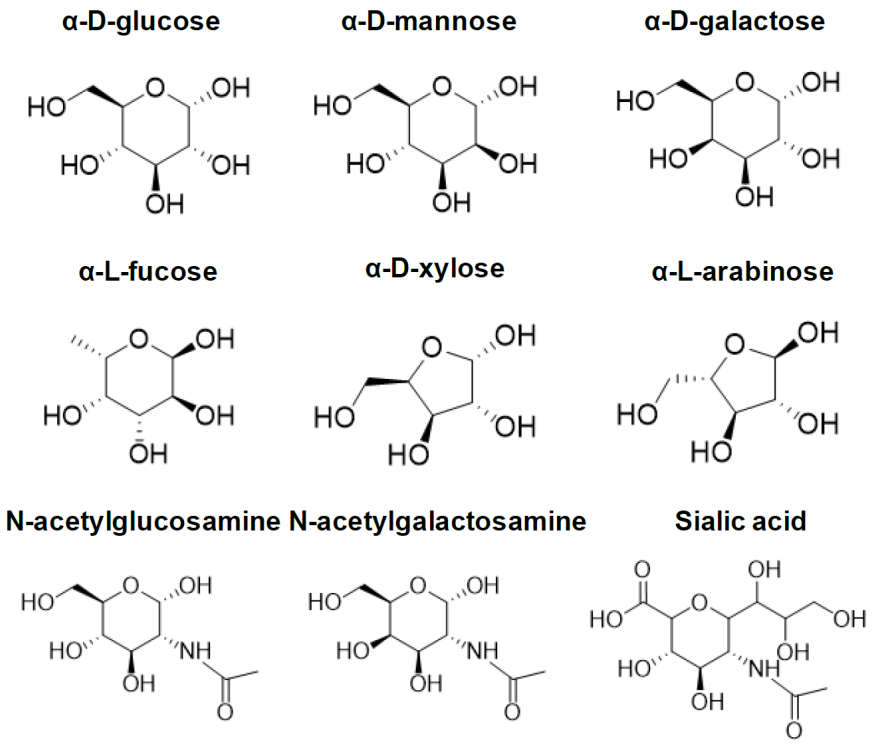

Figure 1.5 The nine most common structural units of membrane carbohydrates.

In prokaryotes, carbohydrates assume specialized structural roles:

- In Gram-negative bacteria, lipopolysaccharides (LPS) form the outer leaflet of the outer membrane, contributing to permeability control and immune recognition [71].

- In Gram-positive species, teichoic and lipoteichoic acids extend through the peptidoglycan wall and contribute to cation binding and surface charge regulation[72,73].

- Archaea often display surface-layer (S-layer) glycoproteins and glycosylated lipids that provide stability under extreme salinity or temperature[74].

In eukaryotes, glycosylation modulates protein folding, protects against proteolysis, and defines cell identity. In both domains of life, membrane-associated carbohydrates are central to recognition, adhesion, and environmental adaptation [75,76].

1.2.3 Membrane proteins and dynamics

Proteins embedded in or associated with the lipid bilayer execute most membrane functions, including transport and catalysis. Integral proteins span or anchor within the bilayer; peripheral proteins interact through electrostatic or hydrophobic associations. In 1972, Singer and Nicolson proposed the *fluid mosaic model* to describe the structural organization and dynamic properties of biological membranes. According to this model, membranes consist of a fluid lipid bilayer containing globular proteins with restricted lateral mobility within the lipid matrix [77]. This dynamic arrangement allows biological membranes to combine structural stability with functional flexibility, forming a continuously reorganizing environment essential for transport, signalling, and molecular recognition. The mobility of phospholipids within the bilayer is expressed through several types of motion [78]:

- Rotational motion: individual phospholipids rotate rapidly around their long molecular axis, modulating local packing and interactions with neighbouring molecules.

- Lateral diffusion: lipids diffuse within the same leaflet of the bilayer, a process fundamental for maintaining membrane fluidity. However, it can be hindered by embedded proteins and by changes in lipid composition or phase state. As a result, membrane viscosity exceeds that of bulk water by factors of 10^3–10^4, reflecting the high internal friction within the bilayer plane[9].

- Transverse diffusion (flip-flop): this process involves the translocation of a lipid molecule from one leaflet to the opposite. Because it requires the transient exposure of the hydrophobic acyl chains to water and of the polar headgroup to the bilayer core, the energetic barrier is substantial. Consequently, spontaneous flip-flop occurs extremely slowly, with characteristic half-lives from days to weeks in the absence of catalytic proteins such as flippases or scramblases. Nevertheless, this motion is essential for maintaining and regulating membrane asymmetry.

- Intramolecular motions: phospholipids undergo rapid internal motions, including bond rotations, torsions, and vibrations within both the acyl chains and the polar headgroup. These contribute to the local flexibility and dielectric behaviour of the membrane.

- Undulation: this collective mode involves slow, wave-like oscillations of the bilayer surface induced by thermal energy. Membrane undulations play a role in elasticity, vesicle deformation, and interactions with proteins and other membranes[79].

Membrane proteins also exhibit dynamic behaviour, being capable of rotational and lateral diffusion within the bilayer. However, their transverse motion is

usually restricted, and proteins associated with the cytoskeleton or extracellular matrix may display severely limited mobility. The combination of lipid and protein dynamics defines the physical basis of the “fluid mosaic,” linking molecular motion to the biological functions of membranes.

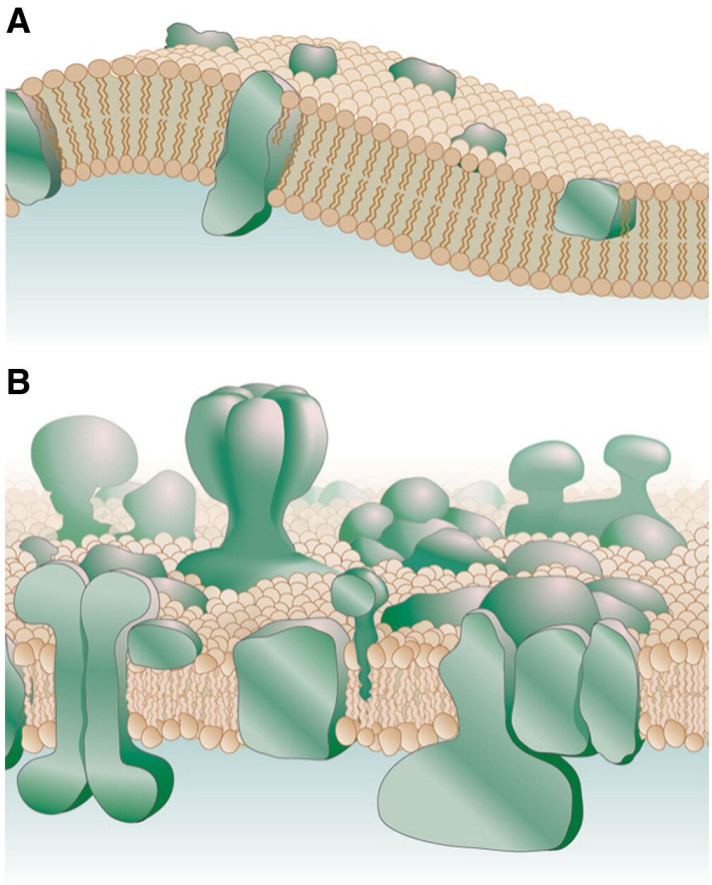

Figure 1.6 Abundance of membrane proteins (A) in the Singer-Nicolson model and (B) in an update version [80].

Membrane fluidity is influenced by temperature, pH, ionic strength, and lipid composition. Cholesterol and sphingolipids generate liquid-ordered (L_o) regions that coexist with liquid-disordered (L_d) areas. These microdomains participate in signal transduction and protein localization [81].

1.2.4 Membranes in extremophiles

Lipid composition is a key determinant of environmental tolerance and thus each extremophile exhibit a characteristic lipid composition, when compared to mesophilic organisms:

- Thermophiles and hyperthermophiles typically exhibit membranes highly resistant to heat-induced disordering. In archaea, this is achieved through the synthesis of isoprenoid ether lipids, which may form monolayer membranes composed of *tetraether lipids* such as caldarchaeol. These structures remain stable above 100 °C and across wide pH ranges, owing to their reduced permeability and extensive hydrophobic packing. In contrast, bacterial thermophiles rely primarily on increased saturation of fatty acyl chains and a high proportion of branched-chain lipids, which elevate the gel-to-fluid transition temperature and enhance van der Waals interactions between acyl tails [42,45].

- Psychrophiles, on the contrary, maintain membrane fluidity under subzero conditions by incorporating unsaturated and short-chain fatty acids, which introduce kinks and reduce packing density. Some polar lipids are enriched in polyunsaturated fatty acids such as eicosapentaenoic or docosahexaenoic acid, confereiring flexibility and low transition

temperatures. The presence of glycolipids and phosphatidylglycerol derivatives also modulates the interfacial hydrogen-bond network, improving fluidity in cold environments [43,82,83].

- Halophiles, which inhabit hypersaline environments, produce membranes rich in negatively charged and glycosylated lipids that preserve structural integrity despite high ionic strength. The anionic headgroups bind hydrated cations, while glycosyl moieties maintain hydration layers at the bilayer interface. Some extreme halophilic archaea, such as *Halobacterium salinarum*, employ bacterioruberin pigments within their membranes to provide both rigidity and protection against oxidative and photic stress [44,84].

- Piezophiles, organisms adapted to high hydrostatic pressure such as deep-sea microbes, counteract pressure-induced lipid ordering by incorporating unsaturated and monounsaturated acyl chains, as well as cis double bonds that prevent close packing. Certain deep-sea archaea synthesize diether lipids with methyl branching, which preserve fluidity at pressures exceeding 100 MPa [85,86].

In prokaryotes such as *Escherichia coli*, the plasma membrane performs most compartmental functions. Its dominant lipids, phosphatidylethanolamine (PE) and phosphatidylglycerol (PG), provide an anionic surface essential for interactions with cationic species. Artificial membrane models replicate essential features of natural bilayers for controlled biophysical studies. Liposomes, supported bilayers, and monolayers are used to examine interactions between lipids and peptides, enzymes, or small ligands.

1.2.5 Liposomes as model membranes

Model membranes facilitate quantitative analysis of how external variables or binding events modify bilayer properties, forming an essential framework for subsequent examination of membrane-ligand interactions. Liposomes are supramolecular assemblies composed of one or more lipid bilayers arranged in concentric lamellae and separated by aqueous compartments. In aqueous environments, amphiphilic molecules such as phospholipids spontaneously self-assemble into these structures owing to their polar headgroups and hydrophobic acyl chains. First described in the 1960s [87], liposomes have since been extensively employed as model membrane systems. Their structural simplicity and tunability have made them valuable tools for investigating fundamental membrane properties, including fluidity, phase transitions, and lateral diffusion[88,89]. According to their size and number of bilayers, liposomes are typically classified as:

- Multilamellar vesicles (MLVs): composed of two or more concentric bilayers, with diameters generally between 1 and 5 μm;
- Large unilamellar vesicles (LUVs): containing a single bilayer, with diameters of approximately 100–250 nm;
- Small unilamellar vesicles (SUVs): also composed of a single bilayer, but with smaller diameters, typically ranging from 20 to 100 nm.

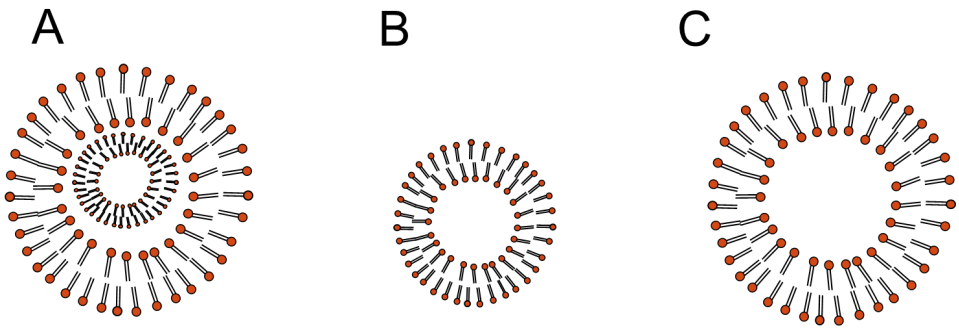

Figure 1.7 Classification of model membrane systems: (A) multilamellar vesicles (MLVs), (B) small unilamellar vesicles (SUVs) and (C) large unilamellar vesicles (LUVs).

The physical state of the lipid phase within liposomes depends primarily on the acyl-chain length and temperature. At 25 °C, liposomes composed of saturated lipids such as DPPC exist in the gel phase (L_β), in which the acyl chains adopt an all-*trans* conformation. This arrangement promotes tight molecular packing and confers high membrane rigidity. Upon heating, the bilayer undergoes a transition to the liquid-crystalline phase (L_α), characterized by reduced thickness, increased molecular disorder, and enhanced lateral mobility of lipid molecules within each leaflet. An intermediate state, the rippled gel phase ($P_{\beta'}$), may also occur. In this configuration, lipid headgroups are tilted relative to the acyl chains, resulting in a periodic ripple pattern that represents a transitional state between the ordered L_β and disordered L_α phases.

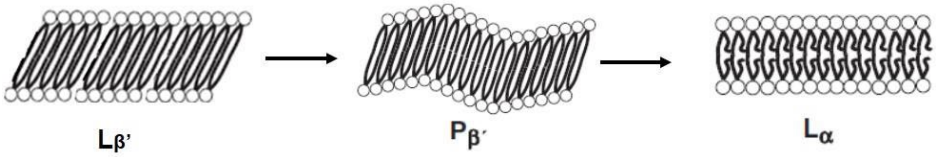

Figure 1.8 Common lipid phases: Gel phase L_{β}, Rippled gel phase (L_{α}), Liquid crystalline phase ($P_{\beta'}$)

However, membranes are not the only key components that regulate life, proteins also exhibit different behaviours in response to environmental stress.

1.3 Protein–ligand interactions in harsh conditions

Molecular recognition between macromolecules underlies all biological function, from enzymatic catalysis to signalling and transport. The same non-covalent forces that drive protein–ligand association, hydrogen bonding, electrostatics, dispersion, and the hydrophobic effect, govern how such complexes adapt to extreme physicochemical environments. Understanding these mechanisms is central to defining the thermodynamic limits of biological activity in planetary and terrestrial extreme settings. The formation of a protein–ligand complex reflects the interplay between enthalpic stabilization and entropic reorganization. Hydrogen bonds and electrostatic complementarity contribute to favourable enthalpy, while conformational restriction and solvent rearrangement produce entropy changes. These terms are often interdependent, leading to enthalpy–entropy compensation, which maintains a relatively constant free energy of binding across a wide range of conditions [90–92]. This compensation forms the

basis of thermodynamic resilience, allowing macromolecules to remain functional even when solvent structure or external parameters vary. The solvent environment strongly modulates these energetic balances. According to the Hofmeister series, kosmotropic ions such as SO_4^{2-} and Mg^{2+} promote water structuring and protein compaction, whereas chaotropic ions such as ClO_4^- and SCN^- disrupt hydrogen bonding, weakening the hydrophobic effect [93,94]. For example, the halophilic enzyme *malate dehydrogenase* from *Halobacterium salinarum* remains active at 4–5 M NaCl, relying on a highly acidic, solvent-exposed surface that preserves solubility and prevents aggregation. Moreover it has been reported that the same enzyme has a higher efficiency at higher salinity level [95]. In contrast, chaotropic perchlorate, abundant in Martian regolith, usually destabilizes folded proteins and weakens ligand binding by disrupting hydration layers[96–98]. These ion-specific effects illustrate how solvation dynamics shape molecular recognition under high-salinity or extraterrestrial aqueous conditions. Temperature exerts an equally strong influence by altering conformational flexibility and solvent organization. *Taq* DNA polymerase from *Thermus aquaticus* retains catalytic activity near 95 °C by pre-organizing its unbound conformation, thus reducing the entropic penalty upon substrate binding [99]. In contrast, *α-amylase* from the Antarctic bacterium *Pseudoalteromonas haloplanktis* remains functional at 4 °C due to increased loop flexibility and a higher density of surface hydrogen bonds[100]. These adaptations minimize the loss of free energy associated with molecular association across extreme thermal regimes. Hydrostatic pressure, characteristic of deep-sea and subsurface environments, modifies binding equilibria through the volume change accompanying complex formation. When complexation reduces total volume, by collapsing internal cavities or expelling hydration water, pressure stabilizes the complex[101–103]. Across these variables, salinity, temperature, and

pressure, proteins display compensatory energetic behavior. Perturbations that weaken hydrogen bonding or alter hydration often enhance molecular motion, while increased rigidity under compression strengthens dispersion and electrostatic interactions. This dynamic self-adjustment defines the thermodynamic and structural resilience of macromolecular complexes[104].

1.4 The emergence of life: interplay between G-quadruplexes and primitive membranes in harsh conditions

1.4.1 Introduction

The emergence of life from non-living matter represents one of the most profound transitions in the history of our planet. Although many details remain uncertain, it is widely accepted that this process required a synergistic interplay between informational polymers and compartment-forming molecules, enabling the coupling of molecular replication, catalysis, and selection. In this context, nucleic acids and primitive membranes likely played central, mutually reinforcing roles during the earliest stages of evolution [105–107]. The compartmentalization provided by self-assembled lipid bilayers was crucial for generating microenvironments where reactants could concentrate, molecular stability could increase, and catalytic cycles could proceed with higher efficiency[105,107,108]. At the same time, nucleic acids provided a unique molecular scaffold capable of storing information and performing catalytic functions, thus bridging the gap between chemistry and biology[109]. Among the hypotheses proposed to describe this early biochemical

landscape, the RNA world hypothesis[110,111] has gained particular prominence. It postulates that, before the appearance of DNA and proteins, RNA molecules fulfilled a dual role as both carriers of genetic information and functional catalysts (ribozymes). This view is supported by experimental demonstrations of RNA's ability to catalyse a variety of reactions, including self-splicing, peptide bond formation, and replication of short RNA fragments[112–114] (Fig. 1.9). However, several challenges complicate the RNA world scenario. The abiotic synthesis of long RNA polymers under prebiotic conditions remains non-trivial, and unprotected RNA molecules are susceptible to hydrolysis and chemical degradation [115,116]. Furthermore, the diversity of RNA structures suggests that early functional nucleic acids might not have been limited to canonical duplexes or linear strands[117]. Indeed, RNA and DNA can adopt a wide range of non-canonical secondary structures, stabilized by specific base pairing and cation-mediated interactions. Among these, G-quadruplexes (G4s) have attracted increasing attention as potential ancient molecular architectures. G4s are highly stable, compact helical structures formed by guanine-rich sequences through Hoogsteen-type hydrogen bonding, stabilized by the presence of monovalent cations such as K^+ or Na^+ which will be discussed in a subsequent paragraph. Their robustness, structural polymorphism, and ability to form under diverse conditions make them attractive candidates for primitive functional folds that could have emerged in a prebiotic setting.

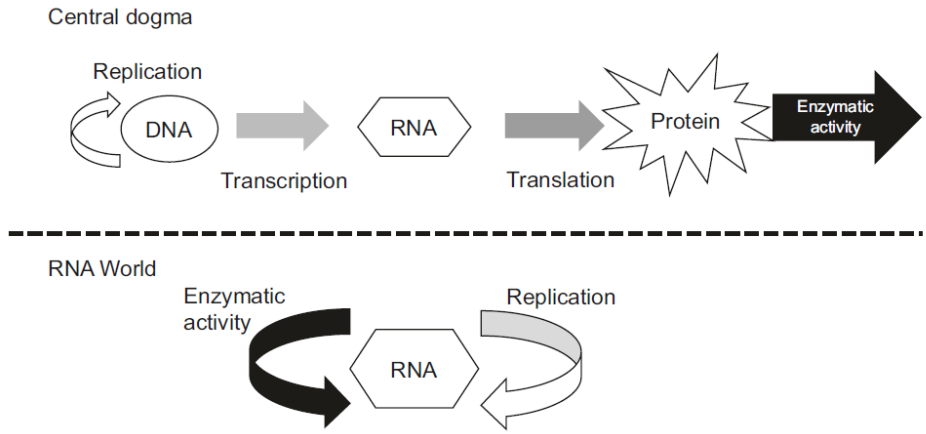

Fig. 1.9 Central dogma and the RNA world. In the central dogma, genetic information flows from DNA to RNA to protein. DNA stores the information, RNA carries it, and proteins perform functions. In the RNA world, RNA served both as the storage of genetic information and the functional molecule.

Building upon the RNA world framework, the G-quadruplex world hypothesis proposes that G4s may have been among the earliest structured nucleic acids to appear on the prebiotic Earth[118]. Their enhanced chemical and thermal stability compared to canonical duplexes could have conferred a selective advantage in harsh early environments characterized by fluctuating temperature, pH, and ionic conditions[119]. Moreover, G4s exhibit remarkable chemical versatility: they can interact with small molecules, ions, and lipid membranes, and can even promote catalytic activities[109,120,121]. These properties suggest that G4-forming sequences might have contributed to the development of primitive biochemical networks and to the molecular organization necessary for life's emergence. However, the role of such non-canonical structures must also be considered in light of the compartmentalization process, a fundamental step toward cellular

organization[105]. Amphiphilic molecules, such as fatty acids and phospholipid precursors, can spontaneously assemble into bilayers and vesicles under prebiotic conditions, providing boundaries that separate internal and external environments while allowing selective permeability. This proto-membrane formation not only offered protection and concentration of molecules but may also have served as a dynamic surface promoting molecular adsorption, alignment, and catalysis[106,122,123]. Thus, interactions between nucleic acids and primitive lipid bilayers could have influenced the stabilization, folding, and function of early polymers, potentially facilitating the first steps toward molecular cooperation and evolutionary selection[124,125]. Modern biological systems provide strong analogies for the relevance of such interactions. Nucleic acid–membrane associations play crucial roles in gene regulation, viral replication, and signalling processes occurring at membrane–water interfaces[126,127]. These examples illustrate that membranes are not passive boundaries but active interfaces capable of modulating the physical and chemical behaviour of nucleic acids. Despite this biological relevance, most experimental studies have focused on canonical DNA and RNA structures, leaving the behavior of G-quadruplexes at membrane interfaces largely unexplored[128–131]. Key questions remain regarding how membrane composition, surface charge, and phase state influence G4 formation, topology, and stability, and whether such interactions could have played a role in prebiotic chemistry. Addressing these questions is essential to understanding how nucleic acid–membrane interplay may have shaped the first steps of life's organization, bridging the gap between molecular self-assembly and the emergence of biological complexity. In the next paragraph a brief description of the key characteristics of G-quadruplex is presented.

1.4.2 G-Quadruplex Structures

G-quadruplexes (G4s) are non-canonical nucleic acid architectures formed through the stacking of guanine tetrads (G-tetrads) stabilized by the coordination of metal cations within a central channel (Fig. 1.10)[132]. Each G-tetrad consists of four guanine bases arranged in a cyclic, planar configuration and held together by Hoogsteen-type hydrogen bonds. In each guanine, the exocyclic amino group at C2 and N1 act as hydrogen-bond donors, while O6 and N7 serve as acceptors. The four carbonyl oxygens point inward, creating a negatively charged cavity that selectively accommodates cations.

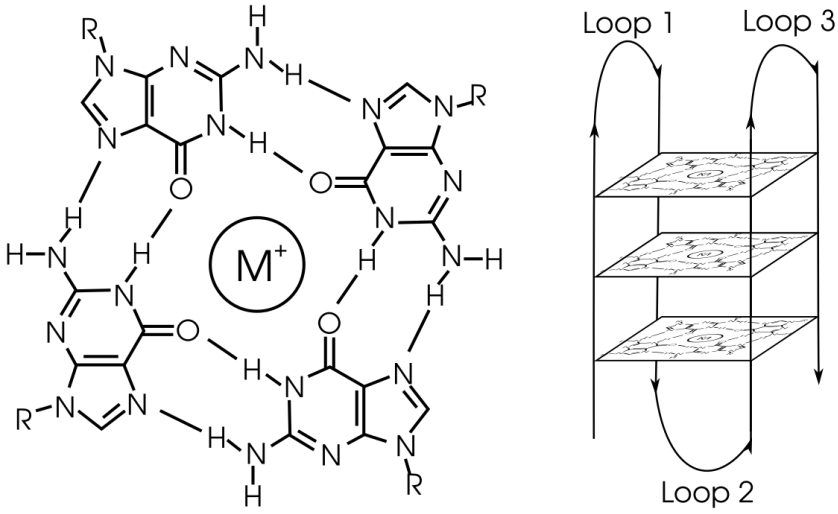

Figure 1.10 Schematic representation of a guanine tetrad and a quadruplex assembly

This central coordination site is crucial for the structural integrity and thermodynamic stability of G-quadruplexes. Potassium (K^+) and sodium (Na^+) are

the most common stabilizing cations[133]. Owing to their distinct ionic radii (Na^+ < K^+), the ions occupy different positions within the quadruplex: K^+ typically resides between adjacent G-tetrads, coordinating eight carbonyl oxygens, while Na^+ lies within a single tetrad plane, interacting with four. The free energy of coordination and dehydration is more favourable for K^+, rendering it the more effective stabilizer[134]. Consequently, G-quadruplexes formed in K^+ solutions are generally more stable and often adopt distinct topologies compared with those stabilized by Na^+ [133,134].

A G-quadruplex can arise from one, two, or four strands of nucleic acid. Its topology is determined by the relative orientation of these strands and by the geometry of the loops connecting the guanine tracts. Three principal categories are recognized[135]:

- Parallel quadruplexes, in which all strands run 5′ → 3′ in the same direction and are connected by propeller (chain-reversal) loops.
- Antiparallel quadruplexes, where alternating strand orientations generate lateral or diagonal loops and produce alternating groove widths.
- Hybrid quadruplexes, combining both parallel and antiparallel orientations.

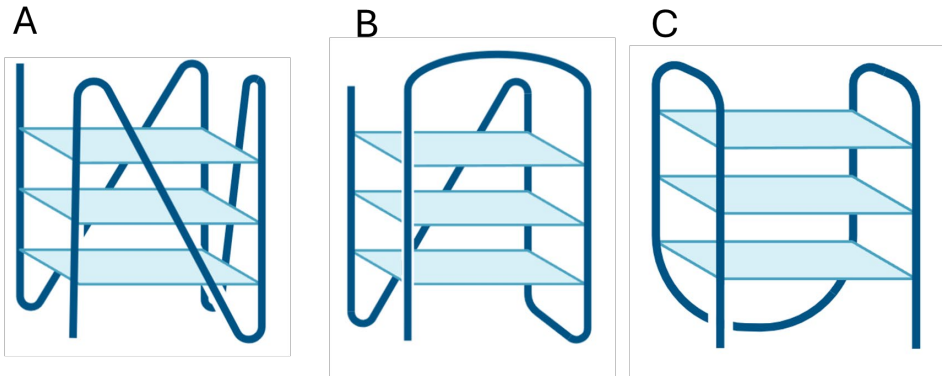

Figure 1.11 Schematic representation of principal G-quadruplex topologies: (A) parallel, (B) hybrid, (C) antiparallel.

In addition to influencing overall stability, the type of coordinating cation can also modulate the folding pathway and global architecture of a G-quadruplex [136]. Any potential unimolecular G-quadruplex can be described by a consensus sequence motif of the form $\mathbf{G_mX_nG_mX_oG_mX_pG_m}$, where *m* denotes the number of consecutive guanine residues in each tract, and X_n, X_o, and X_p represent variable loop regions composed of any nucleotides that connect the guanine tracts[137]. Beyond intramolecular structures, G-quadruplexes can also form through the association of two or four distinct strands, giving rise to bimolecular and tetramolecular assemblies, respectively. In most biologically relevant contexts, G-quadruplexes comprise three or four stacked G-tetrads, a configuration that confers enhanced thermodynamic stability under physiological conditions[138–140].

RNA quadruplexes exhibit markedly reduced polymorphism compared with their DNA counterparts. The 2′-hydroxyl group of ribose enforces a C3′-endo sugar pucker and restricts the glycosidic angle, favouring the anti-conformation for all guanines and thereby promoting parallel strand alignment [141]. DNA

quadruplexes, lacking this geometric constraint, display a broader structural repertoire and can form parallel, antiparallel, or hybrid folds depending on ionic composition, hydration level, and molecular crowding. The structural plasticity and thermodynamic robustness of G-quadruplexes distinguish them from other nucleic acid motifs. Their ability to adopt multiple, yet structurally well-defined, conformations enables them to remain stable and functionally active across heterogeneous chemical settings, ranging from cellular environments to prebiotic systems [142]. This combination of stability, responsiveness, and structural diversity provides the foundation for their biological relevance and supports their potential role as ancient informational or catalytic scaffolds in early molecular evolution [119].

1.5 Thesis aim

The aim of this PhD thesis is to elucidate how physicochemical factors, temperature, ionic composition, pressure and hydration, govern the structure, stability, and energetics of biological macromolecules across distinct chemical environments. By combining spectroscopic, calorimetric, and microscopic techniques, this work investigates molecular organization over multiple levels of complexity, from lipid bilayers to protein–ligand complexes and nucleic acid–membrane assemblies. The first two parts of the thesis (Chapters 2 and 3) focus on Martian-relevant aqueous conditions, examining how high hydrostati pressure and/or salt-rich environments affect the stability of lipid membranes and the thermodynamics of protein–ligand recognition. The final part (Chapter 4) explores the interaction of G-quadruplexes with membranes as first step in assessing the possibility that proto-membranes could have fine-tuned structure

and stability of nucleic acids. Together, these studies aim to identify the physicochemical principles that underpin biomolecular stability, recognition, and adaptability in both extraterrestrial and terrestrial contexts, advancing our understanding of the molecular strategies that enable life to emerge and persist under diverse environmental constraints.

Chapter 2 - Bacterial model membranes under harsh Martian-like conditions.

2.1 Introduction

Assessing the chemical and physical boundaries of biomolecular stability is essential to evaluate the habitability of extraterrestrial environments [1]. On Mars, increasing evidence points to the presence of subsurface liquid water, possibly in the form of brine lakes below the polar caps [3,143,144]. At depths of up to 10 km, such groundwater could experience hydrostatic pressures of ~1 kbar [143]. In addition, the Martian surface and subsurface are enriched in salts, particularly perchlorates and sulphates, which are expected to reach high concentrations in these brines[145–147]. While such conditions are highly challenging for life, they are of prime interest in understanding the limits of biomolecular function. Particularly, perchlorates are chaotropic ions known to disrupt water structure and hydrogen-bonding network, thereby perturbing biomolecular hydration, stability, and function[148]. Previous studies have shown that perchlorates destabilize enzymes such as α-chymotrypsin[98,148], and they have also been reported to modulate protein–ligand interactions even at the level of single binding sites[102]. However, despite this growing knowledge, the impact of Mars-relevant salts on other key biomolecular systems, such as cellular membranes, remains poorly understood. Cellular membranes are central to life, providing structural integrity, compartmentalization, and a platform for processes such as energy transduction and signalling. Their physical state and functional properties can be tuned through lipid composition, allowing adaptation to environmental changes[4–6]. While

recent work has investigated the response of eukaryotic model membranes to Mars-like salts[149], much less is known about their effects on bacterial-type membranes, which are simpler but highly relevant for extremophile survival. In this chapter, the impact of perchlorate and sulphate salts on a prototypical bacterial membrane composed of phosphatidylethanolamine (PE) and phosphatidylglycerol (PG) will be examined. Using a combination of differential scanning calorimetry, fluorescence spectroscopy, confocal microscopy, circular dichroism, and small-angle X-ray scattering, in combination with high hydrostatic pressure, the impact of Martian relevant salts on membrane structure, fluidity, and morphology will be investigated. To connect these structural changes with biological function, the activity of the membrane-associated enzyme phospholipase A2 (PLA2) was also studied. PLA2 plays a key role in regulating membrane composition and physical state by hydrolysing the sn-2 ester bond of phospholipids, and its activity is known to be highly sensitive to lipid packing and osmotic stress[150]. The results demonstrate that bacterial lipid bilayers retain structural integrity under selected combinations of Mars-relevant salts and pressure. Remarkably, PLA2 retains enzymatic activity even under harsh conditions characterized by high $Mg(ClO_4)_2$ concentrations combined with elevated hydrostatic pressure, supporting the possibility that membrane functionality, and by extension, microbial life, may be sustained in Martian subsurface brines.

2.2 Experimental section

2.2.1 Chemicals

The phospholipids 1,2-dipalmitoyl-sn-glycero-3-phosphoethanolamine (DPPE), 1,2-dipalmitoyl-sn-glycero-3-phospho-(1'-rac-glycerol) sodium salt (DPPG), 1-palmitoyl-2-oleoyl-sn-glycero-3phosphoethanolamine (POPE), and 1-palmitoyl-2-oleoyl-sn-glycero-3-phospho-(1'-rac-glycerol) sodium salt (POPG) were purchased from Avanti Polar Lipids (Alabaster, USA). Magnesium perchlorate, magnesium sulphate, magnesium chloride, the corresponding sodium salts and the HEPES buffer were purchased from Merck (Darmstadt, Germany). The fluorescent probes N-(lissamine rhodamine B sulfonyl)-1,2-dihexadecanoyl-sn-glycero-3-phosphoethanolaminetriethylammonium salt (N-Rh-DHPE), and Laurdan (6-dodecanoyl-N,N-dimethyl-2naphthylamine) were purchased from Molecular Probes (Invitrogen, California, USA), ATTO-TEC (Siegen, Germany) and Merck, respectively. Phopholipase A2 from honey bee venom (bvPLA2) was purchased from Merck and its fluorogenic substrate 1-O-(6-Dabcyl-aminohexanoyl)-2-O-(12-(5-BODIPY®-pentanoyl)aminododecanoyl)-sn-glyceryl phosphatidylcholine (DBPC) was purchased from MoBiTec (Goettingen, Germany).

2.2.1 Vesicles preparation

Vesicles were prepared by weighing appropriate amounts of lipid stock solutions and evaporating the organic solvent under a stream of nitrogen 42 to obtain a suspension of multilamellar vesicles (MLVs). Large Unilamellar Vesicles (LUVs)

of 100 nm size were obtained by extruding MLVs at least 21 times through two stacked polycarbonate filters and a permeable membrane with 100 nm pores (Nuclepore, Pleasanton, USA). The whole procedure was carried out using an extruder (Avanti Polar Lipids) filled with two 1.0 mL Hamilton syringes (Hamilton, Reno, USA). Vesicles size was confirmed by means of dynamic light scattering (DLS) measurements, which showed a mean hydrodynamic radius consistent with the formation of LUVs. Giant Unilamellar Vesicles (GUVs) were prepared with the electroformation method using a 1 mg mL-1 lipid solution. For the electroformation, a constant frequency of 500 Hz and an alternating electric field of 0.14 V (5 min), 1.25 V (20 min), and 3.5 V (90 min) was applied at a temperature of 45 °C. GUVs were used for fluorescent microscopy measurements, LUVs were used for enzyme kinetics measurements while MLVs were used in all the other cases. DPPE/DPPG in an 8/2 ratio were used for the DSC measurements, while POPE/POPG at an 8/2 ratio was used in all the other cases.

2.2.2 Differential scanning calorimetry (DSC)

Heat capacity curves of a 500 μM DPPE/DPPG suspension were recorded in buffer and in the presence of magnesium chloride, magnesium sulphate, magnesium perchlorate, and the corresponding sodium salts at concentrations of 0.25 M, 0.5 M, and 1 M using a high sensitivity Nano DSC (TA Instruments, New Castle, DE, USA) equipped with 300 μL twin gold capillary cells, pressurized to 3 atm. Every sample was scanned from 25 to 70 °C at least four times, using a scanning rate of 1 °C/min. For each measurement a background blank was subtracted and the thermograms were analyzed by means of the NanoAnalyze software provided by the manufacturer. Excess heat capacity curves were normalized to total lipid concentration

2.2.3 Fluorescence spectroscopy

Fluorescence spectroscopy measurements were carried out on a K2 multifrequency phase modulation fluorometer (ISS Inc., Champaign, IL, USA), equipped with a variable temperature and a high-pressure optical cell equipped with sapphire windows allowing pressure dependent measurements up to about 2 kbar. The Laurdan probe was embedded into POPE/POPG vesicles in a 1:30 probe:lipid ratio. To monitor changes in lipid order parameter/hydration level, and thus the lipid phase of the membrane, the generalized polarization parameter GP was used. The GP value is defined as $GP = (I_{440} - I_{490})/(I_{440}+I_{490})$ where I_{440} and I_{490} are the intensities at 440 nm and 490 nm, respectively of the Laurdan emission spectrum. A low GP value is associated with a more hydrated fluid state of the lipid membrane, while a high GP value (around 0.5) is associated with a less hydrated ordered (gel) state of the lipid bilayer[147,151]. Laurdan emission spectra were recorded in the 390-580 nm range with an excitation wavelength of 340 nm and both excitation and emission slits set to 8 nm. A total lipid concentration of 50 μM was used in buffer and in the presence of 0.25, 0.5, and 1 M salt concentration.

2.2.4 Enzyme kinetics

In the enzyme kinetics experiment, the fluorogenic analogue of the PLA2 substrate PC, DBPC, was used. The fluorescent probe BODIPY in the sn-1 position is quenched by the 6-Dabcylaminohexanoyl (DBPC) in position sn-2. Once the PLA2 hydrolyses the sn-2 phosphodiester bond, a strong increase in BODIPY fluorescence is observed due to the loss of spatial correlation between the two fluorophores. The measurements were performed on the same K2

multifrequency phase modulation fluorometer reported above. Fluorescence measurements were performed using an excitation wavelength of 488 nm, with kinetic data acquired at the emission wavelength of 518 nm. Both emission and excitation slits were set to 8 nm, the time-step kinetics to 1 s, and the temperature was set to 35 °C. The pressure-dependent kinetic measurements were performed using an enzyme concentration of 0.01 μM, with the lipid concentration fixed at 150 μM, monitoring the fluorescence changes for a period of 1800 s.

2.2.5 Confocal microscopy

For confocal fluorescence microscopy imaging, the laser combiner Oxxius Simply Light, 4Cc-CSB130 (Lannion, France) in combination with a mercury-vapor lamp (Hg 100 W, Nikon, Tokyo, Japan) and the objective lens type CFI Plan Apochromat Lambda 100x Oil, NA 1.45, WD 0.13 (Nikon, Tokyo, Japan) were used. GUVs were grown in a 100 mM NaCl solution with 10 mM HEPES buffer at pH 7.4. Salt solutions were added after vesicle growth with a syringe. Images were postprocessed and analysed with the open-source ImageJ software to obtain average size and distribution.

2.2.6 Small-angle X-ray scattering (SAXS)

SAXS measurements were performed on a SAXSess mc^2 instrument from Anton-Paar (Graz, Austria) with a temperature control unit (TCS Control Unit, Anton-Paar, Graz, Austria). The X-ray radiation was generated with a copper X-ray tube, and it was directed onto a quartz capillary cell. The scattering was detected in an evacuated chamber to reduce air scattering for every sample within 30 min via imaging plates in a temperature range of 10-40 °C. The capillary cell was filled

with 10 μL of the 10% w/w lipid suspension. In a typical diffractogram, the appearance of Bragg-peaks within the elastic scattering curve, I(Q), allows the determination of the lamellar repeat distance and provide insight into the lipid phase organization. Q is the modulus of the wave vector transfer, given by $Q = (4/\pi\lambda)\sin\theta$, with 2θ being the scattering angle and λ the wavelength of the X-rays [152]. The type of phase can be distinguished by the characteristic SAXS peak ratios in Q-space (Q1:Q2:Q3: ...). For the lamellar lipid phase, they are equidistant (1:2:3: ...). According to Bragg's equation, the lattice parameter for the lamellar phase is given by $d_{lam} = 2\pi/Q_1$. The lamellar repeat distance, d_{lam}, includes the thickness of the MLV's interlamellar water layer, d_w, and the thickness of the lipid bilayer, d_l, i.e., $d_{lam} = d_w + d_l$

2.2.7 Circular dichroism spectroscopy

Circular dichroism (CD) measurements were performed on a Jasco J-715 spectropolarimeter (Jasco Analytical Instruments, Tokyo, Japan). The spectra were recorded at 35 °C in the 260-200 nm range with 0.5 nm resolution, 4 nm bandwidth, and 2 s of integration time. The spectra were averaged over five accumulations. The protein concentration used was 3 μM.

2.3 Results and discussion

2.3.1 Impact of salts and pressure on the structure and physicochemical properties of bacterial model membranes

To investigate the effects of Mars-relevant salts on the thermotropic properties of a bacterial model membrane, differential scanning calorimetry (DSC) measurements were performed on multilamellar vesicles (MLVs) composed of 1,2-dipalmitoyl-sn-glycero-3-phosphoethanolamine (DPPE) and 1,2-dipalmitoyl-sn-glycero-3-phosphoglycerol (DPPG) in an 8/2 molar ratio. It is worth noting that the DPPE/DPPG mixture was used exclusively for the DSC experiments, as it provides sharper transition peaks and a higher main transition temperature compared to the 1-palmitoyl-2-oleoyl-sn-glycero-3-phosphoethanolamine (POPE) / 1-palmitoyl-2-oleoyl-sn-glycero-3-phospho-1′-rac-glycerol (POPG) mixture employed in all other experiments. Fig. 2.1(A) shows the DSC thermograms of DPPE/DPPG MLVs in neat buffer and in the presence of 0.5 M sulphate and perchlorate salts of sodium and magnesium. For comparison, the effects of NaCl and $MgCl_2$, the salts most relevant to terrestrial biochemistry, are also included. Concentration-dependent DSC profiles are presented in Fig. 2.2.

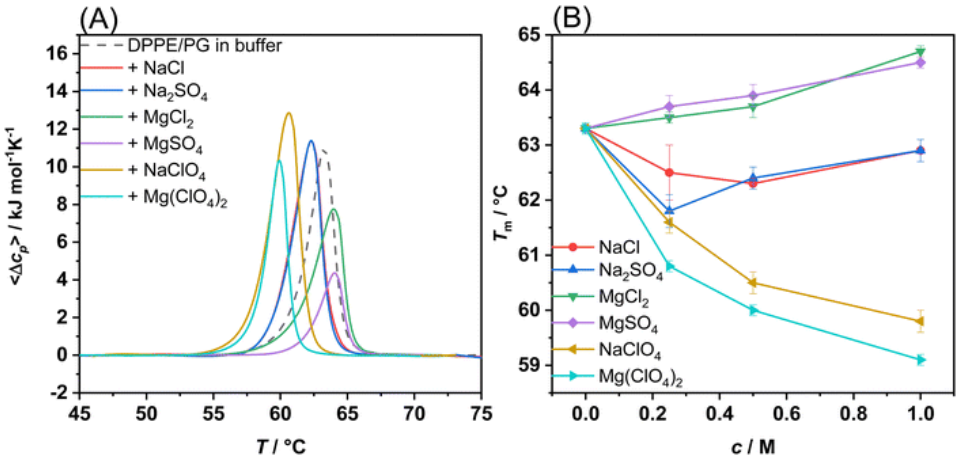

Figure 2.1 (A) DSC traces of DPPE/DPPG (8/2 mol/mol) multilamellar vesicles dispersed in buffer and in the presence of 0.5 M of Mars-relevant salts and NaCl, as indicated in the inset. (B) Gel-to-fluid melting temperatures (T_m) of DPPE/DPPG multilamellar vesicles as a function of salt concentration, c, as inferred from the DSC thermograms reported in panel A and in Fig. 2.2. All the experiments were performed in 10 mM HEPES buffer, pH 7.4.

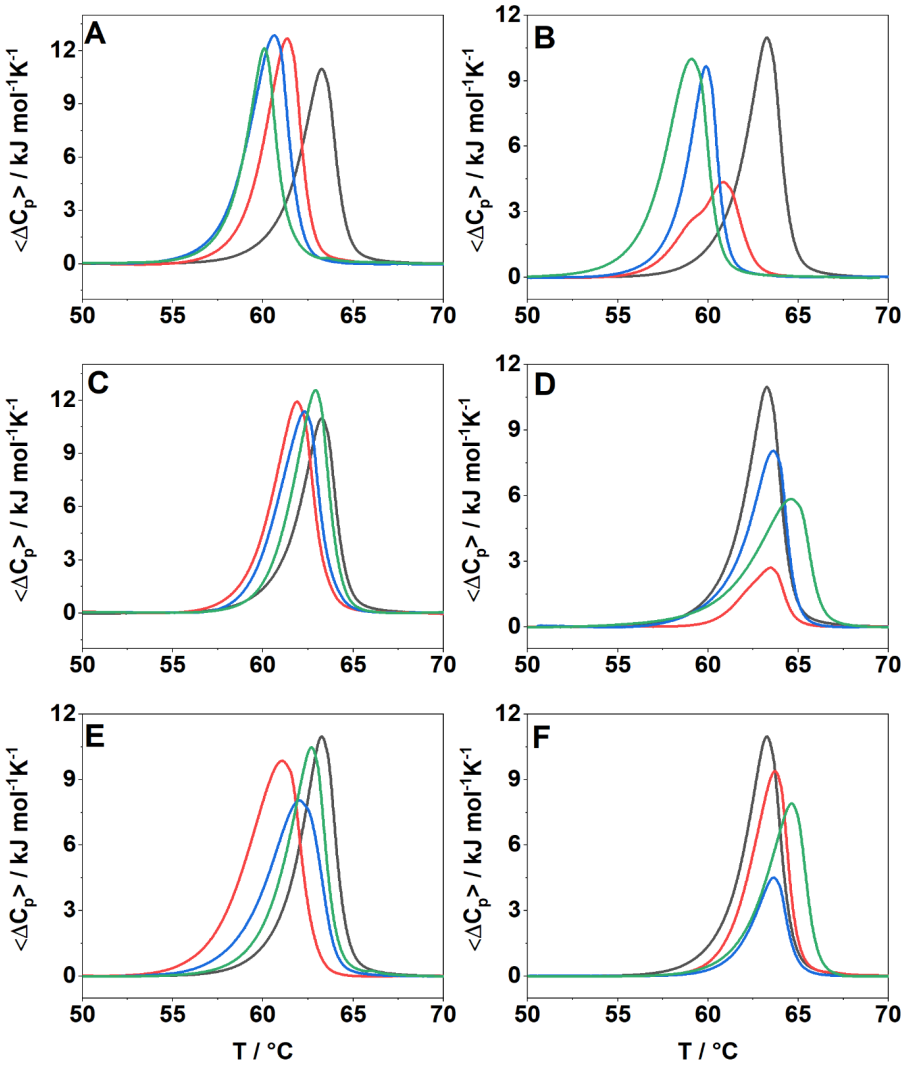

Figure 2.2 DSC traces of DPPE/DPPG in buffer an in the presence of (A) sodium perchlorate, (B) magnesium perchlorate, (C) sodium chloride, (D) magnesium chloride, (E) sodium sulphate, (F) and magnesium sulphate. Salt concentration is: buffer (black line), 0.25M (red line), 0.5 M (blue line), 1 M (green line). All the experiments were performed in 10 mM HEPES buffer, pH 7.4.

The DSC profile of DPPE/DPPG vesicles in neat buffer exhibits a single, well-defined peak, indicating that the two lipids are miscible at the chosen molar ratio[153]. The transition peak, centred at 63.3 °C, corresponds to the phase transition of the lipid acyl chains from the lamellar gel (L_{β}') phase to the liquid-crystalline (L_{α}) phase [154]. Thus, DSC experiments provide insight into the packing of the lipids' hydrocarbon chains. Fig. 2.1(B) presents the melting temperatures (T_m) associated with the gel-to-fluid phase transition of DPPE/DPPG vesicles as a function of salt concentration (*c*). The transition temperature of the DPPE/DPPG mixture is higher than that of the pure lipid components [153], which can be attributed to direct hydrogen bonding between the phosphate and hydroxyl groups of adjacent PE and PG molecules. The presence of PEs mitigates the electrostatic repulsion among PG headgroups, resulting in an increased T_m value for the mixture. Inspection of Fig. 2.1(B) shows that the addition of sodium chloride (NaCl) and sodium sulphate (Na_2SO_4), even at concentrations up to 1 M, exerts only a marginal effect on DPPE/DPPG vesicles, slightly lowering the melting temperature and suggesting minimal perturbation of lipid packing by these salts. In contrast, sodium perchlorate ($NaClO_4$) induces a marked decrease in T_m, like the behaviour observed for phosphatidylcholine vesicles[149]. The T_m value decreases from 63.3 °C in neat buffer to 59.8 °C in 1 M $NaClO_4$. This reduction likely arises from direct interactions between perchlorate and the lipid headgroups (most likely PEs), accompanied by partial penetration of the anion into the hydrophobic chain region. Although perchlorate is negatively charged, its large size and low surface charge density confer a partially hydrophobic character, in sharp contrast to smaller, strongly hydrated anions such as Cl^-. On the other hand, in the presence of Mg^{2+} salts, a different behaviour emerges compared to Na^+ salts. For magnesium chloride and sulphate ($MgCl_2$ and $MgSO_4$), an increase

in T_m of approximately 1.2 °C at 1 M concentration is observed, indicating stabilization of the more tightly packed gel phase of the lipid bilayer. This effect can be attributed to the interaction of the small, highly charged divalent cation with the phosphate moieties of the lipids, particularly the anionic PG headgroups. Conversely, in line with the results observed for the $NaClO_4$, the addition of $Mg(ClO_4)_2$ induces a pronounced decrease in T_m, revealing of gel phase destabilization, mediated by the perchlorate anion. Interestingly, similar trends were found for DPPC vesicles in the presence of $MgSO_4$ and $NaClO_4$, with the notable exception of $Mg(ClO_4)_2$, which abolished the gel-to-fluid transition and led to the emergence of a new phase transition peak at higher temperature. Closer examination of Fig. 2.1 also reveals a clear trend in T_m as a function of salt concentration, while ΔH_m displays more varied behaviour (Fig.2.2). Nonetheless, a general pattern can be discerned: sodium salts cause negligible or slightly positive changes in ΔH_m, whereas all magnesium salts lead to a decrease in ΔH_m. Taken together with temperature-dependent effects, these findings suggest that changes in ΔH_m induced by sodium salts are largely governed by ionic strength, whereas the decrease in ΔH_m observed with magnesium salts is attributable to the cation itself, which may promote less compact lipid packing.

Next, to gain more quantitative information about changes in membrane fluidity upon addition of the salts, fluorescence spectra of the probe Laurdan embedded in the POPE/POPG 8/2 (mol/mol) bilayer were recorded (see Fig. 2.3).

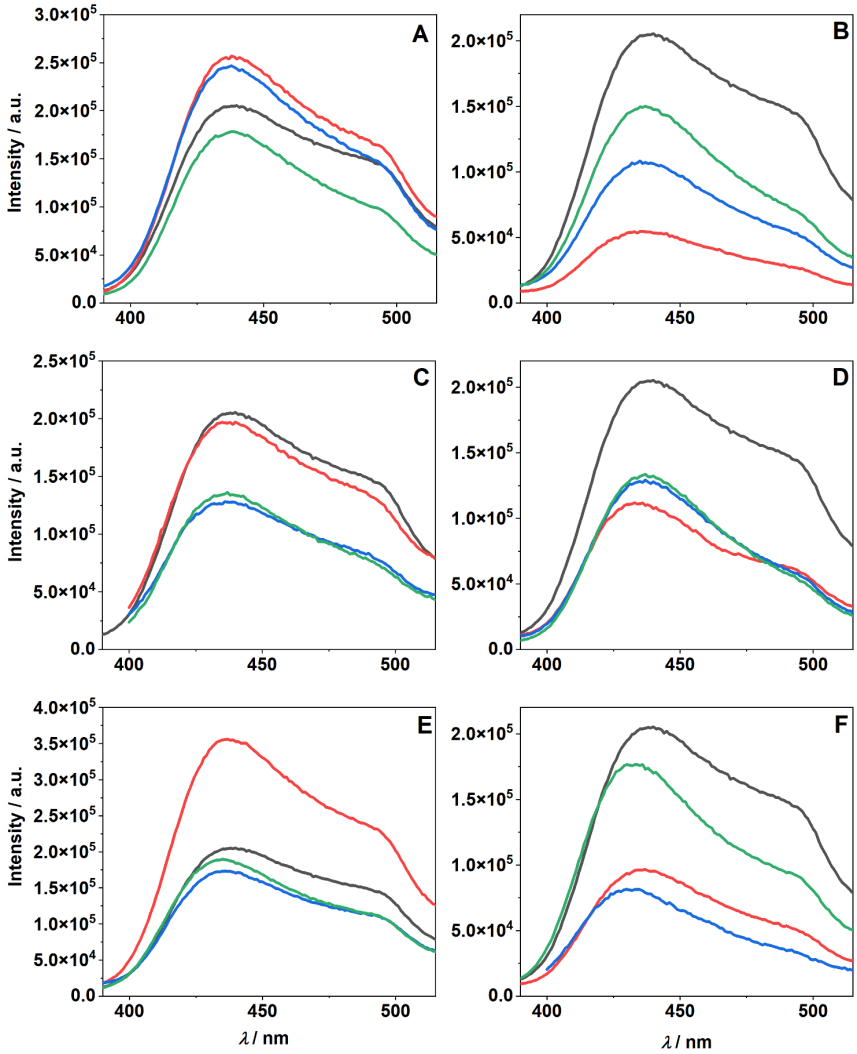

Figure 2.3 Laurdan emission spectra embedded in POPE/POPG bilayer in buffer an in the presence of (A) sodium chloride, (B) magnesium chloride, (C) sodium sulphate, (D) magnesium sulphate), (E) sodium perchlorate, (F) magnesium perchlorate. Salt concentration is 0 (black line), 0.25M (red line), 0.5 M (blue line), 1 M (green line). All the experiments were performed in 10 mM HEPES buffer, pH 7.4.

The probe Laurdan positions itself in the membrane with the fluorescent naphthalene group in close proximity of the glycerol backbone of the lipids. Its fluorescence spectrum is characterized by two well defined emitting states, *i.e.*, a solvent relaxed and a non-solvent relaxed state. The predominance of the emission from one state compared to the other strongly depends on the hydration degree of the membrane which in turn depends on the lipid packing. The emission from the solvent-relaxed state, located at the red edge of the spectrum, is due to Laurdan molecules embedded in a more hydrated and less packed lipid phase, such as the fluid phase of the bilayer. Conversely, the non-solvent relaxed state (at the blue edge of the spectrum) is due to Laurdan being localized in a less hydrated, more densely packed bilayer, such as in the gel phase. To describe the spectroscopic properties of Laurdan, the generalized polarization (*GP,* see materials and methods) parameter can be used. Looking at Fig. 2.3, no clear trends in emission intensity are observed. This lack of consistency could be attributed to several factors, including variations in Laurdan concentration and sample preparation. However, this is not a problem since the GP parameter is a relative measure and does not depend on the absolute intensity. In Fig. 2.4(A), the *GP*-values of Laurdan in the presence of different salts concentrations are shown. The experiments were carried out at the temperature of 35 °C, where the bilayer at neat buffer conditions is in the fluid-like phase.

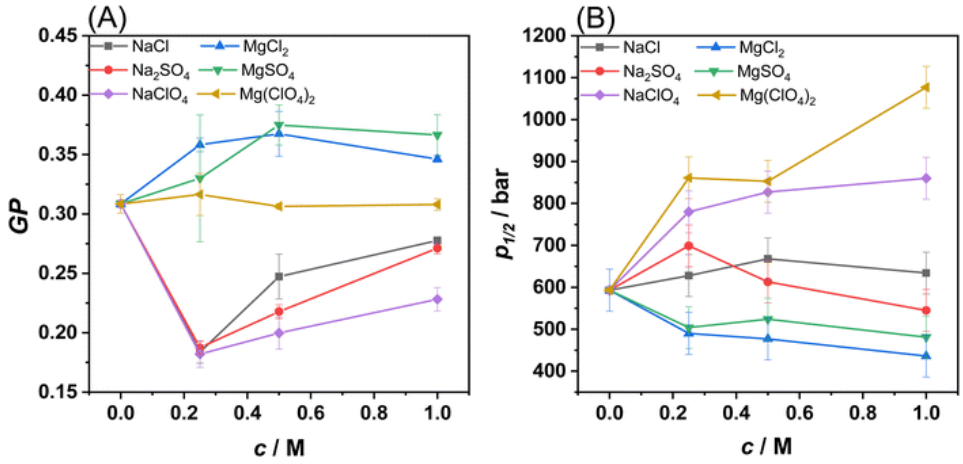

Figure 2.4 (A) *GP*-values of Laurdan embedded in POPE/POPG vesicles at 1 bar as a function of salt concentration. (B) Values of the liquid-to-gel pressure transition pressure, *p*1/2, as a function of salt concentration, *c*. All the experiments were performed in 10 mM HEPES buffer, pH 7.4, at the temperature of 35 °C.

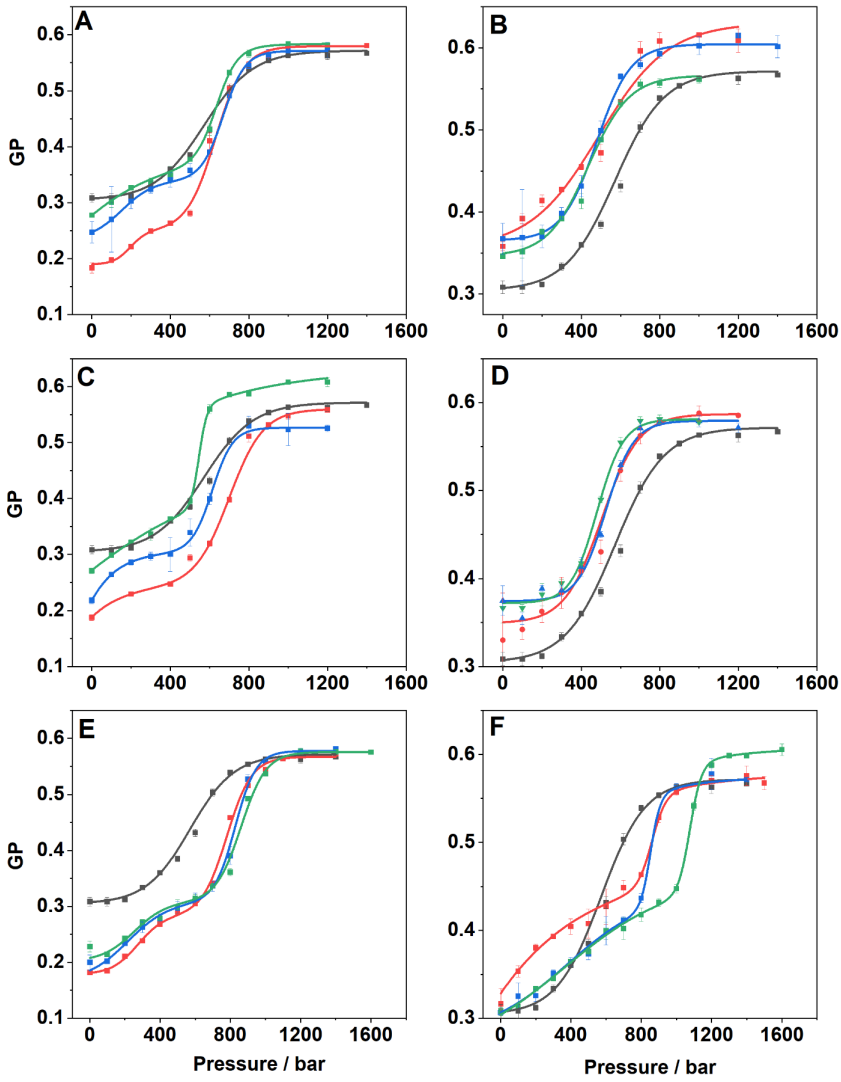

Figure 2.5 GP values reported as a function of pressure for (A) sodium chloride, (B) magnesium chloride, (C) sodium sulphate, (D) magnesium sulphate, (E) sodium perchlorate and (F) magnesium perchlorate. Salt concentration is 0M (black line), 0.25M (red line), 0.5M (blue line), 1M (green line). All the experiments were performed in 10 mM HEPES buffer, pH 7.4, at the temperature of 35 °C.

The presence of sodium salts caused a decrease of the *GP*-values with respect to that observed in neat buffer. The decrease of the *GP* is an indication that the surface of the membrane is more hydrated and less densely packed, in agreement with the DSC results on DPPE/DPPG, where a small decrease of T_m was observed, *i.e.*, the fluid-like phase is slightly favoured over the gel phase. Although the trend of *GP*-values is similar when the sodium salts concentration increases, the magnitude of the effect of perchlorate sodium salt significantly differs from the other sodium salts. Perchlorate is the sodium salt that caused the highest decrease of the *GP*-value. This result is consistent with the ability of perchlorate to partially penetrate the membrane and make it more hydrated and fluid compared to sodium chloride and the sulphate salts. These results are also consistent with the DSC data, showing that sodium perchlorate is better at stabilizing the membrane's fluid phase compared to the other sodium salts. Conversely, in the presence of $MgCl_2$ and $MgSO_4$, a small increase of *GP* was detected, revealing that the surface of the bilayer is less hydrated and that these two salts favour a more compact, densely packed phase, in agreement with the DSC data. Most remarkably, in the presence of $Mg(ClO_4)_2$, no significant changes in the *GP*-value occurred, suggesting that the lipid packing of the bilayer is not affected at all by the salt, even at 1 M concentration. Instead, DSC data on DPPE/DPPG mixture clearly indicate that perchlorate ions decrease the melting temperature of the lipid chains. This effect can be explained considering that Mg^{2+} strongly interacts, through electrostatic interactions, with the phosphate groups of lipids, stabilizing the bilayer. On the other hand, the perchlorate partially penetrates inside the hydrophobic core of the membrane, leading to a fluidizing effect. These two effects counterbalance each other, leading to the observed result.

Then, using the same methodology, the combined effect of salts and HHP was explored. Fig. 2.5 shows the *GP*-values for the different salts in the pressure range from 1 to 1400 bar. The *GP vs. p* plots for the POPE/POPG vesicles in buffer shows the characteristic sigmoidal behaviour describing a pressure-induced liquid-to-gel phase transition [152,155]. On the contrary, it is interesting to note that not all systems exhibit a sigmoidal transition. In some cases, a gradual increase in GP (reflecting membrane stiffening) is observed prior to the inflection point of the curve, which marks the transition to the gel phase. The inflection points of these curves, *i.e.* the transition pressure $p_{1/2}$, as a function of salt concentration is shown in Fig. 2.4(B) for all salts. The $p_{1/2}$ value for POPE/POPG vesicles in neat buffer is ~600 bar, in agreement with the typical value of ~20 °C bar^{-1} observed for the fluid-to-gel transition slope of phospholipids. In the presence of NaCl and Na_2SO_4, the $p_{1/2}$ value remains essentially constant in the whole concentration range explored. Instead, in the presence of $NaClO_4$, a progressive increase of $p_{1/2}$ on increasing the salt concentration was observed. At 1 M $NaClO_4$, $p_{1/2}$ increased to ~850 bar. These data are consistent with the DSC data suggesting stabilization of the fluid phase. The perchlorate anion penetrates the hydrocarbon chains, thereby hampering efficient packing of the lipid chains, which causes a drastic increase of the pressure needed to induce the gel phase. In the presence of $MgCl_2$ and $MgSO_4$, a small decrease of $p_{1/2}$ was observed, indicating a slight destabilization of the gel phase, again, in agreement with the DSC data. When the perchlorate salt of Mg^{2+} is present in solution, the $p_{1/2}$ value increased markedly, reaching a value of ~1100 bar at 1 M concentration, signifying a strong stabilization effect of the fluid-like phase mediated by perchlorate. This is a remarkable result as the fluidizing effect occurred even in the presence of the Mg2+ cation, which generally promotes

denser lipid packing. On the other hand, a *GP*-value around 0.3 in neat buffer already indicates rather efficient lipid packing.

Taken together, the DSC and fluorescence data demonstrate that sodium chloride and sodium sulphate exert negligible effects on the stability of PE/PG lipid bilayers, even at molar concentrations. In contrast, the magnesium salts of chloride and sulphate induce a slight stabilization of the bilayer, promoting the formation of the ordered gel phase. Remarkably, both sodium and magnesium perchlorates strongly destabilize the ordered state, instead favouring the fluid-like phase through partial penetration of ClO_4^- anions into the hydrophobic core of the bilayer. This fluidizing effect is dominant and persists regardless of the counterion, with Mg^{2+} unable to counteract the influence of ClO_4^- anions.

2.3.2 The impact of Mars-like salts on the mesophase structure and topology of lipid vesicles

To gain insights into the effect of the Mars-relevant salts on the morphology of the lipid vesicles, confocal fluorescence microscopy measurements were carried out. Giant unilamellar vesicles (GUVs) composed of POPE/POPG 8/2 mol/mol containing the fluorescent lipid probe N-Rh-DHPE were used. Fig. 2.6 depicts GUVs of POPE/POPG before and after the addition of the salts at a concentration of 0.5 M.

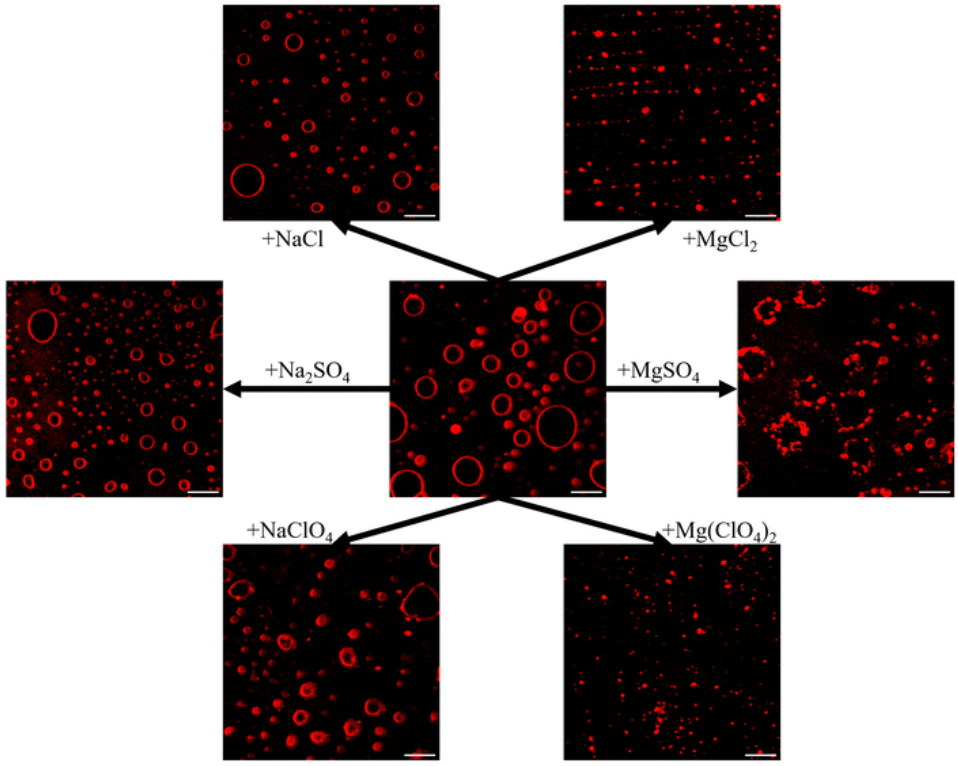

Figure 2.6 Fluorescence confocal microscopy snapshots of GUVs of POPE/POPG grown in the presence of 100 mM NaCl and 10 mM HEPES buffer pH 7.4, before and after the addition of the Martian salts at the concentration of 0.5 M. The reported scale bars are 20 μm. Each experiment has been performed at least twice.

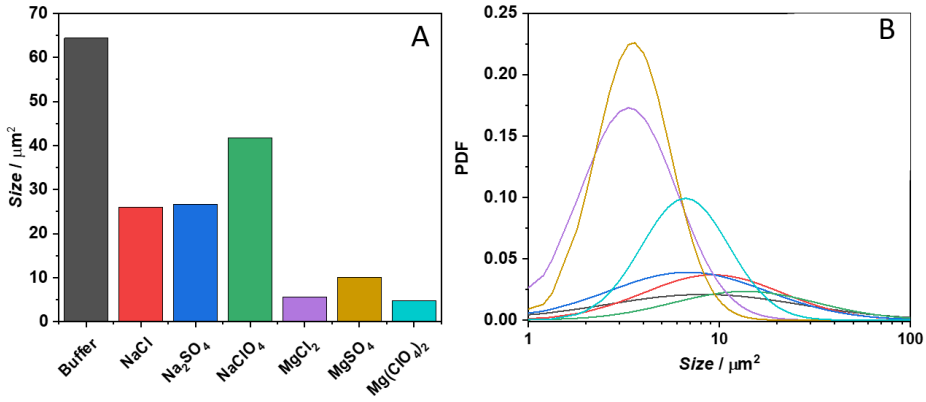

Figure 2.7 (A) average size of GUVs after the addition of the indicated salt (B) Distribution of the GUVs size for buffer (black line), sodium chloride (red line), sodium sulphate (blue line), sodium perchlorate (green line), magnesium chloride (violet line), magnesium sulphate (ochre line), magnesium perchlorate (turquoise line).

After the application of the electroformation protocol, spherical µm-sized GUVs were obtained, where the contour of GUVs is clearly visible due to the presence of rhodamine-labeled PE. Upon addition of NaCl and Na_2SO_4, no significant changes in the morphology of the GUVs were observed: their spherical shape remained intact. The average size and size distribution of the vesicles were determined by analysing multiple images (Fig. 2.7). The vesicle populations were heterogeneous, with narrower size distributions observed for Mg^{2+} salts compared to Na^+ salts (Fig. 2.7). The average vesicle area was 25.9 and 26.6 µm² for NaCl and Na_2SO_4, respectively, with maximum areas of 297 and 358 µm². In contrast, the presence of $NaClO_4$ caused pronounced morphological alterations, with the vesicles appearing fluffy and deformed. This deformation likely results from perchlorate anions penetrating the membrane, leading to a reduction in the bilayer bending modulus (i.e., elasticity) [156]. This observation aligns with the

calorimetric and spectroscopic data discussed above, which indicated a less densely packed membrane structure. Interestingly, despite these morphological changes, the average vesicle area in $NaClO_4$ (41.6 μm²) was comparable to those observed with the other sodium salts. Overall, GUVs exposed to Na^+ salts were smaller on average than those in neat buffer (64.3 μm²). Conversely, all Mg^{2+} salts induced drastic changes in vesicle morphology. Their presence led to remarkable vesicle shrinkage, reducing the average area to 5.6, 10.0, and 4.8 μm² for $MgCl_2$, $MgSO_4$, and $Mg(ClO_4)_2$, respectively, with maximum areas below 27 μm². This effect can be attributed to osmotic stress and, in the case of $MgSO_4$, to clustering of smaller vesicles. Vesicle association is likely promoted by Mg^{2+} coordination with the lipid headgroup region, which reduces electrostatic repulsion between negatively charged liposomes. Similar effects have been reported for DOPC vesicles in the presence of magnesium salts, suggesting that vesicle shrinkage occurs regardless of membrane charge[149]. Importantly, despite the observed morphological changes, bilayer integrity remains preserved, as confirmed by calorimetric and spectroscopic analyses. In biological contexts, bacteria have evolved mechanisms to cope with severe osmotic fluctuations, such as the uptake or biosynthesis of compatible osmolytes, implying that salt-induced osmotic stress may not necessarily pose a severe physiological challenge.

In the end, temperature-dependent small-angle X-ray scattering (SAXS) experiments were carried out on corresponding multilamellar vesicles to reveal changes in the lamellarity of the MLVs and to check if the bilayer structure is still preserved at high salt concentrations, or if phase transitions to other lipid structures (*e.g.*, hexagonal, cubic or micellar lipid phases) are induced. As an example, Fig. 2.8(A) shows the SAXS patterns of POPE/POPG MLVs at selected temperatures under neat buffer conditions while Fig.2.9 shows the diffractograms

obtained in the presence of the salts. SAXS data allow for the determination of lamellar distance constants of MLVs by the appearance of Bragg-peaks in the elastic scattering curve, $I(Q)$, as described in the experimental section. Higher-order Bragg reflections are observed for the lower temperatures only, as the multi-lamellarity is largely lost at higher temperatures due to increasing thermally induced fluctuations.

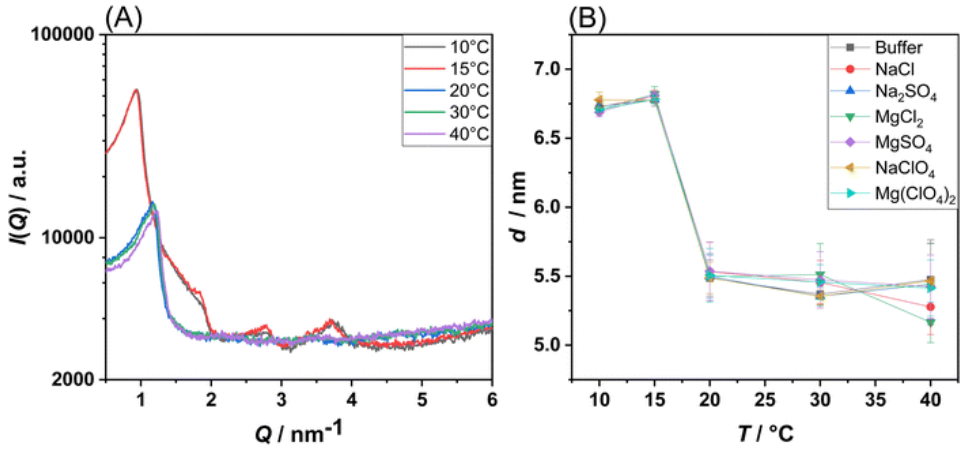

Figure 2.8 (A) SAXS intensity, $I(Q)$, of POPE/POPG multilamellar vesicles at neat buffer conditions recorded at the indicated temperatures. (B) Lamellar spacing, d, of POPE/POPG multilamellar vesicles in buffer and in the presence of the Mars-relevant salts at a concentration of 0.5 M. All the experiments were performed in 10 mM HEPES buffer, pH 7.4. Each experiment has been performed at least twice.

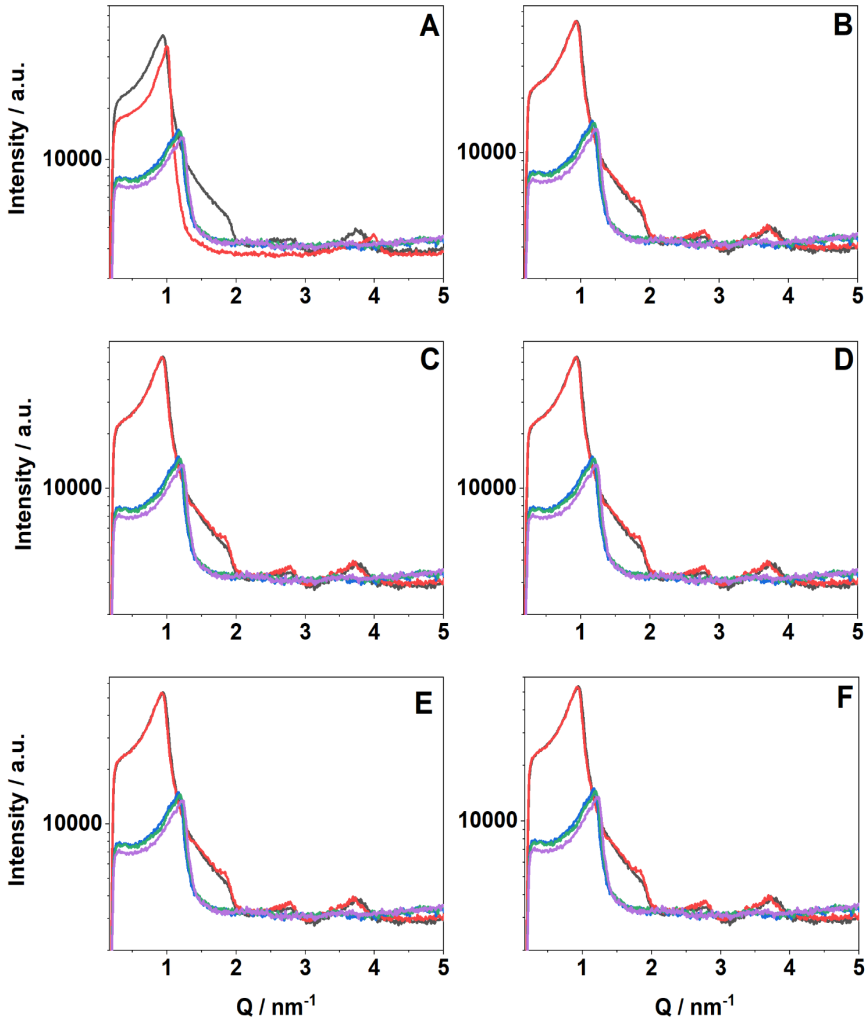

Figure 2.9. SAXS intensity, $I(Q)$, of POPE/POPG multilamellar vesicles in the presence of sodium chloride (A), magnesium chloride (B), sodium sulphate (C), magnesium sulphate (D), sodium perchlorate (E), magnesium perchlorate (F). Intensities are reported at 10°C (black line), 15°C (red line), 20°C (blue line), 30°C (green line), 40°C (violet line).

For all salt conditions, a lamellar lipid phase was recorded, both in the gel and in the fluid-like state. This is an interesting result, since in a previous work the

induction of a bicontinuous inverse cubic lipid phase was suspected in DPPC liposomes in the presence of high concentrations of $Mg(ClO_4)_2$ [149]. In the present case, for a prototypical bacterial PE/PG membrane, the presence of such phase was not observed. This highlights the possibility that the bacterial membrane could still exist in the lamellar phase under such harsh Martian salt conditions, a prerequisite for the development of bacterial-based life [23]. Fig. 2.8(B) shows the temperature dependence of the lamellar *d*-spacing in the absence and presence of the Mars-relevant salts. For POPE/POPG vesicles in the gel phase, a value of d = 6.75 nm was obtained, which decreases to ~5.5 nm in the fluid phase, a typical value for such bilayers in their fluid-like state[157]. The decrease of d can be explained by the much smaller length of the acyl chains in their disordered fluid state and a decrease of the interlamellar water layer. Interestingly, it seems that the lamellar repeat distance is not significantly affected by the presence of the salts.

2.3.3 Effects of Mars-like salts and pressure on a model enzymatic reaction

Finally, to demonstrate how the presence of Mars-relevant salts, in combination with elevated hydrostatic pressure, can modulate biologically relevant reactions, the kinetics of phospholipid hydrolysis catalysed by bee venom phospholipase A2 (PLA2) were investigated[150,158]. PLA2 is an esterase that catalyes the hydrolysis of membrane glycerophospholipids at the *sn*-2 position, producing a free fatty acid and a lysophospholipid containing a single hydrophobic chain (Fig. 2.11(A))[159,160]. Prior to conducting the enzymatic assays, it was essential to verify whether the salts used affected the conformation and stability of the enzyme, as

these parameters directly influence catalytic activity. To this end, circular dichroism (CD) spectra of PLA2 were recorded in the far-UV region (200–260 nm), providing information on the protein's secondary structure elements[161]. (Fig. 2.10) shows the CD spectra of PLA2 in neat buffer and in the presence of sodium and magnesium salts at a concentration of 0.5 M.

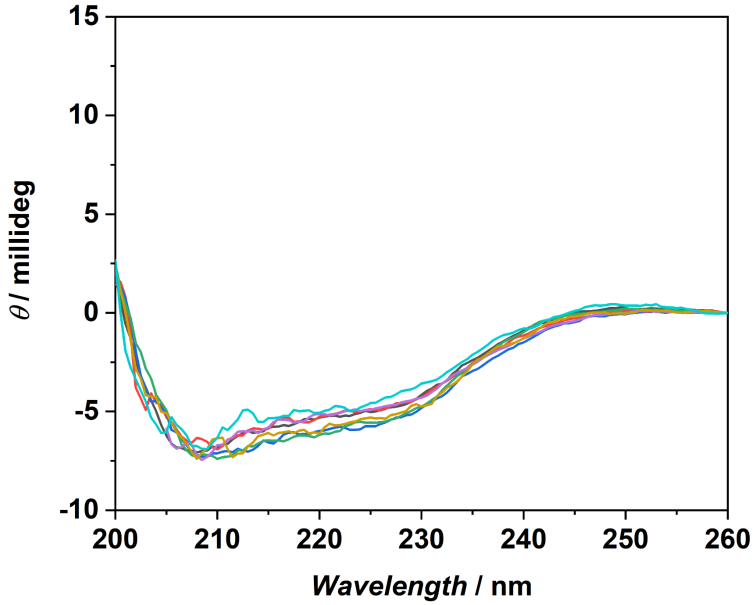

Figure 2.10 CD spectra of PLA2 in buffer (black line), sodium chloride (red line), sodium sulphate (blue line), sodium perchlorate (green line), magnesium chloride (violet line), magnesium sulphate (ocher), magnesium perchlorate (turquoise).

The CD spectrum of PLA2 in neat buffer shows two minima at around 208 and 230 nm, which indicate that the protein adopts mainly an α-helical structure, in

accordance to literature data[150,159]. The intensity of the minimum at 230 nm is lower with respect to that at 208 nm, revealing the presence of other secondary structure elements, β-sheets and loops. Upon addition of the Mars-relevant salts, no significant changes were observed, *i.e.*, the integrity of the protein's structure seems to be preserved at high salt. As pressure dependent activity studies are carried out as well, also the pressure resistance of the enzyme must be confirmed. Indeed, in a previous study employing high-pressure FTIR spectroscopy, it has been demonstrated that the enzyme structure is stable at pressures below 4 kbar.

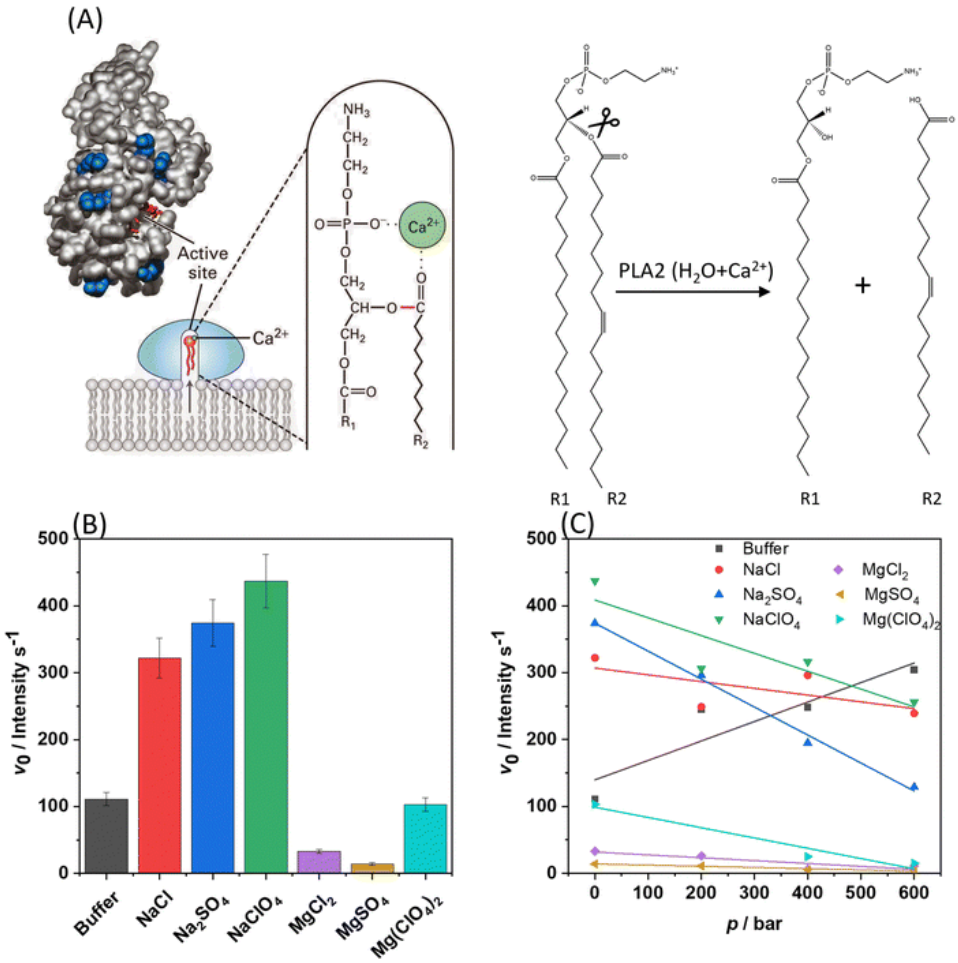

Figure 2.11 (A) Left: Interfacial binding and mechanism of PLA2 action. A small conformational change in phospholipase A2 induced by binding to the water–lipid interface opens a hydrophobic channel and fixes the protein to the phospholipid heads. The Ca^{2+}-containing active site is buried in a channel enriched with hydrophobic amino acids facilitating protrusion of a phospholipid from the bilayer to the catalytic site. Right: Hydrolysis of the *sn*-2 ester of phospholipid yields a free fatty acyl chain (R2), leaving a lysophospholipid molecule behind (R1)[158]. (B) Initial velocity (v_0) plots for the hydrolysis reaction (fluorescence intensity per s), at 1 bar and 35 °C, carried out by PLA2 on DBPC

embedded in POPE/POPG vesicles in neat buffer and in the presence of 0.5 M of the Mars-relevant salts, as indicated in the plot. (C) v_0-values for the same reaction in the presence of 0.5 M salts as a function of pressure. For $Mg(ClO_4)_2$, the v_0-value at 200 bar was discarded due to its large error bar. All the experiments were performed in 10 mM HEPES buffer, pH 7.4.

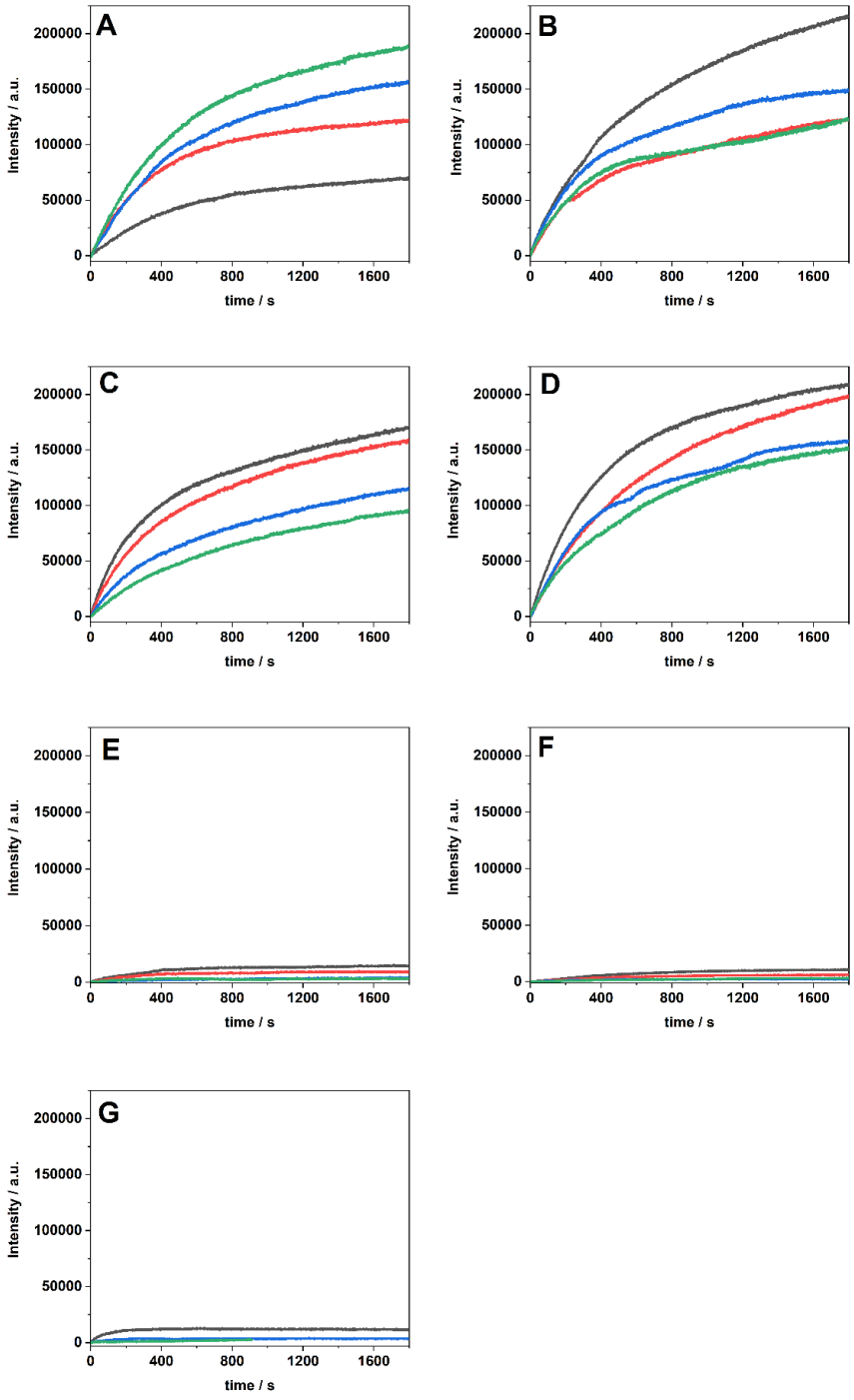
A
B
C
D
E
F
G
Intensity / a.u.
time / s
0
50000
100000
150000
200000
400
800
1200
1600

Figure 2.12 Pressure dependent kinetic curves of POPE/POPG hydrolysis in (A) buffer, (B) sodium chloride, (C) sodium sulphate, (D) sodium perchlorate, (E) magnesium chloride, (F) magnesium sulphate, (G) magnesium perchlorate. Salt concentration was 0.5 M. Pressure is 1 bar (black line), 200 bars (red line), 400 bars (blue line), 600 bars (green line).

Once the structural stability of the enzyme was assessed, the kinetics of the hydrolysis of phospholipids mediated by PLA2 was measured (Fig. 2.11(B)). To this end, liposomes composed of POPE/POPG with 1% mol of the fluorescence probe DBPC was used. In this probe, the fluorescent molecule BODIPY is covalently attached to the hydrocarbon chain in position *sn*-1. The hydrocarbon chain at position *sn*-2 contains the molecule DABCYL, which acts as a nearby quencher of the fluorescence emission of BODIPY. Upon hydrolysis of the ester bond at position *sn*-2 by PLA2, the DABCYL-labelled fatty acid is released. This leads to an increase in the fluorescence intensity of the BODIPY fluorophore, which serves as a real-time readout of enzymatic activity and enables kinetic monitoring of the reaction. To quantitatively evaluate the kinetics of the hydrolysis reaction, the slope of the linear portion of the fluorescence intensity *vs.* time plot was determined, *i.e.*, the initial velocity *v*0 of the enzyme reaction. Fig. 2.12 shows examples of the kinetic plots of the hydrolysis reaction. Fig. 2.11(C) shows the v_0-values obtained for all salts at 1 bar and 25 °C. In these experiments, the concentration of the enzyme was fixed at 0.01 μM, the total lipid concentration was 150 μM, and the salt concentration was 0.5 M. Remarkably, compared to the reaction rate (v_0) in neat buffer, the addition of all sodium salts led to a significant enhancement of the hydrolysis kinetics. The general trend followed the order NaCl ≤ Na_2SO_4 ≤ $NaClO_4$, although the differences among the three sodium salts were relatively small. The kinetics of PLA2-catalyzed hydrolysis is known to depend

on several membrane properties, including lipid composition, charge density, fluidity, bending modulus, and, consequently, the phase state of the bilayer[162,163]. Since two water molecules are directly involved in the catalytic mechanism, the level of membrane hydration is also an important determinant[164,165]. As inferred from the *GP*-data presented above, the POPE/POPG bilayer becomes more hydrated and less densely packed in the presence of sodium salts, particularly $NaClO_4$. Hence, the observed enhancement of the reaction rate can be attributed to bilayer fluidization induced by the salts, accompanied by an increase in hydration of the lipid headgroup region, as supported by the Laurdan fluorescence results. In contrast, the presence of $MgCl_2$ and $MgSO_4$ resulted in significantly lower v_0 values compared to those in neat buffer, indicating that the divalent cation strongly suppresses the hydrolysis rate. Both salts promote a more tightly packed and less hydrated bilayer (as shown by the Laurdan data in Fig. 2.4), thereby reducing membrane accessibility to the enzyme and limiting the availability of water molecules required for catalysis. Moreover, the strong coordination of Mg^{2+} with the negatively charged lipid headgroups may further diminish PLA2 binding affinity by lowering the membrane's surface charge density. Indeed, previous studies have shown that negatively charged lipids enhance PLA2 activity by facilitating enzyme binding to the membrane: the crucial initial step in its catalytic mechanism[166]. Although the CD spectra revealed no global conformational change of PLA2 in the presence of Mg^{2+} salts, minor local rearrangements (e.g., within the active site) or subtle tertiary-structure perturbations cannot be excluded and may contribute to the observed decrease in enzymatic rate. Interestingly, in the presence of $Mg(ClO_4)_2$, the reaction rate was comparable to that in neat buffer, consistent with the calorimetric and spectroscopic data showing that $Mg(ClO_4)_2$ promotes a more hydrated and less ordered bilayer. In this case, the chaotropic

effect of the perchlorate anion outweighs the condensing influence of Mg^{2+}, restoring the enzymatic activity observed under control conditions. Notably, previous studies have reported that both $NaClO_4$ and $Mg(ClO_4)_2$ typically decrease the reaction rate in other enzyme–substrate systems[14,98,167]. In contrast, our results demonstrate the opposite trend, indicating that specific salt–membrane interactions can enhance PLA2 activity. This finding is particularly relevant to the adaptive strategies of halophilic organisms, which can survive and function in environments rich in Mars-relevant salts [18,168,169]. The same experiments were subsequently performed as a function of hydrostatic pressure under conditions where the bilayer remained in its biologically relevant fluid-like state ($p < 600$ bar). The results for $v_0(p)$ are shown in Fig. 2.11(C). Within this pressure range, PLA2 retains its native conformation[150]. In neat buffer, the hydrolysis rate of PLA2 on POPE/POPG membranes increased with increasing pressure. The pressure dependence of the initial velocity is governed by the binding volume (ΔV_b) and activation volume ($\Delta V^{\#}$) of the reaction. According to Le Châtelier's principle, pressure favours the state with the smallest overall volume[170,171]. ΔV_b represents the partial molar volume difference between the enzyme–substrate complex and the unbound state, while $\Delta V^{\#}$ reflects the volume difference between the transition-state complex ($ES^{\#}$) and the ground-state complex (ES). These parameters depend not only on the enzyme–substrate system but also on bilayer composition, lipid packing, headgroup charge, and hydration. In the presence of sodium salts, the reaction rate decreased markedly with increasing pressure, although the values remained comparable to those in neat buffer at ambient pressure. Thus, the reaction still proceeds under these harsh salt and pressure conditions, albeit at a reduced rate. The slowdown of v_0 under high hydrostatic pressure (HHP) can be attributed to enhanced lipid packing induced by

compression. High-pressure ^2H NMR studies have shown that in fluid phospholipid membranes, the lipid chain length increases only modestly (~1.1 Å $kbar^{-1}$), whereas the chain cross-sectional area decreases substantially (~10 $Å^2$ $kbar^{-1}$)[170,172]. Similarly, the lateral self-diffusion constant of fluid lipid vesicles decreases by ~25% with a pressure increase of 1 kbar, with even larger reductions upon transition to the pressure-induced gel phase[170,172]. Remarkably, $NaClO_4$, through its bilayer-fluidizing effect, partially offsets this compaction, resulting in reaction rates comparable to those observed in buffer. By contrast, Mg^{2+} salts of chloride and sulphate caused a pronounced decrease in reaction rate, which diminished further with increasing pressure. This trend reflects the combined effects of pressure and Mg^{2+} binding, both of which promote a more compact and rigid bilayer. Notably, v_0 in $NaClO_4$ remained higher than in $Mg(ClO_4)_2$. For $NaClO_4$, the chaotropic anion dominates the modulation of enzymatic kinetics, whereas in $Mg(ClO_4)_2$, the disruptive influence of ClO_4^- is counterbalanced by Mg^{2+}–headgroup coordination, which enhances bilayer ordering. Pressure further amplifies this ordering effect, leading to slower reaction kinetics in magnesium perchlorate compared to sodium perchlorate.

2.4 Conclusions

In this work, the effect of Mars-relevant salts on the microscopic, mesoscopic, and functional properties of lipid bilayers composed of the bacterial lipids phosphatidylethanolamine (PE) and phosphatidylglycerol (PG) was investigated. These two lipids are the most abundant in bacteria such as *E. coli*, and vesicles with a PE/PG molar ratio of 8:2 provide a representative model of the inner bacterial membrane. Using a multi-technique approach, it was possible to

disentangle how Mars-relevant salts influence the structural organization, lipid packing, hydration, and morphology of these model membranes. To mimic the conditions expected in the Martian subsurface, experiments were also conducted under high-pressure conditions in combination with elevated concentrations of perchlorate and sulphate salts, reproducing the extreme environment of subsurface Martian brines. To assess the functional implications of these conditions, the hydrolysis rate of phospholipase A2 (PLA2), a membrane-associated enzyme, was measured. Our findings clearly demonstrate that chloride, sulphate, and perchlorate salts have distinct effects on bilayer properties, which also strongly depend on the type of counterion present (Na^+ vs. Mg^{2+}). Among these, perchlorate salts, thought to be the most abundant salts on Mars, induce bilayers that are more hydrated and less ordered, thereby strongly favouring the fluid-like phase even under high-pressure stress. Maintaining a fluid membrane is essential for supporting biochemical processes fundamental to life. Interestingly, the lamellar organization of the bacterial model membrane remained stable even under these extreme salt conditions, contrasting with the behaviour of model eukaryotic plasma membranes. Finally, it was demonstrated that PLA2 activity is strongly modulated by both high hydrostatic pressure and salt composition, with the specific effects depending on the nature of the anion and cation. Remarkably, in the presence of the chaotropic perchlorate anion, the enzyme remained active at a reasonable rate even when Mg^{2+}, was present and under high-pressure conditions (Fig. 2.13). Overall, these results support the hypothesis that a functional, fluid, and lamellar bacterial-type membrane could persist in the highly stressed environments of Martian subsurface brines, suggesting that bacterial life may be sustainable under such harsh extraterrestrial conditions.

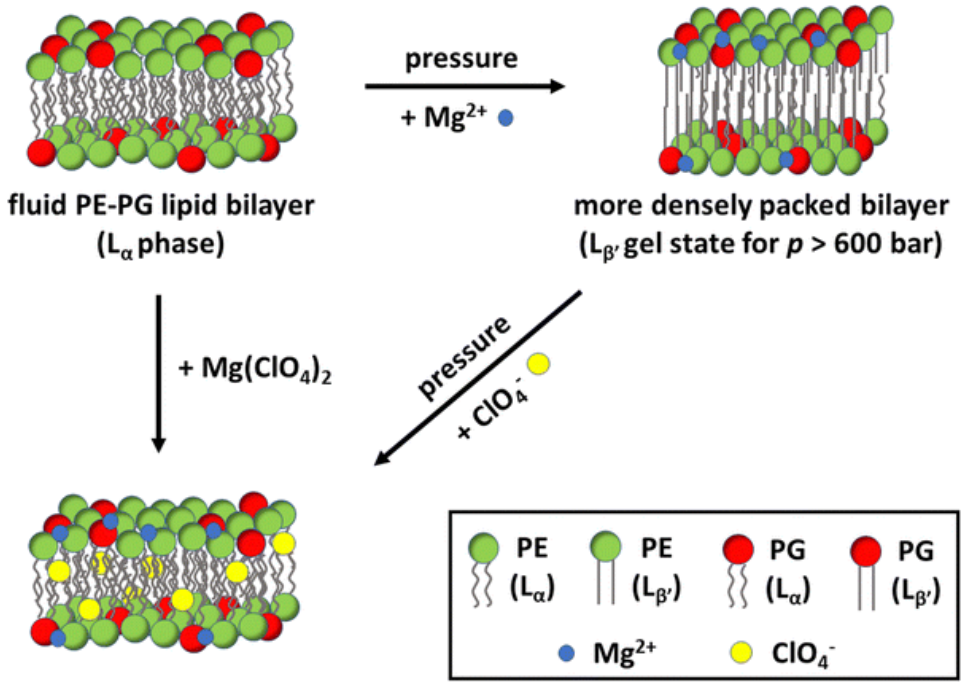

Figure 2.13 Schematic representation of a bacterial model membrane composed of POPE and POPG, illustrating the effects of high pressure, Mg^{2+}, and ClO_4^- on lipid bilayer packing and fluidity. Under ambient pressure, the bilayer exists in a fluid-like (Lα) phase. Increasing pressure promotes tighter packing of the lipid acyl chains, and beyond approximately 600 bar, drives a transition to the more ordered Lβ′ gel phase. In the presence of salts, Mg^{2+} cations (blue circles) interact with the lipid head groups, enhancing lipid packing. Conversely, chaotropic ClO_4^- anions (yellow circles) partially penetrate the hydrophobic core of the bilayer, increasing acyl chain disorder. When both ions are present as $Mg(ClO_4)_2$, the fluid-like phase is stabilized even under high-pressure conditions, delaying the fluid-to-gel transition until around 1.1 kbar. Since optimal PLA2 activity depends on a fluid-like bilayer, enzymatic function remains preserved even in 0.5 M $Mg(ClO_4)_2$ under high-pressure stress.

Chapter 3 - Impact of Martian relevant salts on a model protein-ligand system

3.1 Introduction

Protein-substrate interactions are vital for biological functions and are highly sensitive to their aqueous environment, particularly dissolved salts. Salts influence binding by affecting water activity, hydration, electrostatics, and conformational stability. Chaotropic salts like perchlorates destabilize proteins, while cosmotropic salts such as sulphates rigidify them, impacting binding affinity [173–176]. Understanding these effects is crucial for assessing biochemical viability in extraterrestrial environments like Mars and Europa, which have extreme conditions, low temperatures and high salt concentrations, that challenge biomolecular stability [8,177,178]. Instead of replicating the full complexity of these environments, this work focuses on how specific salts, found or inferred on Mars and Europa, affect protein-ligand interactions. Lysozyme–NAG3 system was chosen as a model due to its well-characterized structure, catalytic mechanism, and binding thermodynamics. This system allows for direct study of recognition without enzymatic complexities [173,174,179,180].

Using physicochemical techniques, the impact of Martian and Europa-relevant salts, magnesium perchlorate, magnesium sulphate, magnesium chloride, and sodium chloride, on lysozyme-NAG3 binding was determined. High concentration of magnesium perchlorate allow liquid water down to -70°C, while both magnesium chloride and sulphate contributed to transient Martian brines. On

Europa, theoretical models predict $MgCl_2$ and $MgSO_4$ from water-rock interactions [14,181–194]. Given the high salt concentrations expected in Martian brines, salt concentration is set at 0.5M for the experiments. This study, using a combined spectroscopic and calorimetric approach, offers new insights into biomolecular behaviour in salt-rich extraterrestrial environments, contributing to protein–ligand interaction research.

3.2 Experimental section

3.2.1 Chemicals

The protein lysozyme (Lyz) from chicken egg white with a purity >90 % was purchased from Merck (Darmstadt, Germany). The ligand, N, N′, N″-triacetylchitotriose (NAG3) with a purity >93% and the fluorophore 8-anilinonaphthalene-1-sulfonic acid (ANS) with a purity >90% were also obtained from Merck. Sucrose and all the salts used in this study: magnesium chloride, magnesium sulphate, magnesium perchlorate and sodium chloride were acquired from Merck, each with a purity >99.0%.

3.2.2. Sample preparation

All stock solutions were prepared in 0.1 M sodium acetate buffer at pH 5.0. Each sample was prepared diluting appropriate amounts of salt, Lyz and NAG3 from stock solution. In these conditions water activity was estimated to be well above 0.95[195,196].

3.2.3 Isothermal Titration Calorimetry

Isothermal titration calorimetry (ITC) measurements were performed on a Malvern Microcal PEAQ-ITC instrument equipped with a 200 μL gold cell and 40 μL syringe. All experiments have been performed titrating a 250 μM lysozyme solution with a 2.5 mM NAG3 solution in the presence and absence of salt, except for magnesium perchlorate which was performed with a 3.5 mM NAG3 solution and 350 μM lysozyme solution. Salt concentration was 0.5 M in both the vessel and the syringe to ensure identical buffer conditions. The samples were stirred for five minutes under vacuum to ensure proper mixing and degassing. Each injection was 3 μL. The heat of dilution of NAG3 was measured in different experiments, injecting the NAG3 solution into the calorimetry vessel containing the buffer. The recorded heat peaks were processed using the MicroCal PEAQ-ITC software supplied with the instrument. The obtained data were fitted with an equivalent and independent binding sites model included in the software provided by the manufacturer, which provided the binding constant (K_b in M^{-1}), the standard binding enthalpy ($\Delta_b H°$ in kJ mol^{-1}), and stoichiometry (N, which is the molar ratio parameter). The experiments were designed to have a molar ratio of two at the end of the titration.

3.2.4 Differential Scanning Calorimetry

Differential scanning calorimetry (DSC) measurements were performed on a high sensitivity Nano DSC from TA Instruments (New Castle, DE, USA) equipped with 300 μL twin gold capillary cells, pressurized to 3 atm. Every sample was scanned from 25 to 90 °C, using a scanning rate of 1 °C/min. The concentration of lysozyme in each experiment was 150 μM. The experiments were performed in

neat buffer and in the presence of magnesium perchlorate. The samples were stirred for five minutes under vacuum to ensure proper mixing and degassing. For each thermogram a background blank was recorded and subtracted. The recorded calorimetric peak was analysed using NanoAnalyze software, provided by the manufacturer.

3.2.5 Circular Dichroism

Circular dichroism (CD) measurements were performed on a Jasco J-715 spectropolarimeter (Jasco Corporation, Tokyo, Japan). Each sample was prepared using a final concentration of Lyz of 200 μM in the presence and absence of 0.5 M of the salt of interest. Spectra of the Lyz-NAG3 complex were recorded in buffer and in the presence of magnesium perchlorate. The concentration of NAG3 was 2 mM. The spectra were recorded at 25 °C in the 320-260 nm range with 0.5 nm resolution, 20 nm/min scanning speed, 2 nm bandwidth, and 4 s of integration time in a 0.1 mm quartz cuvette. The spectra were averaged over four accumulations. For each sample a background blank was recorded and subtracted.

3.2.6 Fluorescence spectroscopy

Fluorescence spectroscopy measurements were performed using a Jasco FP-8650 spectrofluorometer. A solution containing 50 μM lysozyme (Lyz) and 5 μM ANS was titrated with a $Mg(ClO_4)_2$ solution in the 0-20 mM range. All measurements were performed in 0.1 M sodium acetate buffer at pH 5.0 and maintained at a temperature of 25 °C. The excitation wavelength of ANS was set to 350 nm, and emission spectra were recorded in the 400–650 nm range. The excitation and

emission slit widths were set to 5 nm and 10 nm, respectively. Both excitation and emission polarizers were fixed at 0° to prevent Wood's spectral anomaly[197].

3.2.7 Fluorescence anisotropy

The molecular volume of a protein can be estimated using the Perrin equation[198], which describes the relationship between the steady-state anisotropy (r) of a fluorophore and its rotational dynamics:

$$r = \frac{r0}{1+(\tau/\Phi)} \text{ where } \Phi = \frac{\eta V}{RT}$$

In this equation, r_0 represents the anisotropy in the absence of free rotational motion, τ is the average excited-state lifetime, η is the solution viscosity, V is the molecular volume (including the hydration shell), R is the gas constant, and T is the absolute temperature. Steady-state anisotropy reflects the extent of rotational motion of a fluorophore during its excited-state lifetime and is therefore sensitive to both the viscosity of the medium and the size of the rotating molecule. By combining the measured anisotropy values at different viscosities with the known excited-state lifetime and the corresponding viscosities, the molecular volume can be calculated. To this end, a linearized form of the Perrin equation can be used[198]:

$$\frac{1}{r} = \frac{1}{r_0} + \frac{\tau RT}{r_0 \eta V}$$

In this study, four solutions with progressively increasing sucrose concentrations were prepared to systematically vary the solution viscosity, both in the presence and absence of perchlorate. The anisotropy of each sample was measured, and the reciprocal of the measured anisotropy values was plotted against the reciprocal of

the corresponding viscosities. A linear fit was then applied to the data, where the intercept of the fit corresponds to $r_0 = \frac{1}{Intercept}$ and the slope can be used to calculate the molecular volume according to: $V = \frac{\tau RT}{r_0 * (Slope)}$. For this experiment, lysozyme concentration was 3 µM. Fluorescence anisotropy measurements were performed with an excitation wavelength of 280 nm and an emission wavelength of 340 nm. Both the excitation and emission slits were set to 5 nm. <τ> was determined with a Horiba DeltaFlex. In this experiment, excitation was provided by a diode at 295 nm, while the emission wavelength was set to 340 nm. The lysozyme concentration was 3 µM, and both the excitation and emission slits were set to 32 nm. The average excited-state lifetime <τ> was 2.27 ns in buffer and 2.34 ns in the presence of $Mg(ClO_4)_2$.

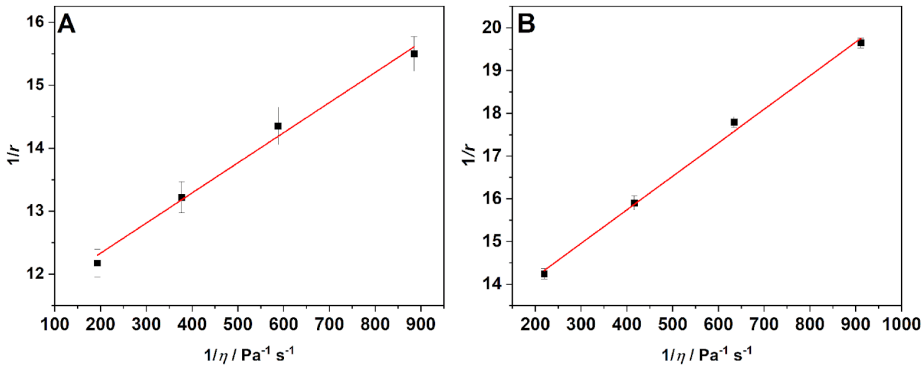

Figure 3.1 Linear fit of the reciprocal anisotropy against the reciprocal viscosity for (A) lysozyme in buffer and (B) lysozyme in the presence of perchlorate.

3.3 Results and Discussion

3.3.1 Impact of Martian relevant salts on NAG3/Lyz binding

To investigate the impact of $MgCl_2$, $MgSO_4$, $Mg(ClO_4)_2$, and, for reference, NaCl on the complex formation between lysozyme (Lyz) and NAG_3, isothermal titration calorimetry (ITC) was employed. This technique provides a complete thermodynamic characterization of the interaction, yielding the changes in binding enthalpy ($\Delta_bH°$), entropy ($T\Delta_bS°$), and free energy ($\Delta_bG°$), while also elucidating how the examined salts influence the binding process. In these experiments, a 250 µM Lyz solution was placed in the calorimeter cell and titrated with a 2.5 mM NAG_3 solution. Measurements were conducted in 0.1 M sodium acetate (NaAc) buffer at pH 5.0, both in the absence and in the presence of 0.5 M NaCl, $MgCl_2$, $MgSO_4$, or $Mg(ClO_4)_2$, over the temperature range 10–40 °C. Fig. 3.2 displays representative ITC thermograms and the corresponding binding isotherms for titrations performed in neat buffer and in the presence of $Mg(ClO_4)_2$ at 20 °C. The complete thermodynamic parameters derived from ITC measurements are summarized in Table 3.1. In all cases, the fitted stoichiometry (N) was close to unity, consistent with the expected 1:1 binding model.

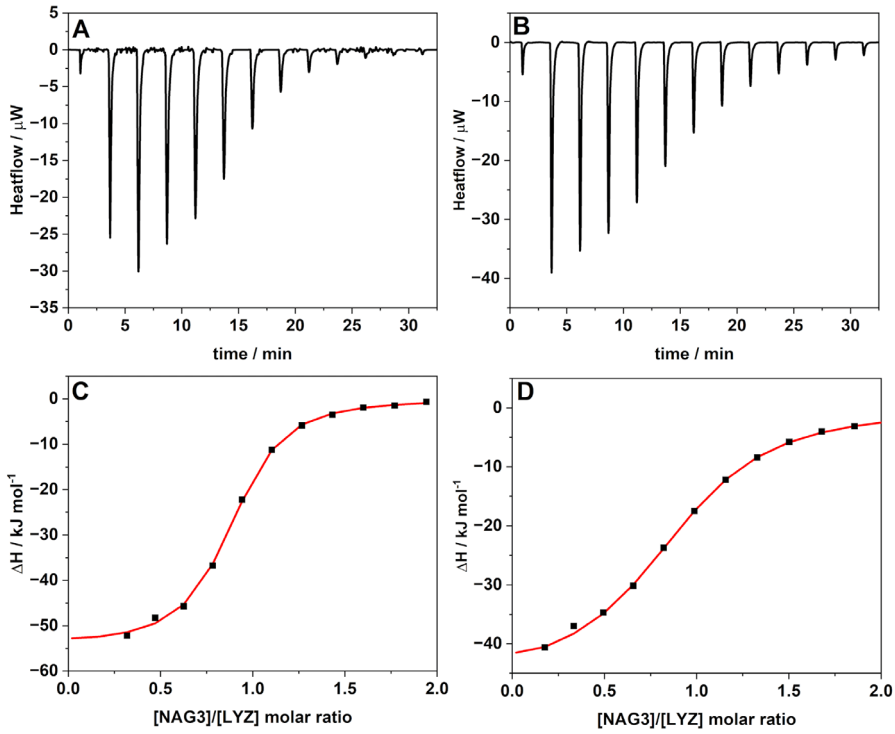

Figure 3.2 (A) ITC trace obtained from the titration of NAG3 with lysozyme in buffer and (B) in the presence of 0.5 M $Mg(ClO_4)_2$. (C) Binding isotherm obtained after data analysis of the ITC trace in buffer and (D) in the presence of $Mg(ClO_4)_2$ at 20°C. The red line represents the best fit of experimental data according to equivalent and independent binding sites model. All the experiments were performed in 0.1 M sodium acetate buffer, pH 5.0.

Table 3.1 The thermodynamic parameters for the complex formation between NAG3 and lysozyme obtained using ITC in buffer and in the presence of various salts at different temperatures.

Solution	T °C	$K_b \cdot 10^5$ M^{-1}	$\Delta_b H°$ kJ mol^{-1}	$T\Delta_b S°$ kJ mol^{-1}	$\Delta_b G°$ kJ mol^{-1}	$\Delta Cp°$ kJ K^{-1}mol^{-1}
Buffer	10	2.4±0.2	-50.9±1.6	-21.8±0.2	-29.1±0.5	-0.43±0.05
	20	1.8±0.2	-54.2±1.8	-24.7±0.3	-29.5±0.5	
	30	0.82±0.05	-58.1±1.4	-29.6±0.2	-28.5±0.5	
	40	0.44±0.02	-64.4±2	-36.6±0.5	-27.8±0.5	
+$Mg(ClO_4)_2$	10	0.32±0.02	-35.8±1.8	-11.4±0.1	-24.4±0.6	-0.58±0.05
	20	0.30±0.05	-46.0±2.1	-20.8±0.3	-25.2±0.4	
	30	0.25±0.02	-49.2±1.4	-23.7±0.2	-25.5±0.5	
	40	0.13±0.01	-52.8±1.9	-28.0±0.1	-24.8±0.5	
+$MgSO_4$	10	2.4±0.2	-48.0±1.7	-18.8±0.5	-29.2±0.2	-0.43±0.03
	20	1.5±0.2	-52.2±1.9	-23.1±0.2	-29.1±0.4	
	30	0.82±0.04	-56.0±1.3	-27.5±0.4	-28.5±0.5	
	40	0.45±0.02	-61.4±2.4	-33.4±0.3	-28.0±0.3	
+$MgCl_2$	10	1.6±0.1	-46.1±1.8	-17.8±0.2	-28.3±0.2	-0.42±0.01
	20	1.1±0.1	-50.7±2.1	-22.6±0.3	-28.2±0.3	
	30	0.60±0.02	-54.3±1.5	-26.5±0.1	-27.8±0.5	
	40	0.33±0.01	-59.0±2.5	-31.9±0.5	-27.1±0.6	
+NaCl	10	2.6±0.2	-49.2±2.1	-19.8±0.4	-29.4±0.3	-0.43±0.03
	20	1.5±0.2	-52.0±2.4	-22.8±0.3	-29.2±0.4	
	30	0.83±0.05	-57.7±2.3	-29.1±0.5	-28.6±0.5	
	40	0.43±0.03	-61.8±2.5	-34.0±0.2	-27.8±0.2	

An inspection of Table 3.1 reveals that, at 20 °C and under neat buffer conditions (pH 5.0), the complex formation between Lyz and NAG3 is characterized by a binding constant of 1.8×10^5 M^{-1}. According to the classification proposed by Velázquez-Campoy and Freire[199], this value falls within the range of moderate affinity, suitable for reliable thermodynamic characterization via isothermal titration calorimetry. In addition, the complex formation is predominantly enthalpy-driven, with a binding enthalpy change of ($\Delta_b H°$) of -54.2 kJ mol^{-1} and an entropy contribution ($T\Delta_b S°$) of -24.7 kJ mol^{-1} at 20°C. These thermodynamic parameters are in excellent agreement with previously reported values at pH 5.0

and 7.0, both measured at 25 °C[173,179]. Specifically, Wei et al. reported $\Delta_b H°$ = -50.3 kJ mol^{-1} and $T\Delta_b S°$ = -21.1 kJ mol^{-1} at pH= 5.0, while Oliva et al. found a value of $\Delta_b H°$ = -52.0 kJ mol^{-1} and $T\Delta_b S°$ = -22.9 kJ mol^{-1} at pH 7.0. The close alignment of these values across different pH conditions highlights the reliability and central role of enthalpy in driving complex formation. The negative $\Delta_b H°$ can be attributed to the formation of non-covalent interactions such as H-bonds and π-stacking interactions. Indeed, as inferred from the crystal structure of the complex[174], NAG3 is located in the binding pocket of Lyz, occupying its subsites (Fig.3.3).

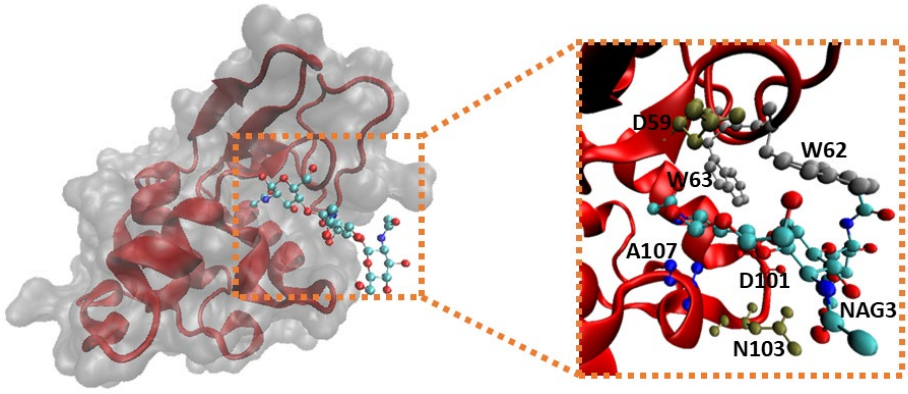

Figure 3.3 The crystal structure of the complex between Lyz and NAG3 (pdb code: 1HEW)[174]. The protein structure is represented as a red ribbon, highlighting the presence of secondary structure elements. The ligand (NAG3) is represented as balls and sticks (N atoms in blue, O in red, and C in cyan). On the left side of the Fig, it is reported an enlargement of the binding pocket of Lyz showing the residues capable to directly interact with the ligand. The Fig was made by using the software Visual Molecular Dynamics (VMD) [200].

Hydrogen bonds are established with residues Asp59, Trp62, Trp63, Asp101, Asn103, and Ala107, while stacking interactions occur with the two tryptophan residues, Trp62 and Trp63. The negative value of $T\Delta_bS°$ indicates an unfavorable entropy contribution accompanying complex formation. Previous studies have shown that approximately 79 water molecules are released from the hydration shells of Lyz and NAG3, including water molecules located near the binding site[201]. Such a release would generally lead to a positive entropy change; however, this effect was not observed. The negative entropy change can therefore be attributed to a reduction in conformational flexibility of both the protein and the ligand upon complex formation. The influence of the investigated salts on complex formation was examined at 20 °C. As reported in Table 3.1, $Mg(ClO_4)_2$ was the only salt found to significantly perturb the Lyz/NAG3 interaction, whereas $MgSO_4$, $MgCl_2$, and NaCl exhibited negligible effects. Although Mg^{2+} ions are capable of interacting with positively charged surface residues of Lyz, thereby potentially influencing its behaviour[202], the data clearly indicate that the perchlorate anion plays the predominant role in modulating the interaction. In the presence of $Mg(ClO_4)_2$, the binding constant (K_b) for Lyz/NAG3 complex formation is approximately one order of magnitude lower than that measured in neat buffer or in the presence of the other salts. This reduction in K_b results in a less favorable free energy of binding ($\Delta_bG°$), the highest among all systems studied. The change in $\Delta_bG°$ is primarily associated with variations in both $\Delta_bH°$ and $T\Delta_bS°$. The binding enthalpy ($\Delta_bH°$) is approximately 15% less negative than in neat buffer, while $T\Delta_bS°$ is about 16% less negative. The less exothermic $\Delta_bH°$ value is consistent with direct interactions of perchlorate ions within the protein binding pocket. These interactions must be disrupted during Lyz/NAG3 complex formation, partially offsetting the enthalpic gain associated with hydrogen

bonding and stacking interactions between Lyz and NAG3. This interpretation aligns with the reduced binding constant observed in the presence of $Mg(ClO_4)_2$. Evidence supporting this explanation has been reported previously[203], with direct perchlorate–lysozyme interactions identified experimentally. Similar behaviour has been described for bovine serum albumin (BSA), where perchlorate binding was found to reduce the affinity for the aromatic ligand 8-anilino-1-naphthalenesulfonic acid (ANS)[102]. Other anions characterized by low charge density, such as iodide, have likewise been reported to interact with protein surfaces[204]. To further substantiate these findings, titrations of the ANS–Lyz complex were performed in the presence of increasing perchlorate concentrations. The fluorescence emission of ANS, which intensifies upon binding to hydrophobic regions of proteins, decreased progressively during titration, whereas the fluorescence signal of free ANS in solution is reported to be negligible[205].

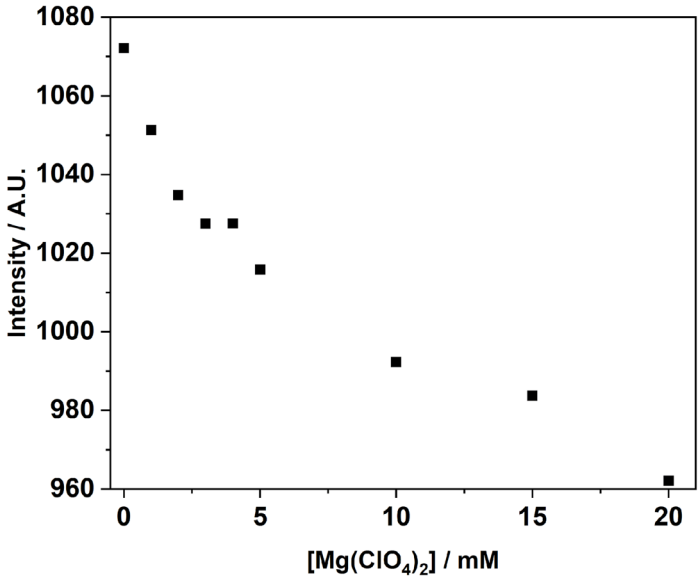

Figure 3.4 Fluorescence displacement assay obtained from the titration of the Lyz/ANS complex with magnesium perchlorate.

Fig 3.4 illustrates the emission intensity of ANS as a function of $Mg(ClO_4)_2$ concentration. As perchlorate binds to the protein, it displaces ANS from its binding site, leading to a reduction in bound ANS and thus a decrease in the fluorescence signal. The less negative $T\Delta_b S°$ can also be explained by the release of perchlorate ions from the Lyz binding pocket upon NAG3 interaction. Indeed, recalling that according to the Hofmeister series of anions, ClO_4^- is chaotropic (*i.e.* water structure-breaker), its release to the bulk will favor a more disordered environment, leading to the increase (in absolute value) of entropy change. Upon release into the bulk solvent, ClO_4^- promotes a more disordered aqueous environment, thereby increasing the entropy change associated with the binding process. However, this entropic gain (reflected in a more favorable $T\Delta_b S°$ term) is

insufficient to counterbalance the less negative and thermodynamically unfavorable $\Delta_b H°$. As a result, the overall Gibbs energy of binding becomes less favorable, leading to a marked reduction in the binding constant.

3.3.2 Impact of Martian relevant salts on Lyz conformation

To gain further insight into the complex formation in the presence of magnesium perchlorate ($Mg(ClO_4)_2$), the conformational behaviour of lysozyme was examined by circular dichroism (CD) spectroscopy. Measurements were performed in the near-UV region (320–260 nm), which primarily reflects the contributions of the aromatic residues (three Phe, three Tyr, and six Trp) located in asymmetric environments within the folded three-dimensional structure of the protein. Consequently, this spectral region provides information on the tertiary structure of lysozyme[161]. The CD spectra of Lyz in buffer and in the presence of 0.5 M salt are shown in Fig. 3.5.

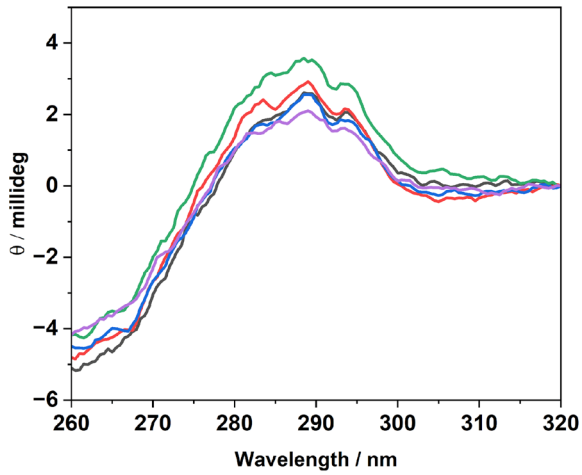

Figure 3.5 CD spectra in the near UV region of lysozyme in the presence of buffer (black line, magnesium perchlorate (red line), magnesium sulphate (blue line), magnesium chloride (green line), sodium chloride (violet line).

The CD spectrum recorded in neat buffer is consistent with those reported under similar conditions [180,206,207]. Upon addition of magnesium perchlorate, minor spectral differences were observed in the 260–295 nm region relative to the buffer spectrum. Comparable trends were obtained in the presence of the other investigated salts, indicating that none of the tested ionic environments induced significant perturbations in the tertiary structure of lysozyme.

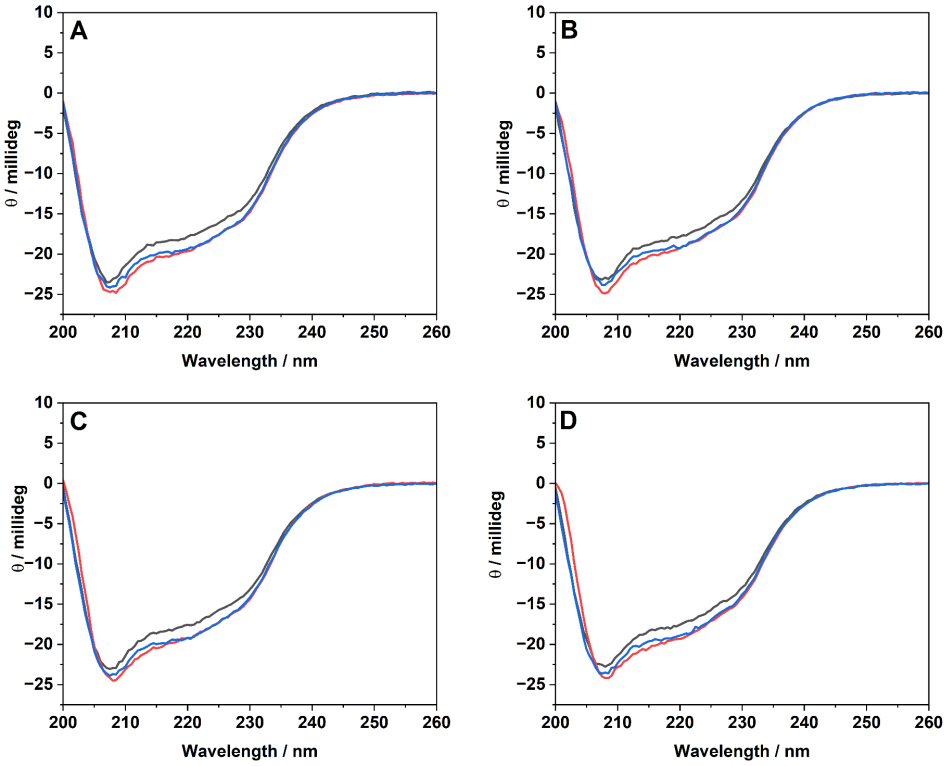

Figure 3.6 CD spectra in the far-UV region of lysozyme in of buffer (black line), in the presence of sodium chloride (red line) and magnesium perchlorate (blue line) at temperature of (A) 10°C, (B) 20°C, (C) 30°C and (D) 40°C.

To gain further insight into this behaviour, CD spectra of lysozyme were also recorded in the far-UV region (260–200 nm, Fig. 3.6). Interestingly, the spectra obtained in the presence of salts exhibited slightly higher intensity compared to those recorded in buffer, consistent with the observations from the near-UV region. Moreover, to assess the potential influence of temperature on the protein structure, spectra were collected over the 10–40 °C range, revealing no significant

differences in spectral intensity. To better interpret these results, the molecular volume of lysozyme was estimated using the Perrin equation (see Materials and Methods), which relates the rotational correlation time to the molecular volume, including the hydration contribution. This approach provides insight into the effective hydrodynamic volume of the protein under different conditions. The analysis revealed a decrease in molecular volume in the presence of magnesium perchlorate ($V_{buffer} = (2.22 \pm 0.05) \times 10^4$ Å^3 molecule^{-1}; $V_{ClO_4} = (1.55 \pm 0.03) \times 10^4$ Å^3 molecule^{-1}; Fig. 3.1). Taken together, the CD and fluorescence data indicate that the presence of magnesium perchlorate alters the hydration shell of lysozyme rather than its conformation. This interpretation is consistent with previous reports showing that chaotropic salts such as perchlorates can modulate protein hydration without significantly perturbing the secondary or tertiary structure[208].

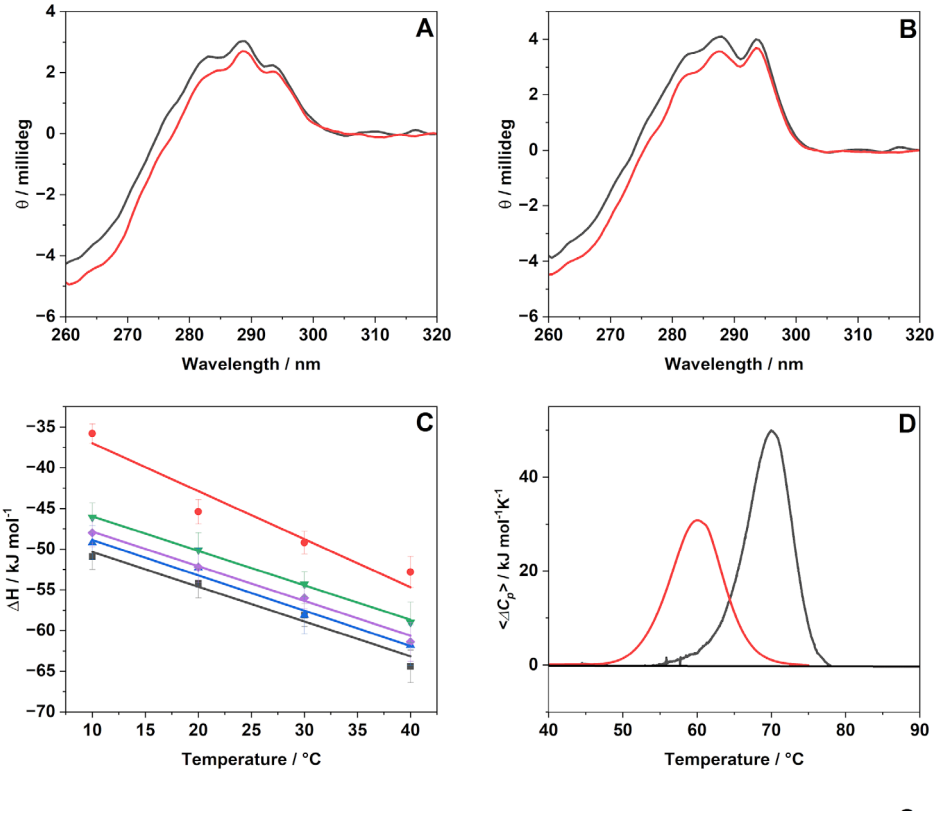

Figure 3.7 (A) Near-UV CD spectra of lysozyme in buffer (black line) and in the presence of $Mg(ClO_4)_2$ (red line). (B) Near-UV CD spectra of the complex lysozime-NAG3 in buffer (black line) and in the presence of $Mg(ClO_4)_2$ (red line). (C) Binding heat capacity variation ($\Delta C_p°$) of the following systems: buffer (black line), $Mg(ClO_4)_2$ (red line), NaCl (blue line), $MgCl_2$ (green line), $MgSO_4$ (violet line). (D) DSC traces of lysozyme in buffer (black line) and in the presence of $Mg(ClO_4)_2$ (red line).

Table 3.2. Thermodynamic parameters of lysozyme thermal unfolding determined by DSC measurements

System	T_m °C	$\Delta_m H°$ kJ mol^{-1}	$\Delta_m S°$ kJ K^{-1} mol^{-1}
Buffer	70.0±0.2	400±20	1.16±0.15
+ $Mg(ClO_4)_2$	60.0±1.0	290±20	0.86±0.09

Next, the CD spectra of Lyz in complex with NAG3 (Fig 3.7B) were collected as well, both in neat buffer conditions and in the presence of $Mg(ClO_4)_2$. In neat buffer, upon NAG3 binding, the intensity of the CD spectrum of the protein increased, suggesting a reduction in structural fluctuations. In addition, a clear change in the shape of the positive band (275 nm – 300 nm) was observed. This can be explained by considering that in the active site of Lyz, two Trp residues are present (Fig 3.3). The binding of NAG3 changes the asymmetry of the environment surrounding the aromatic residues, leading to the observed changes in the spectrum. Remarkably, a very similar behaviour was observed in the presence of $Mg(ClO_4)_2$. Thus, based on the above considerations, it is possible to conclude that the alteration in the binding constant observed in the presence of $Mg(ClO_4)_2$ cannot be attributed to conformational changes imposed by the perchlorate anion.

3.3.3 Impact of temperature and salts on Lyz-NAG3 interaction

Next, the impact of the temperature on the Lyz/NAG3 complex formation was measured by performing additional ITC experiments at 10 °C, 30 °C and 40 °C. All the thermodynamic data are collected in Table 3.1. Under neat buffer conditions, the binding constant (K_b) decreases with increasing temperature, from 2.4×10^5 M^{-1} at 10 °C to 0.44×10^5 M^{-1} at 40 °C. A similar temperature dependence was observed in the presence of NaCl, $MgCl_2$, and $MgSO_4$. Notably, in the presence of $Mg(ClO_4)_2$, only minor variations in K_b were detected across the explored temperature range, indicating that the binding process is largely insensitive to temperature under these conditions. As reported in Table 3.1, the binding enthalpy ($\Delta_bH°$) varies with temperature in all tested environments, allowing the estimation of the change in binding heat capacity ($\Delta C_p°$) according to the relation $\Delta C_p° = (\delta\Delta_bH°/\delta T)_p$, which represents the difference in heat capacity between the complexed (Lyz/NAG3) and uncomplexed (Lyz + NAG3) states (Fig. 3.7C). The ΔCp° values, listed in the last column of Table 3.1, are negative under all conditions, being approximately −0.44 kJ K^{-1} mol^{-1} in neat buffer and in the presence of NaCl, $MgCl_2$, and $MgSO_4$, and −0.58 kJ K^{-1} mol^{-1} in the presence of $Mg(ClO_4)_2$.

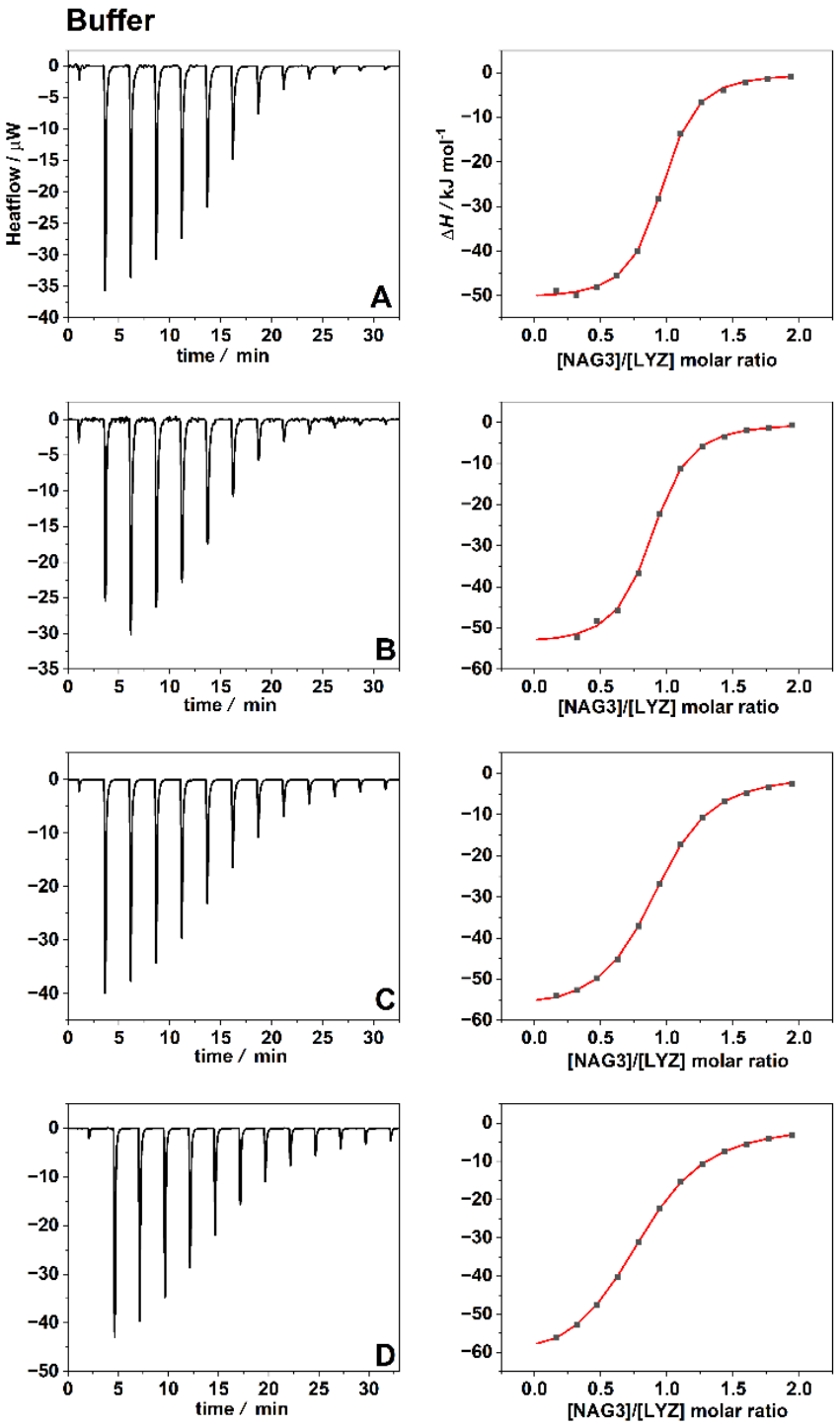
Buffer
Heatflow / μW
time / min
A
ΔH / kJ mol-1
[NAG3]/[LYZ] molar ratio
B
C
D

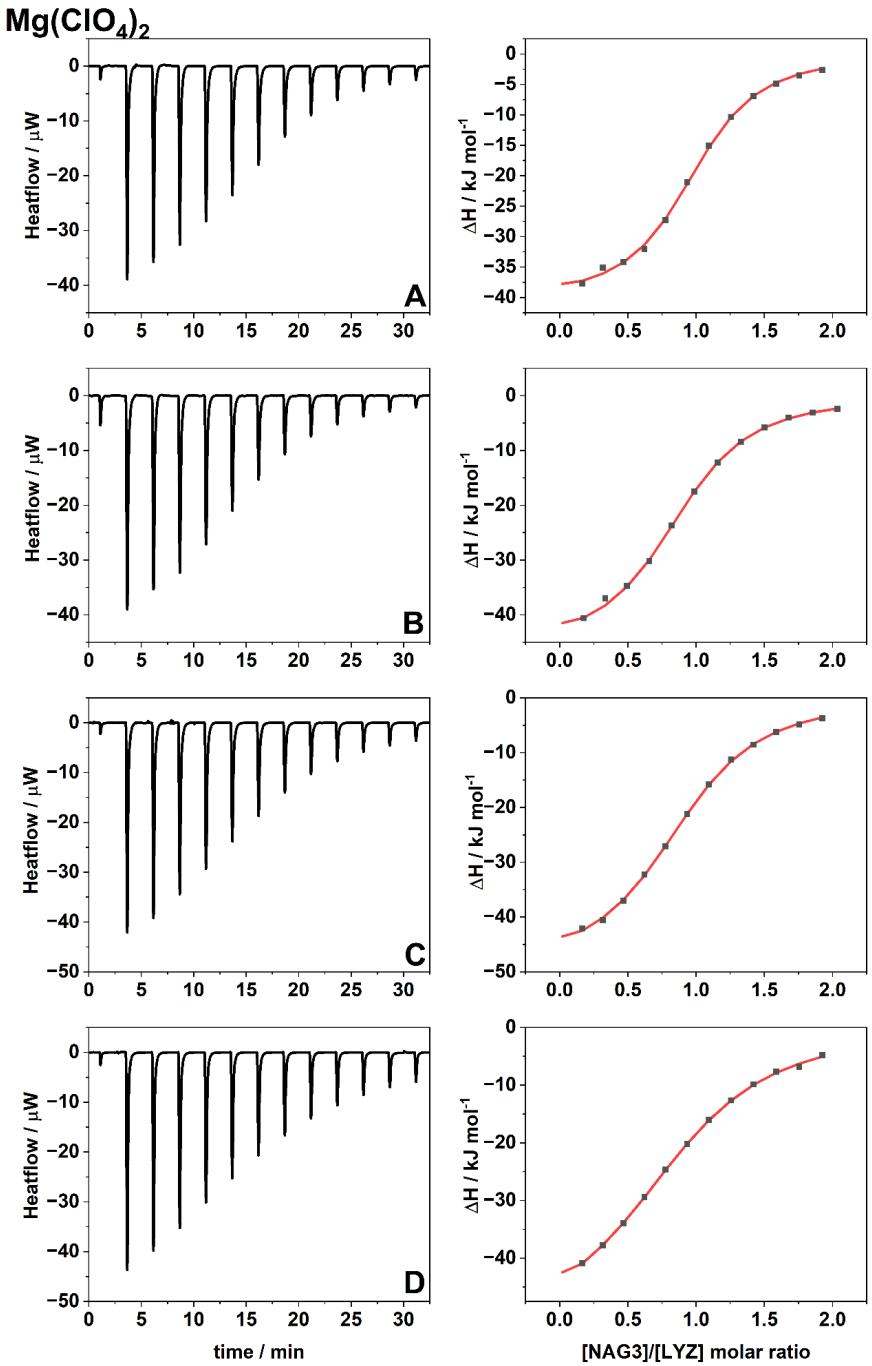
Mg(ClO4)2
Heatflow / μW
ΔH / kJ mol-1
A
B
C
D
time / min
[NAG3]/[LYZ] molar ratio

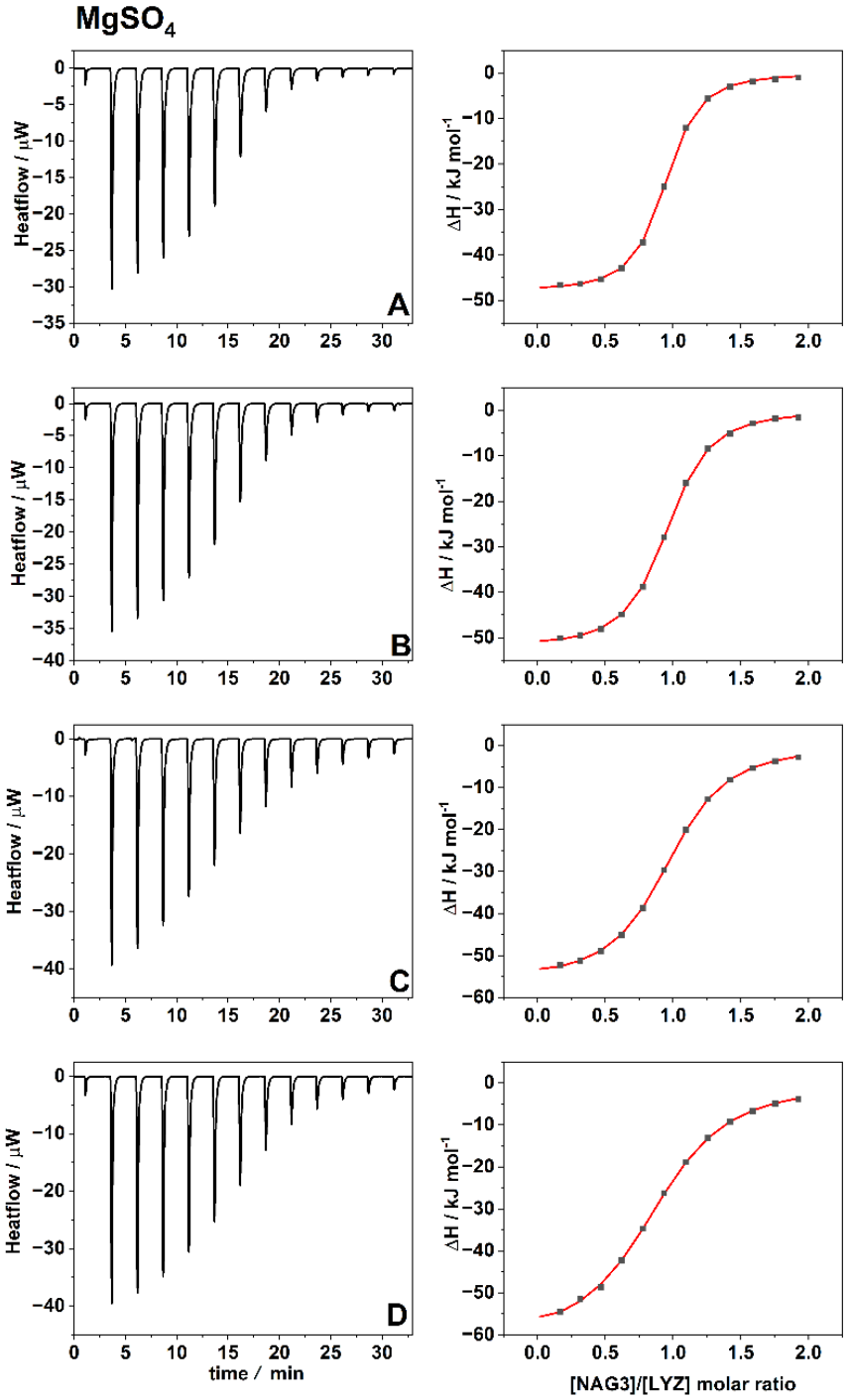
MgSO4
Heatflow / μW
ΔH / kJ mol-1
A
B
C
D
time / min
[NAG3]/[LYZ] molar ratio

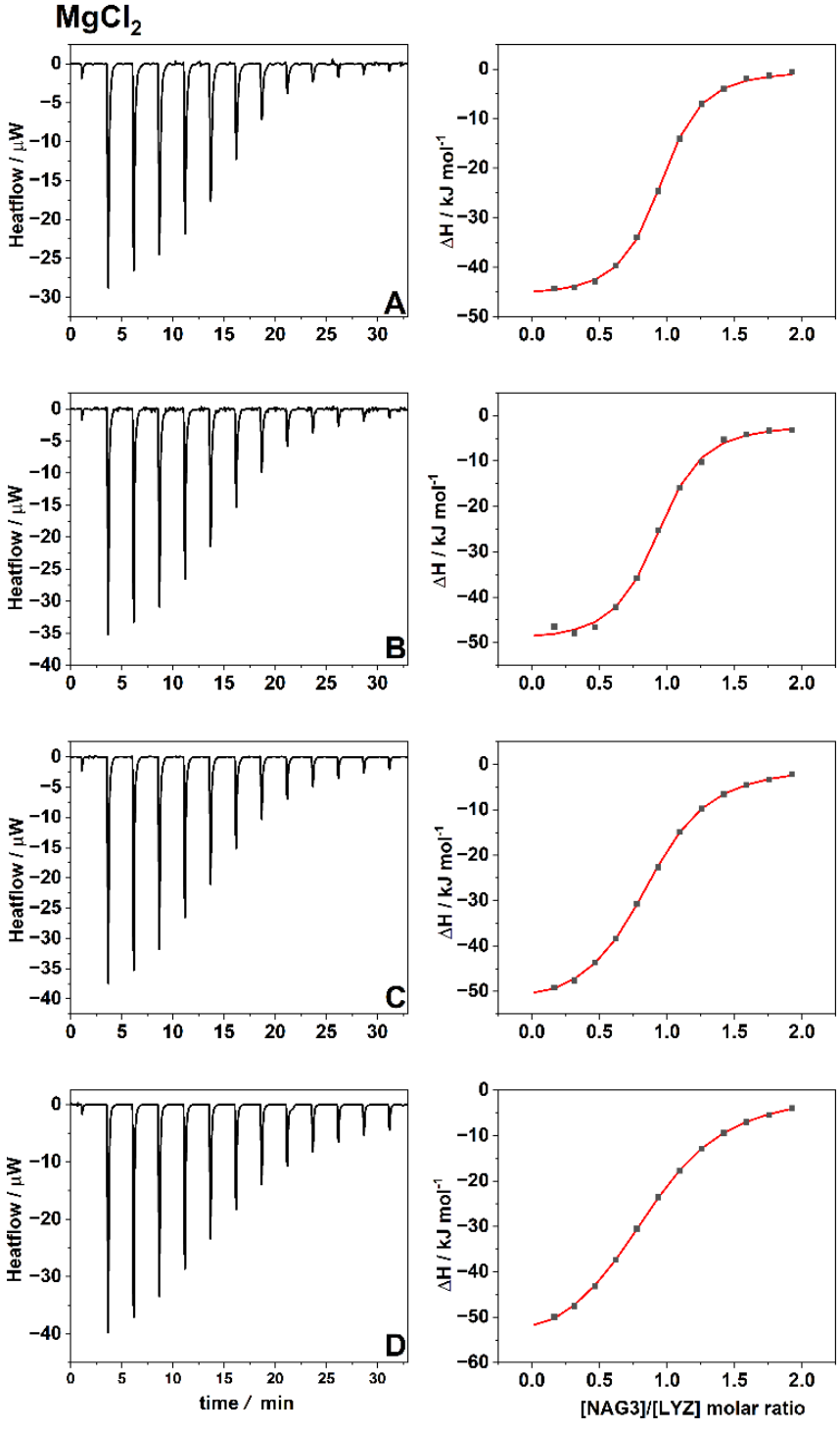
MgCl2
Heatflow / μW
ΔH / kJ mol-1
A
B
C
D
time / min
[NAG3]/[LYZ] molar ratio

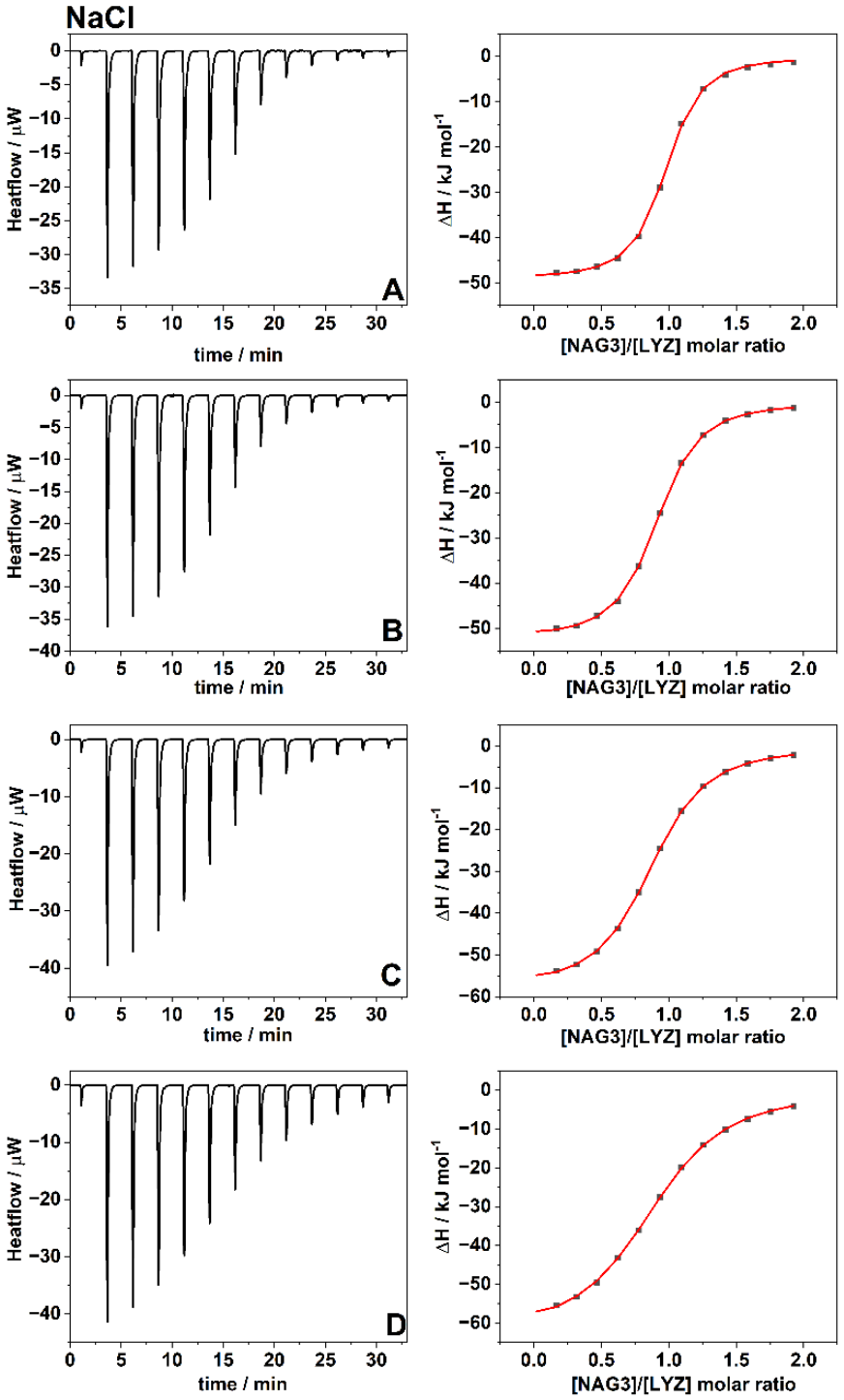
NaCl
Heatflow / μW
time / min
ΔH / kJ mol-1
[NAG3]/[LYZ] molar ratio
A
B
C
D

Figure 3.8. The ITC traces obtained from the titration of NAG3 with lysozyme (left), along with the corresponding binding isotherm derived from data analysis (right). Measurements are reported for buffer, and in the presence of $Mg(ClO_4)_2$, $MgSO_4$, $MgCl_2$ and NaCl, respectively. Each panel displays measurements performed at four different temperatures: 10°C (A), 20°C (B), 30°C (C) and 40°C (D).

Negative $\Delta C_p°$ values are typically attributed to the burial of hydrophobic residues at the protein–ligand interface[209,210], and this effect likely accounts for the observed trends. However, the more negative $\Delta C_p°$ value in $Mg(ClO_4)_2$ suggests an additional contribution beyond hydrophobic burial. Fluorescence anisotropy measurements revealed that the molecular volume of lysozyme decreases by approximately 30% in the presence of magnesium perchlorate. Since these molecular volumes include both the protein and its hydration shell[198], and CD experiments indicated only minor conformational changes upon perchlorate binding, the enhanced negative $\Delta C_p°$ can be attributed to a larger change in hydration upon complex formation, with the nonpolar surface becoming less hydrated. To further test this interpretation, differential scanning calorimetry (DSC) experiments were performed on lysozyme in neat buffer and in the presence of $Mg(ClO_4)_2$. The DSC thermograms (Fig. 3.7D) and the derived thermodynamic parameters (denaturation temperature, enthalpy, and entropy changes; Table 3.2) show that in the presence of magnesium perchlorate the denaturation temperature decreases by approximately 10 °C relative to the buffer value. Moreover, the denaturation process in $Mg(ClO_4)_2$ was found to be highly reversible (≈92%), as determined from the enthalpic changes observed in two consecutive DSC scans (Fig. 3.9).

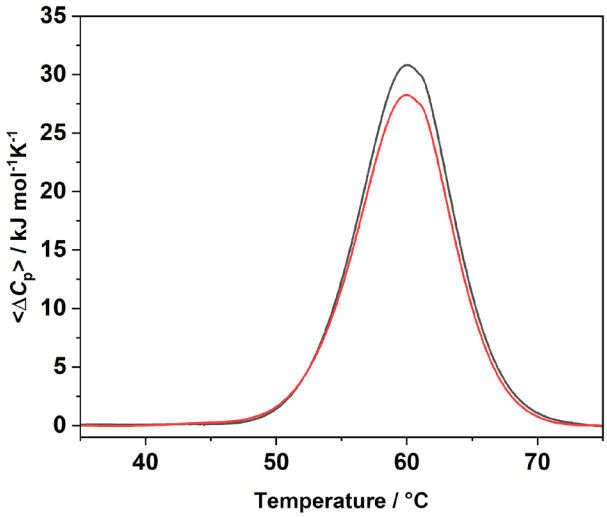

Figure 3.9. First (black line) and second (red line) heating curves of lysozyme in the presence of magnesium perchlorate.

Additionally, the enthalpy change of denaturation in $Mg(ClO_4)_2$ solution was about 28% lower than the enthalpy measured in neat buffer and the temperature decreased of about 10°C, in agreement with previously reported data[203]. Instead, the entropy change of denaturation in perchlorate solution is around 26% lower compared to the value determined in neat buffer. The detected lower entropy change of denaturation can be ascribed to the reduced hydration of the protein surface in the presence of perchlorate, where the unfolding process is accompanied by a reduced release of water molecules, supporting the findings described above.

Finally, the DSC data align with the ITC measurements, which indicate that the binding of NAG3 to lysozyme in the presence of magnesium perchlorate results in a reduced binding constant. This reduction is attributed to changes in the protein

hydration and solvation properties, as previously discussed, leading to a decrease in both the unfolding enthalpy and temperature.

3.4 Conclusions

This study demonstrates that salt-rich environments, particularly those containing magnesium perchlorate ($Mg(ClO_4)_2$), significantly modulate the thermodynamics of protein–ligand interactions without inducing major conformational changes in the protein structure. Using lysozyme and NAG3 as a model system, it has been shown that $Mg(ClO_4)_2$ reduces the binding affinity by an order of magnitude, primarily through alterations in hydration and solvation properties. Circular dichroism and fluorescence anisotropy data indicate that these effects are due to changes in the hydration shell and protein microenvironment. Differential scanning calorimetry further supports this interpretation, revealing a decrease in both denaturation temperature and enthalpy in the presence of perchlorate. These findings suggest that chaotropic salts like $Mg(ClO_4)_2$ can influence protein function in extraterrestrial-like conditions by modulating water structure and protein–ligand interactions, offering valuable insights into biochemical resilience in salts-rich environments such as those found on Mars or Europa.

Chapter 4: Exploring the interaction of G-Quadruplexes with different model membranes

4.1 Introduction

The emergence of life is thought to have required a close interplay between nucleic acids and primitive membranes[106]. Compartmentalization provided by lipid bilayers was essential for creating distinct microenvironments[105,107,108,211], while nucleic acids offered the ability to store information and catalyse chemical transformations. According to the widely discussed RNA world hypothesis[110], RNA molecules played a central role at this stage, acting both as carriers of genetic information and as ribozymes with catalytic activity[111,212,213]. However, RNA molecules are also chemically versatile and can adopt a variety of secondary and tertiary structures beyond the simple duplex or single strand [214–219]. Among these, G-quadruplexes (G4s) stand out as highly stable, compact helical structures formed by guanine-rich sequences[220–222]. These structures are stabilized through Hoogsteen-type hydrogen bonding and the presence of specific monovalent cations such as K^+ or Na^+[223,224]. The idea of a quadruplex world hypothesis has recently been proposed[118], suggesting that G4 structures might have been among the earliest functional nucleic acid folds to emerge. Their enhanced chemical and structural stability, together with the ability to participate in complex interactions, make them attractive candidates for molecules that could have played a role in prebiotic chemistry and early evolution. Neverthless, our understanding of the behaviour of non-canonical nucleic acid structures in the context of protocellular

membranes remains very limited[106]. This is particularly relevant, since modern biology provides numerous examples in which nucleic acid–membrane interactions play a crucial role[121,128,129,225–227], including the regulation of processes occurring at membrane–water interfaces. It is therefore reasonable to hypothesize that similar interactions between nucleic acids and primitive lipid bilayers could have influenced the earliest steps toward the organization of life. However, most previous work has focused on canonical nucleic acid forms[130,131,228,229], much less is known about the affinity of G-quadruplexes for lipid bilayers and how this depends on factors such as membrane composition, charge, and physical state[121,230]. To address this gap, a systematic investigation of the binding of a panel of RNA and DNA G4s with model membranes was performed, taking into account the effects of membrane phase state (gel versus fluid) and surface charge (zwitterionic versus negatively charged lipids). For this purpose, liposomes composed of zwitterionic phosphatidylcholines (DPPC and POPC) and negatively charged mixtures containing phosphatidylglycerol or phosphatidylserine (DPPC/DPPG, POPC/POPG, DPPC/POPS, POPC/POPS) were employed. Binding affinities were quantified through fluorescence anisotropy measurements using fluorescently labeled oligonucleotides, comparing the free nucleic acids with those associated to the larger lipid vesicles. The results presented here demonstrate that G4–lipid interactions are strongly dependent on both the structural nature of the G-quadruplex and the physicochemical properties of the membrane. In particular, RNA G4s show a pronounced affinity for negatively charged bilayers, whereas DNA G4s do not. These findings provide new insights into how nucleic acid–lipid interactions could have contributed to the chemical landscape of early life, suggesting that G-

quadruplex structures may have had functional relevance already in prebiotic scenarios.

4.2 Experimental section

4.2.1 Chemicals

The lipids 1,2-dipalmytoil-*sn*-glycero-3-phosphocholine (DPPC), 1,2-dipalmytoil-*sn*-glycero-3-*rac*-phosphoglycerol (DPPG), 1-palmytoil-2-oleyl-*sn*-glycero-3-phosphocholine (POPC), 1-palmytoil-2-oleyl-*sn*-glycero-3-*rac*-phosphoglycerol (POPG) and 1,2-dioleoyl-sn-glycero-3-phosphoethanolamine-N-(lissamine rhodamine B sulfonyl) (ammonium salt) (N-Rh-DHPE) were purchased from Avanti Polar Lipids Inc. (Alabaster, AL, USA) and were used without further purification. Unlabeled and 5'-labeled with carboxyfluorescein (FAM) sequences (see Table 4.1) were purchased as HPLC grade powder from Biomers (Ulm/Donau, Germany) or Genscript (Rijswijk, Netherlands). Lithium cacodylate buffer, lithium chloride, sodium chloride, potassium chloride, calcium chloride, RNAse free water and 1,3-diphenil-1,3,5-hexatriene (DPH) were purchased from Merck (Darmstadt, Germany).

4.2.2 Vesicle preparation

Giant Unilamellar Vesicle (GUVs) were used for confocal fluorescent microscopy, Multilamellar Vesicles (MLVs) were used for Differential Scanning Calorimetry measurements. In all other experiments, Small Unilamellar Vesicles (SUVs) were used. GUVs vesicles were prepared using the electroformation method by means of Vesicle Prep Pro from Nanion Technologies (Munich,

Germany). Briefly, a solution containing a total lipid concentration of 5 mM was prepared and 1% mol/mol of N-Rh-DHPE was added. Subsequently, 20 μL of the solution were placed on an indium tin oxide (ITO) coated coverslip. The solvent was dried under vacuum for 1 hour. An O-ring was placed around the lipid film and 300 μL of a solution containing K^+-buffer and 300 mM of sucrose were added to the lipid film. GUVs were grown for 3 hours in a 3 V voltage 100 Hz electric field at 65°C. SUVs were prepared weighting appropriate amounts of the desired lipid; the lipid was dissolved in chloroform and subsequently dried out under a stream of nitrogen. The lipid film was hydrated in buffer solution and subsequently sonicated for 90 seconds at 20 kHz at 20% of duty cycle. MLVs were prepared in the same way as SUVs, without sonication.

4.2.3 Sample preparation

Oligonucleotide stock solutions were prepared by dissolving the lyophilized powders in nuclease-free water. Concentrations were determined spectrophotometrically (using a Jasco V730 spectrophotometer from Jasco Corporation, Tokyo, Japan) by measuring the absorbance at 260 nm and calculating using extinction coefficients derived from the nearest-neighbour model[231]. For experiments involving a quadruplex structure, samples were diluted to the desired concentration in 10 mM lithium cacodylate (LiDMA) buffer (pH 7.0) containing 10 mM KCl. For experiments involving the unstructured oligonucleotide, samples were diluted in 10 mM LiDMA buffer (pH 7.0) containing 10 mM LiCl (lithium buffer), heated to 90 °C for 4 minutes, and then allowed to slowly cool to room temperature prior to storage at 4 °C. In all cases, after the annealing process, 2 mM $CaCl_2$ was added. In the main text the buffers

were named: K^+-buffer (10 mM LiDMA pH 7.0, 10 mM KCl, 2mM $CaCl_2$) and Li^+-buffer (10 mM LiDMA pH 7.0, 10 mM LiCl, 2mM $CaCl_2$).

4.2.4 Fluorescence anisotropy

Binding of FAM-labelled oligonucleotides to membranes was fluorescence anisotropy. Fluorescence anisotropy is defined by the equation: $< r > = (I_{VV} - GI_{VH})/(I_{VV} + 2GI_{VH})$, where I_{VV} is the fluorescence intensity obtained by setting both the excitation and emission polarizers vertically, I_{VH} is the fluorescence intensity obtained by setting the excitation polarizer vertically and the emission polarizer horizontally, and G is the grating (or instrument-specific) correction factor used to account for differences in the detector's sensitivity to vertical and horizontal polarized light. Excitation and emission wavelength were 450 nm and 516 nm respectively, while both the excitation and emission slits were set to 9 nm. The desired oligonucleotide was titrated in cell with a suspension of SUVs. The binding isotherm was obtained by plotting the relative anisotropy values ($r/r_{(0)}$) against total lipid concentration, where r and $r_{(0)}$ are the anisotropies of the labelled oligonucleotide in the presence and in the absence of SUVs, respectively. The mole fraction partition constant (K_x) was obtained by fitting the experimental data with the following equation[232]:

$$R = 1 + (R_\infty - 1)\cdot[(K_x\cdot[L])/([W] + K_x\cdot[L])]$$

where R is the relative anisotropy at each point of the titration, R_∞ is the relative anisotropy at saturation, [L] is the lipid concentration, and [W] = 55.3 M is the molar concentration of water. The mole fraction partition constant is defined as[233] $K_x = ([O_b]/[L])/([O_f]/[W])$ where $[O_b]$, $[O_f]$, [L] and [W] are the molar

concentrations of the membrane-associated oligonucleotide, the free oligonucleotide in the aqueous phase, the lipids and water, respectively. Oligonucleotides concentration was 100 nM, while lipid concentration ranged from 0 to 500 μM. All titrations were performed at 20°C on a Jobin Yvon Horiba Fluoromax 4.

Fluorescence anisotropy melting experiments were performed using 1,6-diphenyl-1,3,5-hexatriene (DPH) as a hydrophobic probe embedded in DPPC liposomes at a lipid-to-probe molar ratio of 150:1. DPH intercalates into the hydrophobic core of the lipid bilayer, and its fluorescence anisotropy is highly sensitive to the physical state of the membrane. Higher anisotropy values correspond to a more compact and rigid bilayer, whereas lower anisotropy values indicate increased membrane fluidity. The sharp decrease in anisotropy is associated with the melting of the acyl chains during the gel-to-liquid crystalline phase transition. DPH was excited at 355 nm, and emission was recorded at 425 nm. Measurements were performed over a temperature range of 20–60 °C, with a heating rate of 1 °C/min, and anisotropy values were recorded at 1 °C intervals. The total lipid concentration was 50 μM. Melting experiments were carried out both in the absence and in the presence of the oligonucleotide at a final concentration of 5 μM.

4.2.5 Confocal fluorescence microscopy

Image acquisitions were performed with a confocal laser scanning microscope (LSM700-Zeiss, Germany) equipped with an Ar laser (488 nm), and a He–Ne laser (555 nm). The images were obtained using a "plan-apochromat" 63x/1,40 oil DIC m27 objective. All images were analysed with ZEN Black Imaging Software

3.0 (ZEISS, Jena, Germany). Acquisition parameters were identical for each sample. Total lipid concentration was 300 μM, while oligonucleotide concentration was 1 μM

4.2.6 Circular dichroism

CD measurements were performed on a Jasco J-1500 spectropolarimeter (Jasco Corporation, Tokyo, Japan). The spectra were recorded at 20°C in a 1.0 cm quartz cuvette in the 330-220 nm spectral range with a 0.5 nm resolution, 50 nm/min scanning speed, 4 nm bandwidth and 4s integration time. The spectra were averaged over two accumulations. Total oligomer concentration was 3 μM. In the experiments with the lipid bilayers, the total lipid concentration was 300 μM. For each sample a background blank was subtracted. CD melting experiments were performed with a 1°C/min heating rate monitoring the intensity at 263 nm for G4-RNA and cMyc in K^+-buffer, and at 269 nm for G4-RNA in Li^+-buffer. Temperature ranges were 10-100°C for G4-RNA in K^+-buffer , from 20-100°C for cMyc and from 10-90°C for G4-RNA in Li^+-buffer.

4.2.7 Differential scanning calorimetry (DSC)

Heat capacity curves of a 1 mM MLVs suspension were recorded in K^+-buffer and in the presence of 100 μM oligonucleotide (Lipid/Quadruplex ratio = 10) using a high sensitivity Nano DSC (TA Instruments, New Castle, DE, USA) equipped with 300 μL twin gold capillary cells, pressurized to 3 atm. Every sample was scanned from 20 to 55 °C at least three times, using a scanning rate of 1 °C/min. For each thermogram, a background blank thermogram was subtracted. Data were analyzed using the Nano Analyze software, provided by the manufacturer.

Enthalpy values were obtained by direct integration of the normalized baseline subtracted peaks and normalized per total lipid moles.

4.2.8 Isothermal titration calorimetry (ITC)

Isothermal titration calorimetry (ITC) measurements were performed on a Malvern Microcal PEAQ-ITC instrument equipped with a 200 µL gold cell and 40 µL syringe. All experiments have been performed titrating a 5 mM lipid suspension with a 50 µM oligonucleotide solution. Each injection was 7.5 µL. The heat of dilution of oligonucleotides was measured in different experiments, injecting the oligonucleotide solution into the calorimetry vessel containing only the buffer. The titrations were performed using a large excess of lipids to ensure that all injected quadruplex was bound to the lipids. The recorded heat peaks were processed using the MicroCal PEAQ-ITC software supplied with the instrument. The standard Gibbs free energies of partition were determined from K_x according to $\Delta G_x^\circ = -RT\ln(K_x)$ and the standard entropies of partition from the Gibbs relation.

4.2.9 Fluorescence spectroscopy

Fluorescence spectroscopy measurements were performed on a Jobin Yvon Horiba Fluoromax-4. Laurdan was incorporated into lipid vesicles at a probe-to-lipid ratio of 1:30. Changes in lipid order and hydration, and thus in the membrane phase state, were monitored using the generalized polarization (GP) parameter, defined as $GP = (I_{440} - I_{480})/(I_{440} + I_{480})$, where I_{440} and I_{480} correspond to the emission intensities at 440 nm and 480 nm, respectively Low GP values indicate a more hydrated, fluid state of the membrane, whereas high GP values (approximately 0.5) correspond to a less hydrated, ordered gel phase [147,151].

Laurdan emission spectra were recorded between 360–640 nm with excitation at 340 nm, using 8 nm slits for both excitation and emission. The total lipid concentration was 50 μM, and the oligonucleotide concentration was 5 μM. GP-melting experiments were performed in the temperature range of 20–65 °C with a scan rate of 1°C/min.

4.3 Results and discussion

4.3.1 Characterization of quadruplex-membrane interaction

First, the partition constant of an RNA (G4-RNA) and a DNA (cMyc) G4 of parallel topology for the DPPC gel phase zwitterionic membrane was evaluated. The formation of parallel G4 topology under the experimental conditions mentioned in materials and methods was further confirmed for both sequences by inspection of their CD spectra (Fig 4.1), showing the characteristic maxima at 264 nm and minima at 245 [234]. Both oligonucleotides were labelled with carboxyfluorescein (FAM) (Table 4.1)[235], a fluorophore reported not interacting with lipid bilayers[236].

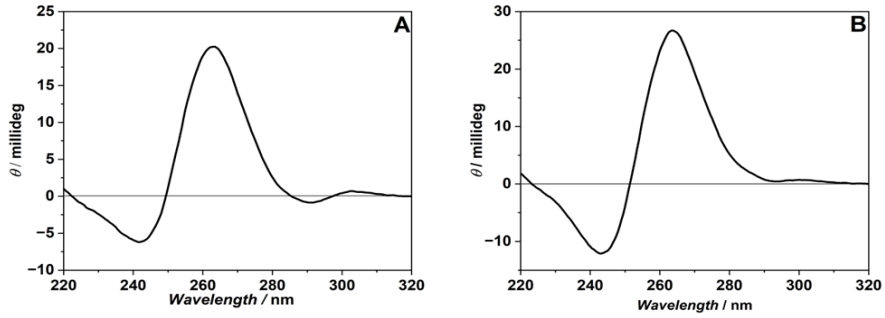

Figure 4.1. CD spectra of G4-RNA (A) and cMyc (B) in potassium buffer

Table 4.1. RNA and DNA sequences employed in this study

Oligonucleotide	Sequence
FAM-G4-RNA	6-FAM-AGGGAAGGGAAGGGAAGGGA
FAM-cMyc	6-FAM-TGAGGGTGGGTAGGGTGGGTAA
FAM-Tel23	6-FAM-TAGGGTTAGGGTTAGGGTTAGGG
FAM-mut-RNA	6-FAM-AGTGAAGGTAATGGAAGTGA
FAM-G3U2	6-FAM-AAAGGGUUGGGUUGGGUUGGGAAA
G4-RNA	AGGGAAGGGAAGGGAAGGGA
cMyc	TGAGGGTGGGTAGGGTGGGTAA

Analysis of the binding curves indicates that both G4 structures interact strongly with the DPPC, though with markedly different partition constants (Figs. 4.2, 4.3, and Table 4.2). In particular, G4-RNA binds to the DPPC bilayer with a partition constant approximately seven times higher than that of the cMyc quadruplex. The affinity of both quadruplexes for the negatively charged DPPC/DPPG membrane was then examined. A partition constant of $(4.9 \pm 0.3) \times 10^5$ was determined for G4-RNA, whereas no measurable binding curve was obtained for cMyc, indicating a negligible interaction of this G4 with the anionic membrane (Fig. 4.2 and Table 4.2).

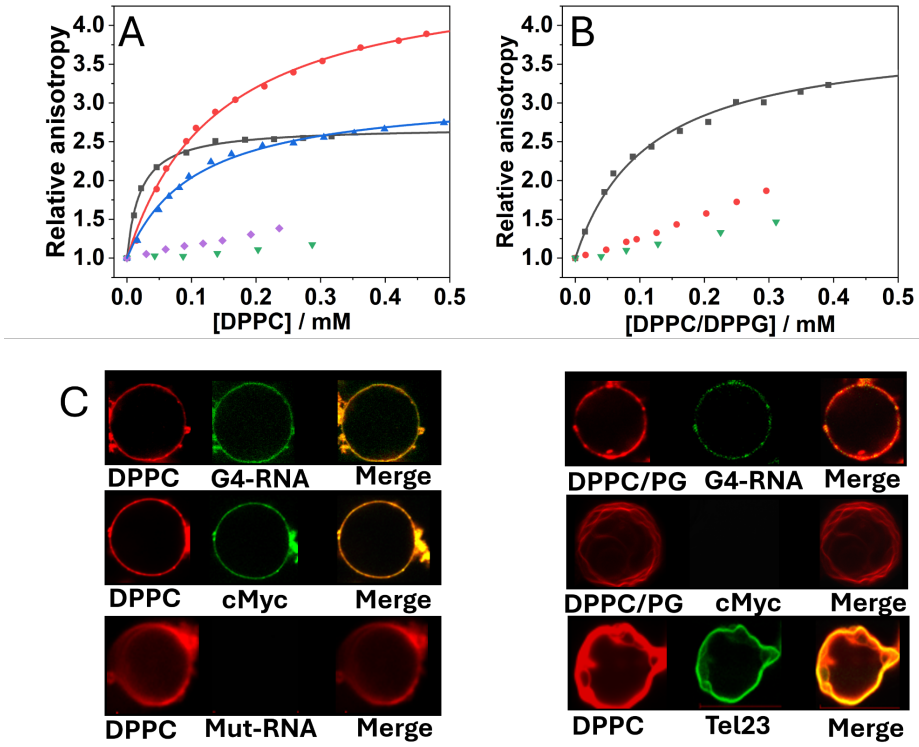

Figure 4.2. Representative binding curves of the studied nucleic acids with (A) DPPC and (B) DPPC/DPPG membranes. G4-RNA (black), cMyc (red), Mut-RNA (violet) in K^+-buffer and G4-RNA (blue) and cMyc (green) in Li^+-buffer. All the binding experiments were performed at 20 °C. (C) Confocal fluorescence microscopy images of GUVs (red) incubated with different oligonucleotides (green). Colocalization appears as yellow in the merged images.

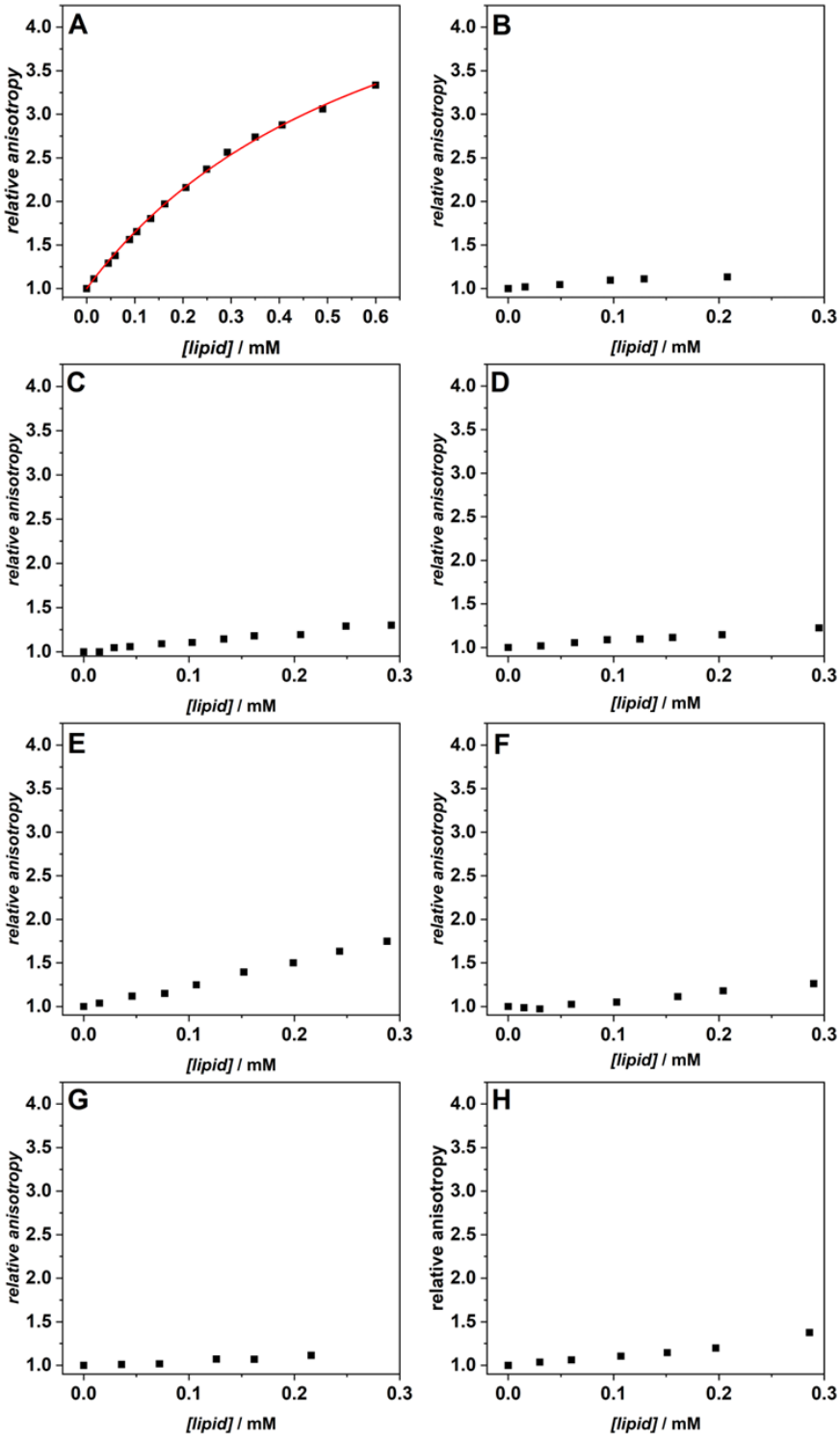
A
B
C
D
E
F
G
H
relative anisotropy
[lipid] / mM
1.0
1.5
2.0
2.5
3.0
3.5
4.0
0.0
0.1
0.2
0.3
0.4
0.5
0.6

Figure 4.3. Experimental data points of (A) G4-RNA vs DPPC/DPPG in lithium buffer, (B) cMyc vs DPPC in potassium buffer, (C) G4-RNA vs POPC in potassium buffer, (D) G4-RNA vs POPC/POPG in potassium buffer, (E) Tel23 vs DPPC in potassium buffer, (F) Tel23 vs DPPC/DPPG in potassium buffer, (G) Tel23 vs DPPC in lithium buffer, (H) Tel23 vs DPPC/DPPG in lithium buffer.

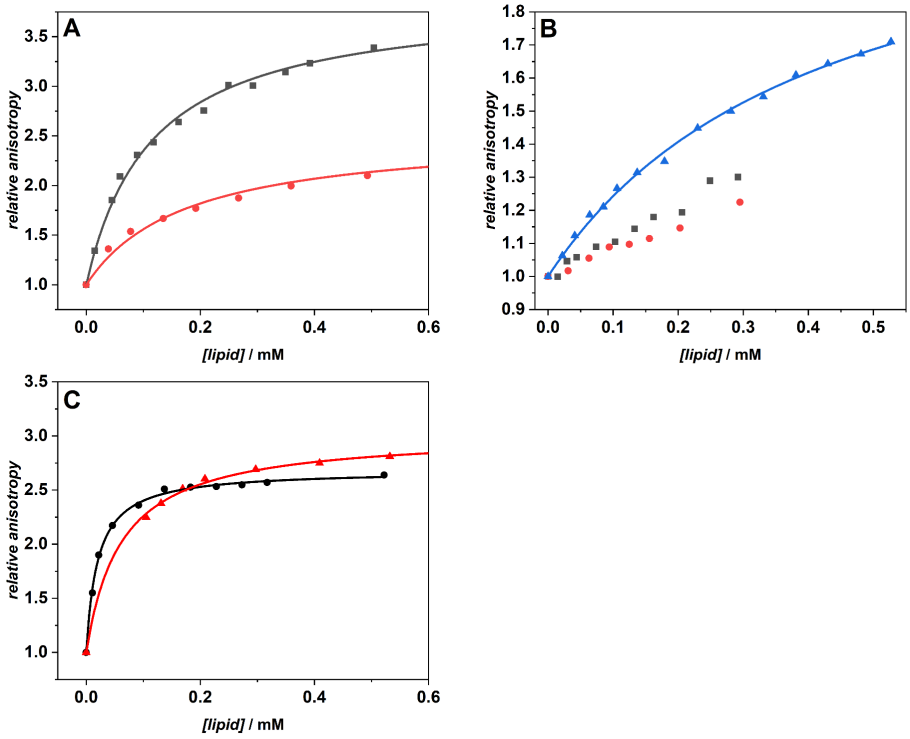

Figure 4.4. Experimental data points of (A) G4-RNA vs DPPC/DPPG in K^+-buffer (black line), G4-RNA vs DPPC/POPS in K^+-buffer (B) G4-RNA vs POPC in K^+-buffer (black line), G4-RNA vs POPC/POPG in K^+-buffer (red line), G4-RNA vs POPC/POPS in K^+-buffer (blue line) (C) G4-RNA vs DPPC in K^+-buffer (black line), G3U2 vs DPPC in K^+-buffer (red line).

Further, very small changes of fluorescence anisotropy on increasing POPC and POPC/POPG liposomes for G4-RNA were observed (Fig. 4.3) revealing negligible binding for the liquid phases. These results reveal that G4-RNA has a much higher propensity to interact with gel lipid bilayers electrically neutral in comparison with the DNA counterpart. Further, only G4-RNA is able to strongly interact with the negatively charged membrane. This finding is also relevant since many biological membranes are negatively charged and thus membrane charge could have fine-tuned membrane-quadruplex interaction (or *viceversa*) from an evolutionary point of view[237,238].

To check if the binding was specific to a particular headgroup type, rather than being just influenced by lipid charge, G4-RNA was also titrated with a DPPC/POPS membrane, which has the same negative charge of DPPC/DPPG but different headgroup shape (PG was replaced with PS) (Fig.4.4A). Remarkably, the K_x obtained for DPPC/POPS was similar to the one obtained for DPPC/DPPG, indicating that the binding is mostly determined by the overall membrane charge, rather than from headgroups type. The same experiment was performed with the correspondent fluid phase membrane (POPC/POPS) (Fig.4.4B). Surprisingly, in this case it was possible to determine a partition constant, while it was not for POPC and POPC/POPG. This result can be explained taking into account that PS headgroups can specifically bind calcium ions and upon binding the membrane becomes stiffer[239]. Likely, the increased membrane stiffness increases the binding affinity of the RNA for this membrane. Furtherly, a second RNA quadruplex named G3U2 (Fig.4.4C) was tested. The quadruplex was previously reported to be parallel and monomolecular[240] and it showed a partition constant similar to G4-RNA, suggesting that the formation of a parallel RNA G-quadruplex is needed for a strong binding to the membrane.

To further assess whether the high affinity of G4-RNA for DPPC and DPPC/DPPG bilayers is specific to the G-quadruplex structure, the experiment was repeated in a Li^+-containing buffer, which inhibits quadruplex formation, as evidenced by the corresponding CD spectrum and the absence of cooperative melting behaviour (Fig. 4.5). Under these conditions, a fivefold decrease in the binding constant (K_x) was observed for both membranes compared to the K^+-containing buffer (Fig. 4.2 and Table 4.2). Interestingly, the CD spectrum recorded in Li^+ showed an increase in intensity upon addition of DPPC, suggesting that the RNA strand partially refolds into a G4 structure upon membrane binding (Fig. 4.5A). This interpretation is further supported by the observation of a cooperative CD melting transition in the presence of DPPC (Fig. 4.5B). Such behaviour was not detected for the DPPC/DPPG membrane.

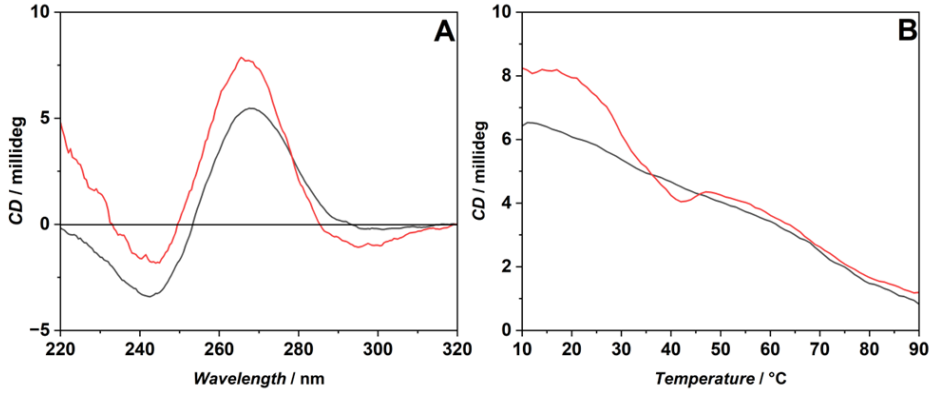

Figure 4.5. (A) CD spectra of G4-RNA in the absence (black line) and in the presence of DPPC (red line). (B) thermal melting behaviour of G4-RNA in the absence (black line) and in the presence of DPPC (red line). All the experiments were performed in lithium buffer.

To exclude the possibility of G4 formation as the sole cause of the observed binding, the experiment was repeated using a mutated RNA sequence (mut-RNA) that is unable to form G4 structures even in K^+-containing buffer (Table 4.1). The mut-RNA did not bind to the liposomes, confirming that the G4 structure is essential for membrane association (Fig. 4.2, Table 4.2). This finding aligns with recent computational studies indicating that RNA structural order plays a major role in modulating RNA–lipid interactions[241]. The binding of cMyc in Li^+ buffer to DPPC and DPPC/DPPG membranes was also examined. No binding was detected, further supporting the key role of the parallel G4 topology in mediating membrane association (Fig. 4.3). To assess the influence of G4 topology on membrane–quadruplex interactions, additional experiments were carried out using the FAM-labelled Tel23 sequence in K^+ buffer, as this DNA sequence is known to adopt a mixed-type topology under these conditions[242]. A measurable change in fluorescence anisotropy was observed upon increasing the DPPC concentration; however, it was not possible to obtain a complete binding isotherm, indicating a weak interaction ($K_x < 10^4$). An even smaller signal change was detected in the presence of DPPC/DPPG (Fig. 4.3). Taken together, these results indicate that both the quadruplex topology and the nature of the nucleic acid influence the strength of membrane binding, following the affinity order (for DPPC): parallel G4 RNA > parallel G4 DNA > hybrid G4 DNA > unfolded RNA/DNA. Notably, the parallel G4 RNA was the only structure that exhibited strong binding to the negatively charged DPPC/DPPG membrane. To validate these findings, confocal fluorescence microscopy was performed using fluorescently labelled giant unilamellar vesicles (GUVs) and labelled oligonucleotides (Fig. 4.2). Co-localization of the oligonucleotides with the membrane surface was confirmed for G4-RNA, cMyc, and Tel23 on DPPC

membranes, and for G4-RNA on DPPC/DPPG membranes. No co-localization was detected for cMyc with DPPC/DPPG or for mut-RNA with DPPC, in full agreement with the fluorescence binding experiments.

Table 4.2. Partition constants (K_x) of the systems explored in this work.

Oligonucleotide	Membrane	Buffer	K_x
FAM-G4-RNA	DPPC	10 mM K^+, 2 mM Ca^{2+}	$(2.6 \pm 1.0)\cdot10^6$
FAM-G4-RNA	DPPC/DPPG	10 mM K^+, 2 mM Ca^{2+}	$(4.9 \pm 0.3)\cdot10^5$
FAM-cMyc	DPPC	10 mM K^+, 2 mM Ca^{2+}	$(3.9 \pm 0.2)\cdot10^5$
FAM-cMyc	DPPC/DPPG	10 mM K^+, 2 mM Ca^{2+}	n.d.
FAM-Tel23	DPPC	10 mM K^+, 2 mM Ca^{2+}	n.d.
FAM-Tel23	DPPC/DPPG	10 mM K^+, 2 mM Ca^{2+}	n.d.
FAM-mut-RNA	DPPC	10 mM K^+, 2 mM Ca^{2+}	n.d.
FAM-G4-RNA	DPPC	10 mM Li^+, 2 mM Ca^{2+}	$(5.2 \pm 0.4)\cdot10^5$
FAM-G4-RNA	DPPC/DPPG	10 mM Li^+, 2 mM Ca^{2+}	$(8.4 \pm 0.2)\cdot10^4$
FAM-G4-RNA	DPPC/POPS	10 mM K^+, 2 mM Ca^{2+}	$(3.2 \pm 0.4)\cdot10^5$
FAM-cMyc	DPPC	10 mM Li^+, 2 mM Ca^{2+}	n.d.
FAM-cMyc	DPPC/DPPG	10 mM Li^+, 2 mM Ca^{2+}	n.d.
FAM-Tel23	DPPC	10 mM Li^+, 2 mM Ca^{2+}	n.d.
FAM-Tel23	DPPC/DPPG	10 mM Li^+, 2 mM Ca^{2+}	n.d.
FAM-G4-RNA	DPPC	10 mM K^+, 2 mM Mg^{2+}	$(7.6 \pm 0.6)\cdot10^5$
FAM-G4-RNA	DPPC	10 mM K^+, 2 mM Ca^{2+}, 0.5 M Na^+	$(4.5 \pm 0.8)\cdot10^5$
FAM-G4-RNA	DPPC	10 mM K^+, 2 mM Ca^{2+}, 1 M Na^+	$(3.6 \pm 0.5)\cdot10^5$
FAM-G4-RNA	DPPC/DPPG	10 mM K^+, 2 mM Ca^{2+}, 0.5 M Na^+	$(5.8 \pm 0.5)\cdot10^5$
FAM-cMyc	DPPC	10 mM K^+, 2 mM Ca^{2+}, 0.5 M Na^+	n.d.
FAM-cMyc	DPPC	10 mM K^+, 2 mM Ca^{2+}, 1 M Na^+	n.d.
FAM-G4-RNA	POPC	10 mM K^+, 2 mM Ca^{2+}	n.d.
FAM-G4-RNA	POPC/POPG	10 mM K^+, 2 mM Ca^{2+}	n.d.
FAM-G4-RNA	POPC/POPS	10 mM K^+, 2 mM Ca^{2+}	$(1.3 \pm 0.2)\cdot10^5$
FAM-cMyc	POPC	10 mM K^+, 2 mM Ca^{2+}	n.d.

4.3.2 Impact of membranes on G-quadruplex structure and stability

To test whether the interaction with the lipid bilayers affects G-quadruplex conformation and stability, a comparison of the CD spectra of all the RNA/DNA-liposome complexes with the CD spectra of the free oligonucleotides and the corresponding melting behaviour was performed. Overall, inspection of the CD spectra suggests that in all cases the GQ structure is maintained upon membrane binding (Fig. 4.6).

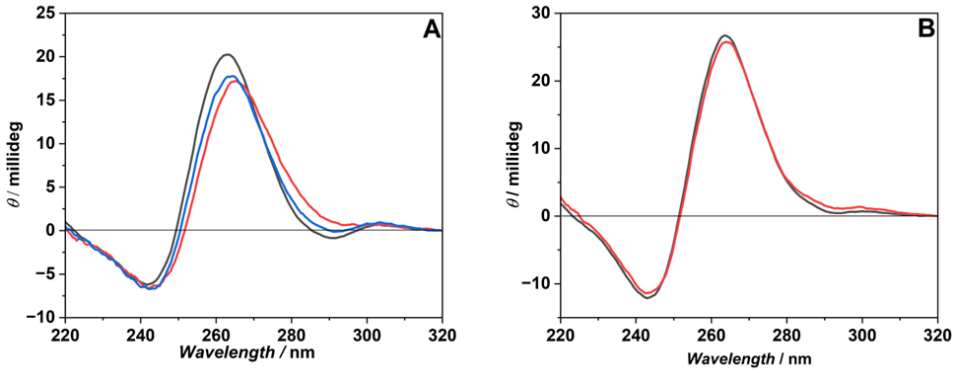

Figure 4.6 (A) CD spectra of G4-RNA alone (black line) and in the presence of DPPC (red line) or DPPC/DPPG (blue line). (B) CD spectra of cMyc (black line) and in the presence of DPPC. All experiments were performed in potassium buffer.

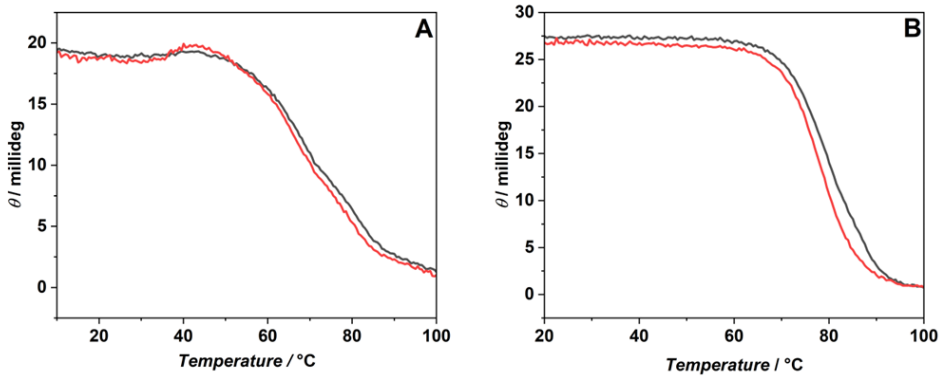

Figure 4.7. (A) CD melting of G4-RNA in the absence (black line) and in the presence of DPPC/DPPG (red line). (B) CD melting of cMyc in absence (black line) and in the presence DPPC (red line). All experiments were performed in potassium buffer.

Minor spectral variations were detected only for the G4-RNA–membrane complexes, characterized by a slight decrease in CD intensity upon addition of DPPC and DPPC/DPPG, accompanied by a small red shift of the main peak. Interestingly, the melting profile of G4-RNA in the presence of DPPC displayed a complex behaviour, with an initial decrease in CD signal between 10 and 35 °C, followed by an increase between 35 and 60 °C, and a subsequent decrease from 60 to 100 °C (Fig. 4.8A). The initial decrease in CD intensity suggests a destabilization of the G4 structure when bound to the membrane in its gel phase. The subsequent increase in CD signal within the 35–60 °C range can be explained by the gel-to-liquid crystalline transition of the membrane occurring at approximately 40 °C[243], during which the RNA G4 is released from the bilayer (as it does not associate with the liquid phase) and refolds into its G4 structure in solution. Above 60 °C, the melting profile closely resembles that observed in the absence of membranes, indicating that the G4-RNA melts primarily as a free quadruplex. To confirm this interpretation, the temperature-dependent CD

intensity was compared with the membrane gel-to-liquid transition profile obtained by monitoring the fluorescence anisotropy of the probe DPH embedded in the DPPC bilayer (see Materials and Methods) in the presence of G4-RNA. The comparison between the anisotropy melting curve and the CD data confirms that G4-RNA detachment initiates at the onset of the gel-to-liquid transition and progresses gradually with increasing temperature (Fig. 4.8B). It is noteworthy that around physiological temperature (37 °C), interactions with the zwitterionic membrane significantly influence the G4-RNA conformation. In contrast, the CD melting profiles of G4-RNA–DPPC/DPPG and cMyc–DPPC complexes were nearly identical to those of the free G4s (Fig. 4.7), indicating that the G4 structures are preserved at least within the 10–40 °C range, where the membrane remains in the gel phase and the G4s are likely bound to the membrane surface.

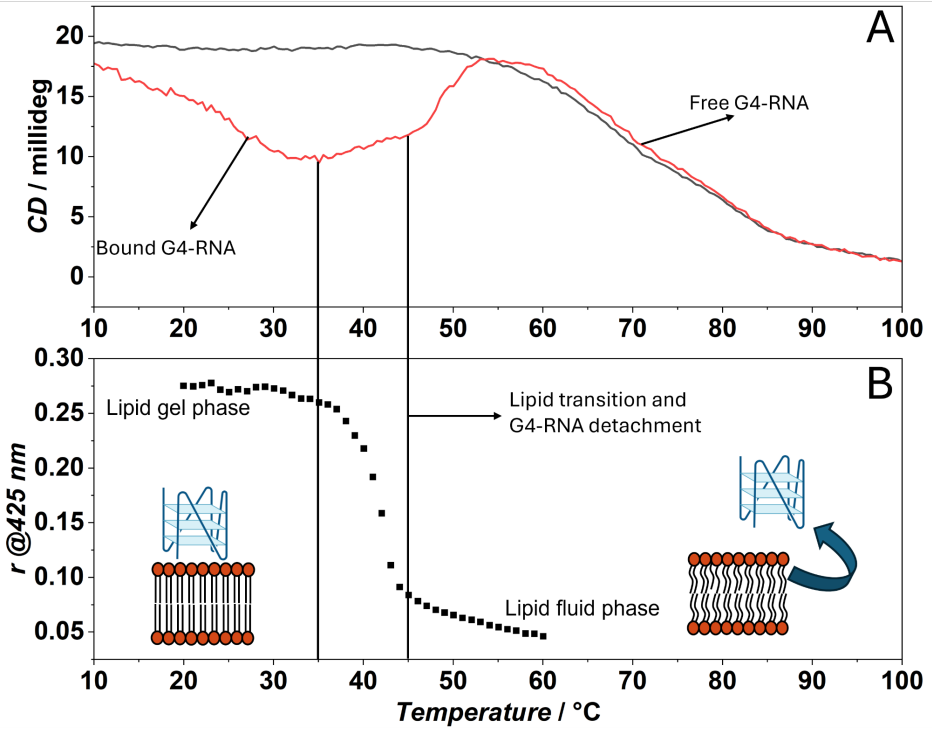

Figure 4.8. (A) CD melting profiles of G4-RNA in absence (black) and in the presence (red) of DPPC. (B) Gel-to-liquid transition of DPPC in the presence of G4-RNA monitored by following the fluorescence anisotropy of the DPH probe.

4.3.3 Energetics of G-quadruplex-membrane interaction

Subsequently, the energetics of membrane-quadruplex binding was explored by means of isothermal titration calorimetry (ITC). Particularly, the ITC experiments were designed to measure the binding enthalpy[101,244] and calculate the other thermodynamic quantities using the partition constant (see Table 4.2). A favourable entropic contribution was measured ($T\Delta S_x^0$, < 0) with almost no

measurable enthalpy change except for the G4 RNA showing also a favourable enthalpic contribution (Fig. 4.9, Fig. 4.10 and Table 4.3).

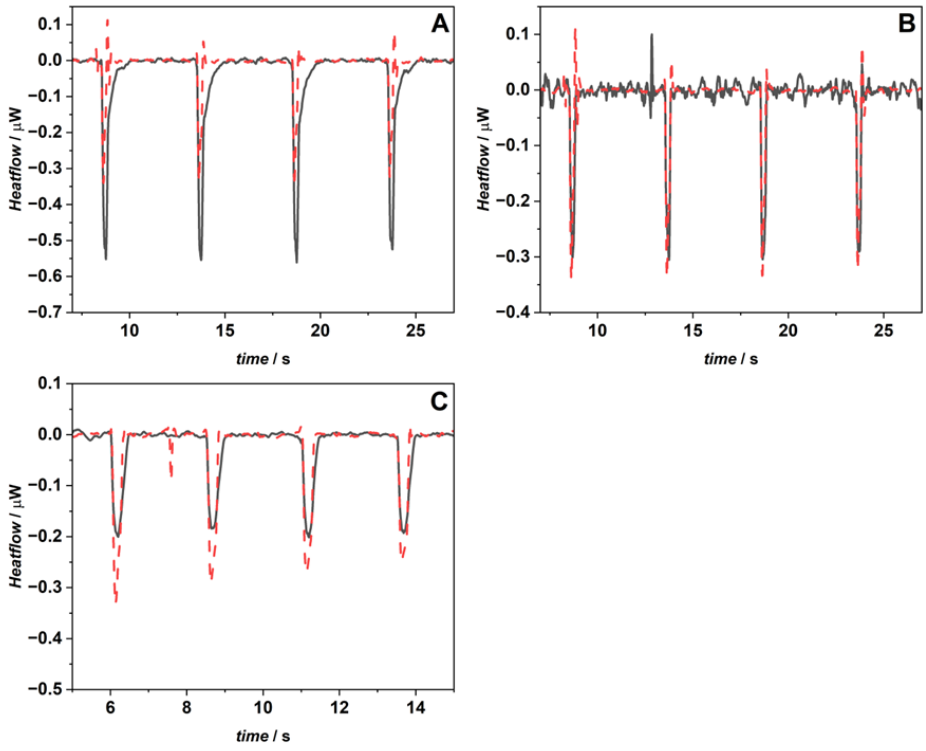

Figure 4.9. ITC traces (black lines) obtained from the titration of (A) 5 mM DPPC suspension with 50 µM G4-RNA solution, (B) 5 mM DPPC/DPPG suspension with 50 µM G4-RNA solution and (C) 5 mM of DPPC suspension with 50 µM of cMyc. The corresponding dilution heats are reported with a dashed red line. All experiments were performed in potassium buffer.

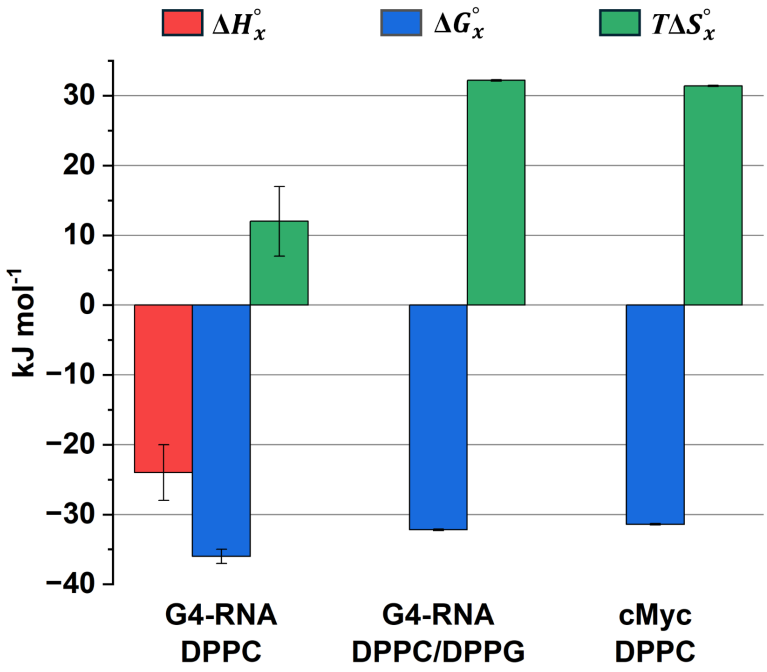

Figure 4.10. Thermodynamic signatures for RNA and DNA G4s partition into the lipid bilayers. The sum of the partition enthalpy, ΔH_x^0, (red) and the partition entropy multiplied by the absolute temperature, $T\Delta S_x^0$, (green) provides the partition Gibbs energy, ΔG_x^0 (blue). All the thermodynamic parameters are given at 20 °C (T = 293 K). The corresponding G4 and membrane lipid composition are indicated below the bars.

Table 4.3. Thermodynamic parameters for the oligonucleotide-membrane interaction: partition constants (K_x), standard Gibbs free energies of partition (ΔG^0), standard enthalpies of partition (ΔH^0), the standard entropic terms of partition ($T\Delta S^0$)

Sequence	Membrane	K_x	ΔG^0 kJ mol^{-1}	ΔH^0 kJ mol^{-1}	$T\Delta S^0$ kJ mol^{-1} K^{-1}
G4-RNA	DPPC	$(2.6 \pm 1.0)\cdot 10^6$	-36.0±1.0	-24±4	12±5
G4-RNA	DPPC/ DPPG	$(4.9 \pm 0.3)\cdot 10^5$	-32.2±0.1	n.d.	32.2±0.1
cMyc	DPPC	$(3.9 \pm 0.2)\cdot 10^5$	-31.4±0.1	n.d.	31.4±0.1

The favourable entropic contribution points toward an electrostatic driving force of the binding process which is accompanied by a release of hydration water and/or counterions[245,246], whereas the negative enthalpic contribution for the G4-RNA DPPC binding process suggests the presence of specific G4-lipid interactions. Overall, these results show that RNA and DNA G-quadruplexes differ in their binding energetics with DPPC bilayer.

4.3.4 Impact of ionic strength on G-quadruplex-membrane interaction

To further assess the role of electrostatic interactions, the effects of ionic strength and divalent cation concentration were evaluated on the binding of G4-RNA and cMyc to DPPC liposomes (Fig. 4.11–4.13). As a first comparison, the influence of Mg^{2+} (Fig. 4.11A) was measured. The binding constant obtained in the presence of Mg^{2+} was markedly lower than that measured with Ca^{2+}. This difference may be attributed to the smaller ionic radius of Mg^{2+}, which could hinder its coordination to the membrane and possibly reduce its mediating effect on the G-quadruplex. Next, the specific role of Ca^{2+} was explored (Fig. 4.11B) while

maintaining a constant K^+ concentration. Interestingly, G4-RNA bound to DPPC even in the absence of Ca^{2+}, yielding a sigmoidal binding curve suggestive of cooperative binding under these conditions. This type of curve could not be reliably fitted. However, the addition of Ca^{2+} at concentrations as low as 0.05 mM largely diminished the sigmoidal behaviour, allowing the curve to be fitted, albeit imperfectly. Further increases in Ca^{2+} concentration rapidly led to a plateau, with Kx values exceeding 10^6. Taken together, these results indicate that G4-RNA can interact with membranes even without divalent cations. Nevertheless, the presence of very low concentrations of divalent cations is sufficient to dramatically enhance the binding constant, highlighting their key role in modulating the interaction, even if they are not strictly required.

Increasing the ionic strength up to 1M of NaCl completely abolished the cMyc interaction as expected for a binding mainly driven by electrostatic. On the other hand, the partition constant for the G4-RNA remains greater than 10^5 even at the highest ionic strength explored, indicating a great non-electrostatic contribution to the binding in agreement with the ITC results and other studies on RNA[129]. Prompted by these results the effect of the ionic strength on the G4-RNA with the negatively charged DPPC/DPPG membrane was also explored (Fig. 4.13). Interestingly, the presence of high ionic strength almost did not affect the G4-RNA interactions with the membrane, suggesting that in this case a great non electrostatic contribution in the G4-RNA interaction with the membrane. Overall, these results suggest that the electrostatic interactions play a different role in

modulating the RNA and DNA G-quadruplex interaction with the lipid bilayers.

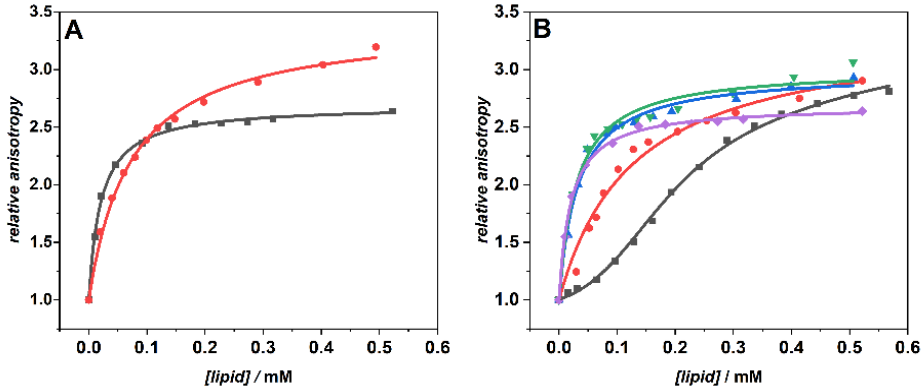

Figure 4.11 (A) G4-RNA vs DPPC binding in the presence of Ca^{2+} ion (black line), G4-RNA vs DPPC binding in the presence of Mg^{2+} ion (red line). (B) Binding of G4-RNA in the presence of 0 mM Ca^{2+} (black line), 0.05 mM Ca^{2+} (red line), 0.2 mM Ca^{2+} (blue line), 0.5 Ca^{2+} (green line), 2 mM Ca^{2+} (violet line).

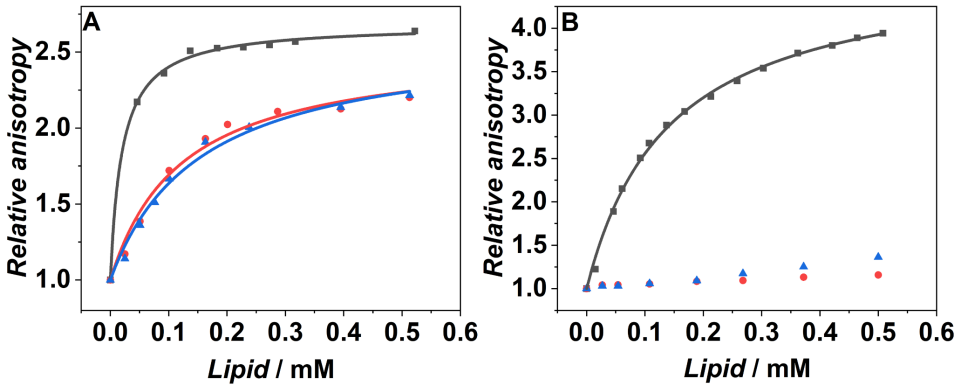

Figure 4.12 (A) Binding curves G4-RNA and (B) cMyc with DPPC in K+-buffer (black) and in the presence of 0.5 M NaCl (red) and 1 M NaCl (blu).

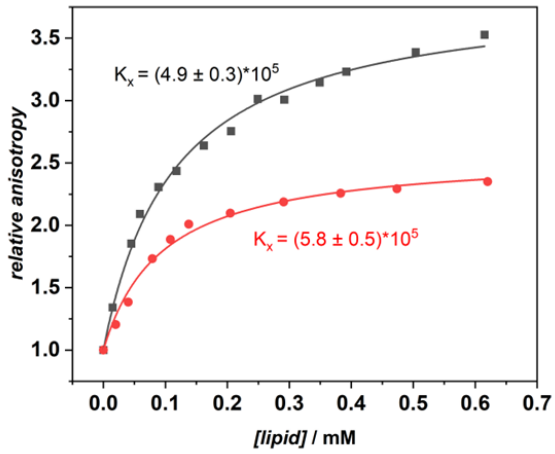

Figure 4.13. Binding curves of G4-RNA vs DPPC/DPPG in potassium buffer in the absence (black line) and in the presence of 0.5 M NaCl (red line)

4.3.5 Impact of G-quadruplexes on membrane stability

The impact of G-quadruplexes on membrane stability was initially assessed through fluorescence anisotropy melting experiments of DPPC and DPPC/DPPG liposomes, using the fluorescent probe DPH embedded in the lipid bilayer. DPH anisotropy is sensitive to lipid phase: higher anisotropy values are observed in the tightly packed gel phase, while lower values correspond to the more disordered fluid phase. The inflection point of these melting curves is generally associated with the lipid phase transition temperature. The complete set of melting profiles is shown in Fig. 4.14. In the presence of G4-RNA, DPPC displayed a slight increase in anisotropy in both gel and fluid phases, accompanied by an increase of the melting temperature by ~1 °C (Fig. 4.14A). The effects observed for DPPC/DPPG in the presence of G4-RNA, as well as for DPPC in the presence of

cMyc, were smaller and within the range of systematic error associated with the temperature controller.

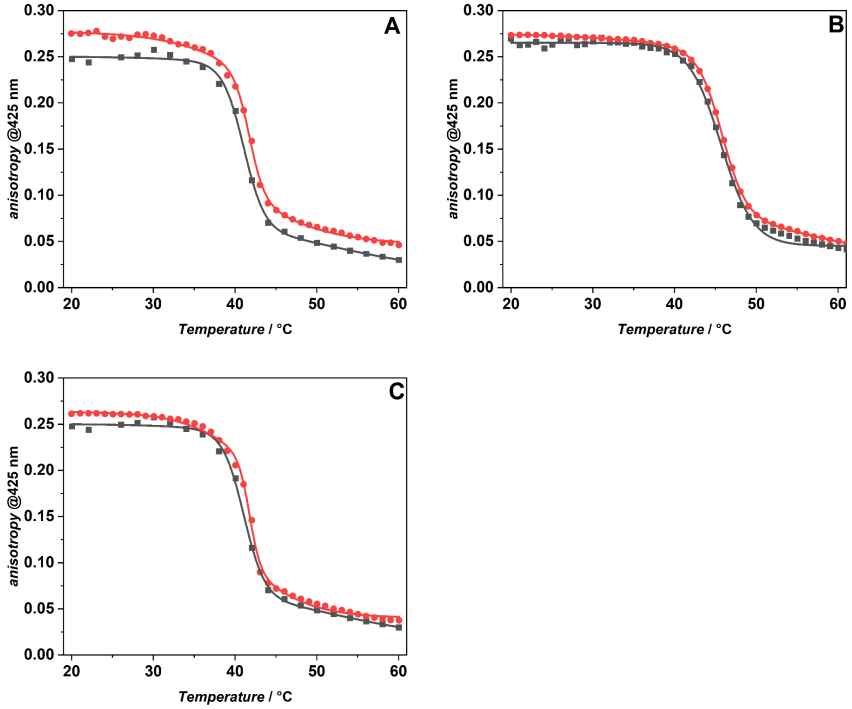

Figure 4.14. DPH meltings of (A) DPPC (black line) and DPPC+ G4-RNA (red line), (B) DPPC/DPPG (black line) and DPPC/DPPG + G4-RNA, (C) DPPC (black line) and DPPC+cMyc (red line). All the experiments were performed in K^+-buffer.

Further insights on the impact of G-quadruplexes on membrane properties were inferred from the Laurdan probe, which positions itself at the water-headgroup interface and due to its two different emitting states is able to closely monitor the hydration level of a membrane. Briefly, the emission spectra of Laurdan are composed of a solvent relaxed state (at higher wavelengths) and a non-solvent

relaxed state (at lower wavelengths). The hydration level is quantified *via* the GP parameter (see materials and methods). Temperature dependent GP-values of DPPC in the absence and in the presence of either G4-RNA or cMyc are reported in Fig.4.15. The GP values reported for G4-RNA (Fig.4.15A) indicate that the quadruplex is able to perturb the membrane surface, inducing a slightly less dehydrated membrane. On the other hand, GP values obtained for cMyc (Fig.4.15B) were almost superimposable to DPPC membrane alone making it impossible to retrieve any information.

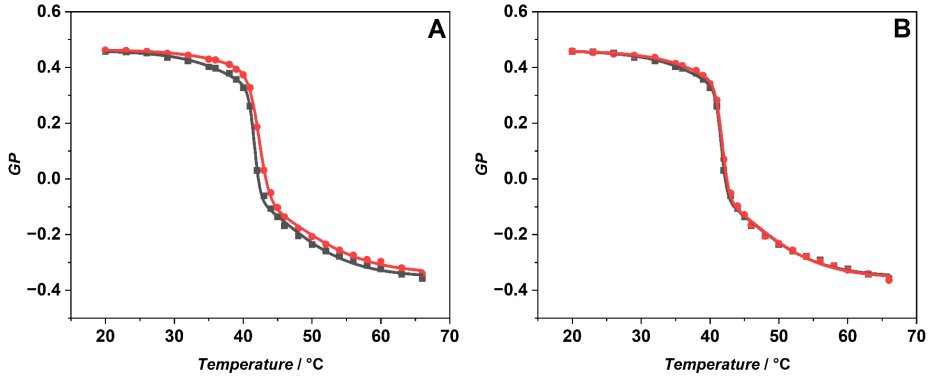

Figure 4.15. GP dependent curves of DPPC in the absence (black line) and in the presence of G4-RNA (red line, panel A) and cMyc (red line, panel B).

To better understand the impact that G-quadruplexes have on membranes, differential scanning calorimetry (DSC) was employed. The main focus was on the DPPC membrane as it has the highest affinity for both G4-RNA and cMyc. The DSC thermograms of pure DPPC MLVs in the absence of RNA/DNA are very similar and characterized by two well-defined transitions (Fig. 4.16): the pre-transition at lower temperature (involving the rearrangement of polar head groups)

followed by the main gel-to-fluid transition (involving mainly the melting of the lipid chains) [247,248]. Analysis of the DSC profiles shows that both G4-RNA and cMyc affect the melting profiles of the DPPC liposomes changing both the pre-transition and the main transition peak. Particularly, the G4-RNA turns the DPPC main transition peak in a multicomponent profile revealing that G4-RNA has a much drastic effect on the membrane properties in comparison with the cMyc. On the other hand, the small variation observed on the main transition enthalpy (table 4.4) suggests that both G4s do not enter in the hydrophobic core of the bilayer but rather bind at the membrane-water interface.

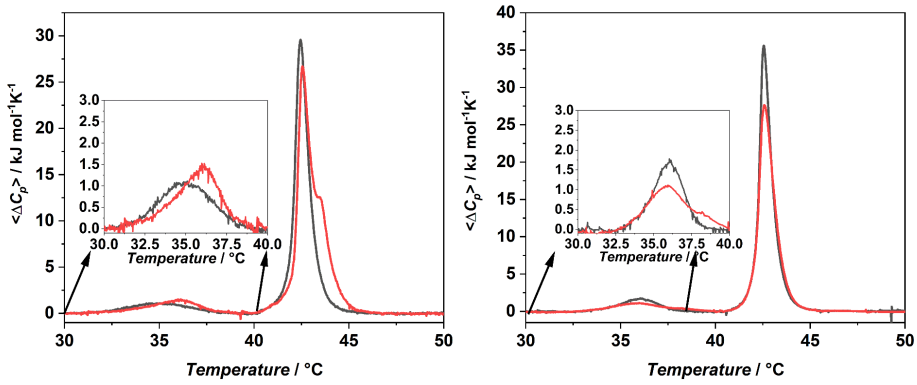

Figure 4.16. DSC thermograms of DPPC MLVs in the absence (black line) and in the presence of G4-RNA (red line, panel A) and cMyc (red line, panel B). The insets show an enlargement of the pre-transition peaks.

Table 4.4. Thermodynamic parameters for the membrane gel-to-liquid transition obtained by DSC.

System	T_p[a] °C	ΔH_p[a] kJ mol^{-1}	T_m[b] °C	ΔH_m[b] kJ mol^{-1}
DPPC	35.2±0.2	4.4±0.2	42.4±0.2	30.5±1.5
+G4-RNA L/Q = 10	36.1±0.2	4.5±0.2	42.6±0.2	34.8±1.7
DPPC	36.0±0.2	3.9±0.2	42.6±0.2	32.8±1.6
+cMyc L/Q = 10	35.9±0.2	4.0±0.2	42.6±0.2	30.8±1.4
DPPC/DPPG	34.9±0.2	1.7±0.2	45.0±0.4	52.6±2.6
+G4-RNA L/Q = 10	34.4±0.2	1.8±0.2	45.9±0.4	57.4±2.8

(a) Transition temperature and enthalpy change for the transition from the gel phase ($L_{\beta'}$) to the rippled gel phase ($P_{\beta'}$) (T_p, ΔH_p); (b) transition temperature and enthalpy change for the transition from the rippled gel phase ($P_{\beta'}$) to the liquid crystalline phase (L_α) (T_m, ΔH_m)

The same experiment was performed also for DPPC/DPPG membrane, trying to highlight differences with DPPC membrane. Even in this case the DSC thermogram of DPPC/DPPG is composed of two distinguished peaks (Fig. 4.17): the pretransition at lower temperature and the main transition peak at higher temperature. The pretransition in this case has a much lower ΔH_p since it can only be ascribed to the DPPC lipid. However, the addition of G4-RNA did not change the profile and enthalpy of the pretransition peak (Table 4.4). On the other hand, the main transition peak was changed by the addition of G4-RNA with an increase in melting temperature and enthalpy. The slight increase in the transition enthalpy suggests that G4-RNA does not penetrate into the hydrophobic core but binds on the membrane surface

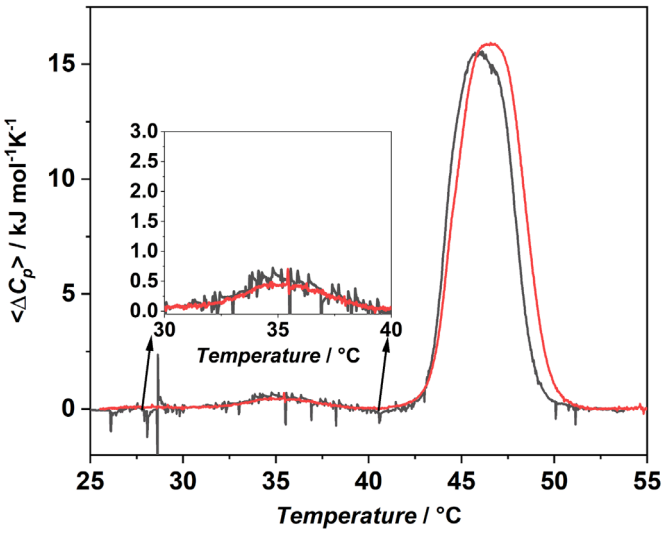

Figure 4.17. DSC thermograms of DPPC/DPPG MLVs in the absence (black line) and in the presence of G4-RNA (red line).

4.4 Conclusions

In conclusion, these data demonstrate that G4 interactions with membranes are strongly influenced by G4 topology, nucleic acid type (RNA vs. DNA), and the lipid composition of the bilayer. From an origins-of-life perspective, such interactions likely played a crucial role in guiding the earliest steps of molecular organization. G4–membrane binding may have promoted the localization and stabilization of G-rich oligonucleotides at primitive membrane surfaces, thereby fostering environments where nucleic acids could accumulate and interact. Moreover, the ability of G4s to modulate membrane properties suggests a potential feedback mechanism in which nucleic acids not only relied on

membranes for compartmentalization, but also influenced their physical state, possibly mediating primitive signalling or regulatory functions. Importantly, the observed dependence on ionic strength and divalent cation concentration highlights simple physicochemical parameters that could have fine-tuned G4–membrane interplay in prebiotic environments, providing an additional regulatory layer in the absence of proteins. Altogether, these findings support the view that G4 structures, particularly RNA G-quadruplexes, may have contributed to the emergence of functional protocell-like systems, bridging nucleic acid stability, compartmentalization, and primitive molecular regulation.

5 Bibliography

[1] A. A. Yayanos, "Evolutional and ecological implications of the properties of deep-sea barophilic bacteria" *Proc. Natl. Acad. Sci. U.S.A.* **1986**, *83*, 9542–9546.

[2] C. S. Cockell, *Astrobiology: Understanding Life in the Universe*, John Wiley & Sons, **2020**.

[3] N. Merino, H. S. Aronson, D. P. Bojanova, J. Feyhl-Buska, M. L. Wong, S. Zhang, D. Giovannelli, "Living at the Extremes: Extremophiles and the Limits of Life in a Planetary Context" *Frontiers in Microbiology* **2019**, *10*.

[4] I. Daniel, P. Oger, R. Winter, "Origins of life and biochemistry under high-pressure conditions" *Chem. Soc. Rev.* **2006**, *35*, 858–875.

[5] P. M. Oger, M. Jebbar, "The many ways of coping with pressure" *Research in Microbiology* **2010**, *161*, 799–809.

[6] F. Meersman, I. Daniel, D. H. Bartlett, R. Winter, R. Hazael, P. F. McMillan, "High-Pressure Biochemistry and Biophysics" *Reviews in Mineralogy and Geochemistry* **2013**, *75*, 607–648.

[7] H. Wang, Y. Zhang, D. H. Bartlett, X. Xiao, "Transcriptomic Analysis Reveals Common Adaptation Mechanisms Under Different Stresses for Moderately Piezophilic Bacteria" *Microb Ecol* **2021**, *81*, 617–629.

[8] J.-M. Knop, S. Mukherjee, M. W. Jaworek, S. Kriegler, M. Manisegaran, Z. Fetahaj, L. Ostermeier, R. Oliva, S. Gault, C. S. Cockell, R. Winter, "Life in Multi-Extreme Environments: Brines, Osmotic and Hydrostatic Pressure─A Physicochemical View" *Chem. Rev.* **2023**, *123*, 73–104.

[9] W. Stillwell in *An Introduction to Biological Membranes*, Elsevier, **2016**, pp. 3–15.

[10] N. Sugimoto, Ed. , *Handbook of Chemical Biology of Nucleic Acids*, Springer Nature Singapore, Singapore, **2023**.

[11] D. Voet, J. G. Voet, *Biochemistry*, New York : J. Wiley & Sons, **2004**.

[12] D. L. Nelson, M. M. Cox, A. A. Hoskins, "Lehninger Principles of Biochemistry" **n.d.**, 4381.

[13] M. J. Daly, "A new perspective on radiation resistance based on Deinococcus radiodurans" *Nat Rev Microbiol* **2009**, *7*, 237–245.

[14] V. J. Laye, S. DasSarma, "An Antarctic Extreme Halophile and Its Polyextremophilic Enzyme: Effects of Perchlorate Salts" *Astrobiology* **2018**, *18*, 412–418.

[15] K. Takai, D. P. Moser, T. C. Onstott, N. Spoelstra, S. M. Pfiffner, A. Dohnalkova, J. K. Fredrickson, "Alkaliphilus transvaalensis gen. nov., sp. nov., an extremely alkaliphilic bacterium isolated from a deep South African gold mine." *International Journal of Systematic and Evolutionary Microbiology* **2001**, *51*, 1245–1256.

[16] C. Schleper, G. Puehler, I. Holz, A. Gambacorta, D. Janekovic, U. Santarius, H. P. Klenk, W. Zillig, "Picrophilus gen. nov., fam. nov.: a novel aerobic, heterotrophic, thermoacidophilic genus and family comprising archaea capable of growth around pH 0" *Journal of Bacteriology* **1995**, *177*, 7050–7059.

[17] L. Carré, D. Gonzalez, É. Girard, B. Franzetti, "Effects of chaotropic salts on global proteome stability in halophilic archaea: Implications for life signatures on Mars" *Environmental Microbiology* **2023**, 1462-2920.16451.

[18] L. García-Descalzo, M. Á. Lezcano, D. Carrizo, A. G. Fairén, "Changes in membrane fatty acids of a halo-psychrophile exposed to magnesium perchlorate and low temperatures: Implications for Mars habitability" *Frontiers in Astronomy and Space Sciences* **2023**, *10*.

[19] M. Kusube, T. S. Kyaw, K. Tanikawa, R. A. Chastain, K. M. Hardy, J. Cameron, D. H. Bartlett, "Colwellia marinimaniae sp. nov., a hyperpiezophilic species isolated from an amphipod within the Challenger Deep, Mariana Trench" *International Journal of Systematic and Evolutionary Microbiology* **2017**, *67*, 824–831.

[20] E. E. Allen, D. Facciotti, D. H. Bartlett, "Monounsaturated but Not Polyunsaturated Fatty Acids Are Required for Growth of the Deep-Sea BacteriumPhotobacterium profundum SS9 at High Pressure and Low Temperature" *Applied and Environmental Microbiology* **1999**, *65*, 1710–1720.

[21] A. Chytła, S. Rattay, B. Akgül, M. Sztacho, "Plasma membrane and nuclear phosphatidylinositol 4,5-bisphosphate signalling in cancer" *Lipids Health Dis* **2025**, *24*, 39.

[22] K. Jahnke, O. Staufer, "Membranes on the move: The functional role of the extracellular vesicle membrane for contact-dependent cellular signalling" *Journal of Extracellular Vesicles* **2024**, *13*, e12436.

[23] X. Cheng, J. C. Smith, "Biological Membrane Organization and Cellular Signaling" *Chem. Rev.* **2019**, *119*, 5849–5880.

[24] N. Ando, B. Barquera, D. H. Bartlett, E. Boyd, A. A. Burnim, A. S. Byer, D. Colman, R. E. Gillilan, M. Gruebele, G. Makhatadze, C. A. Royer, E. Shock, A. J. Wand, M. B. Watkins, "The Molecular Basis for Life in Extreme Environments" *Annual Review of Biophysics* **2021**, *50*, 343–372.

[25] J. Atalah, P. Cáceres-Moreno, G. Espina, J. M. Blamey, "Thermophiles and the applications of their enzymes as new biocatalysts" *Bioresource Technology* **2019**, *280*, 478–488.

[26] T. Collins, G. Feller, "Psychrophilic enzymes: strategies for cold-adaptation" *Essays Biochem* **2023**, *67*, 701–713.

[27] J. Xue, J. Fang, H. Zhang, Y. Wei, L. Wang, R. Liu, J. Cao, "Complete genome sequence of a piezophilic bacterium *Salinimonas sediminis* N102T,

isolated from deep-sea sediment of the New Britain Trench" *Marine Genomics* **2021**, *56*, 100807.

[28] Y. SAKO, N. NOMURA, A. UCHIDA, Y. ISHIDA, H. MORII, Y. KOGA, T. HOAKI, T. MARUYAMA, "Aeropyrum pernix gen. nov., sp. nov., a Novel Aerobic Hyperthermophilic Archaeon Growing at Temperatures up to 100°C" *International Journal of Systematic and Evolutionary Microbiology* **1996**, *46*, 1070–1077.

[29] M. C. Mudge, B. L. Nunn, E. Firth, M. Ewert, K. Hales, W. E. Fondrie, W. S. Noble, J. Toner, B. Light, K. A. Junge, "Subzero, saline incubations of Colwellia psychrerythraea reveal strategies and biomarkers for sustained life in extreme icy environments" *Environmental Microbiology* **2021**, *23*, 3840–3866.

[30] I. Raymond-Bouchard, K. Chourey, I. Altshuler, R. Iyer, R. L. Hettich, L. G. Whyte, "Mechanisms of subzero growth in the cryophile Planococcus halocryophilus determined through proteomic analysis" *Environmental Microbiology* **2017**, *19*, 4460–4479.

[31] G. M. Martínez, C. Pire, R. M. Martínez-Espinosa, "Hypersaline environments as natural sources of microbes with potential applications in biotechnology: The case of solar evaporation systems to produce salt in Alicante County (Spain)." *Current Research in Microbial Sciences* **2022**, *3*, 100136.

[32] E. González, F. Vera, F. Scott, C. Guerrero, J. M. Bolívar, G. Aroca, J. Á. Muñoz, M. Ladero, V. E. Santos, "Acidophilic heterotrophs: basic aspects and technological applications" *Front. Microbiol.* **2024**, *15*, DOI 10.3389/fmicb.2024.1374800.

[33] L. Preiss, D. B. Hicks, S. Suzuki, T. Meier, T. A. Krulwich, "Alkaliphilic Bacteria with Impact on Industrial Applications, Concepts of Early Life Forms, and Bioenergetics of ATP Synthesis" *Front. Bioeng. Biotechnol.* **2015**, *3*, DOI 10.3389/fbioe.2015.00075.

[34] L. Yi, R. Solanki, M. Strous, “In search of the pH limit of growth in halo-alkaliphilic cyanobacteria” *Environmental Microbiology Reports* **2024**, *16*, e13323.

[35] L. J. Rothschild, R. L. Mancinelli, “Life in extreme environments” *Nature* **2001**, *409*, 1092–1101.

[36] J. P. Harrison, N. Gheeraert, D. Tsigelnitskiy, C. S. Cockell, “The limits for life under multiple extremes” *Trends in Microbiology* **2013**, *21*, 204–212.

[37] A. Munguira, R. Hueso, A. Sánchez-Lavega, M. de la Torre-Juarez, G. M. Martínez, C. E. Newman, E. Sebastian, A. Lepinette, A. Vicente-Retortillo, B. Chide, M. T. Lemmon, T. Bertrand, R. D. Lorenz, D. Banfield, J. Gómez-Elvira, J. Martín-Soler, S. Navarro, J. Pla-García, J. A. Rodríguez-Manfredi, J. Romeral, M. D. Smith, J. Torres, “Near Surface Atmospheric Temperatures at Jezero From Mars 2020 MEDA Measurements” *Journal of Geophysical Research: Planets* **2023**, *128*, e2022JE007559.

[38] N. Naz, B. F. Harandi, J. Newmark, S. P. Kounaves, “Microbial growth in actual martian regolith in the form of Mars meteorite EETA79001” *Commun Earth Environ* **2023**, *4*, 381.

[39] R. Karan, M. D. Capes, S. DasSarma, “Function and biotechnology of extremophilic enzymes in low water activity” *Aquatic Biosystems* **2012**, *8*, 4.

[40] S. Fukuchi, K. Yoshimune, M. Wakayama, M. Moriguchi, K. Nishikawa, “Unique Amino Acid Composition of Proteins in Halophilic Bacteria” *Journal of Molecular Biology* **2003**, *327*, 347–357.

[41] C. J. Reed, H. Lewis, E. Trejo, V. Winston, C. Evilia, “Protein Adaptations in Archaeal Extremophiles” *Archaea* **2013**, *2013*, 1–14.

[42] M. F. Siliakus, J. van der Oost, S. W. M. Kengen, “Adaptations of archaeal and bacterial membranes to variations in temperature, pH and pressure” *Extremophiles* **2017**, *21*, 651–670.

[43] A. Anesi, U. Obertegger, G. Hansen, A. Sukenik, G. Flaim, G. Guella, “Comparative Analysis of Membrane Lipids in Psychrophilic and Mesophilic Freshwater Dinoflagellates” *Front. Plant Sci.* **2016**, *7*, DOI 10.3389/fpls.2016.00524.

[44] N. J. Bale, D. Y. Sorokin, E. C. Hopmans, M. Koenen, W. I. C. Rijpstra, L. Villanueva, H. Wienk, J. S. Sinninghe Damsté, “New Insights Into the Polar Lipid Composition of Extremely Halo(alkali)philic Euryarchaea From Hypersaline Lakes” *Front. Microbiol.* **2019**, *10*, DOI 10.3389/fmicb.2019.00377.

[45] Y. Koga, “Thermal Adaptation of the Archaeal and Bacterial Lipid Membranes” *Archaea* **2012**, *2012*, 789652.

[46] A. Damjanović, M. Logarušić, L.-M. Tumir, T. Andreou, M. C. Bubalo, I. R. Redovniković, “Enhancing protein stability under stress: osmolyte-based deep eutectic solvents as a biocompatible and robust stabilizing medium for lysozyme under heat and cold shock” *Physical Chemistry Chemical Physics* **2024**, *26*, 21040–21051.

[47] J. K. Kaushik, R. Bhat, “Why Is Trehalose an Exceptional Protein Stabilizer?: AN ANALYSIS OF THE THERMAL STABILITY OF PROTEINS IN THE PRESENCE OF THE COMPATIBLE OSMOLYTE TREHALOSE*” *Journal of Biological Chemistry* **2003**, *278*, 26458–26465.

[48] E. Christodoulou, C. E. Vorgias, “The thermostability of DNA-binding protein HU from mesophilic, thermophilic, and extreme thermophilic bacteria” *Extremophiles* **2002**, *6*, 21–31.

[49] H. Lu, Y. Hua, “PprI: The Key Protein in Response to DNA Damage in Deinococcus” *Front. Cell Dev. Biol.* **2021**, *8*, DOI 10.3389/fcell.2020.609714.

[50] D. Slade, M. Radman, “Oxidative Stress Resistance in Deinococcus radiodurans” *Microbiology and Molecular Biology Reviews* **2011**, *75*, 133–191.

[51], “Biologia molecolare della cellula - Bruce Alberts, Alexander Johnson, Julian Lewis, David Morgan, Martin Raff, Keith Roberts, Peter Walter |

Zanichelli," can be found under https://www.zanichelli.it/ricerca/prodotti/biologia-molecolare-della-cellula-alberts-johnson-lewis-morgan-raff-roberts-walter(accessed 29 October 2025), **n.d.**

[52], "Biology,cell,diagram,science,membrane - free image from needpix.com," can be found under https://www.needpix.com/photo/32544/biology-cell-diagram-science-membrane-detail-health-research-scientific.(accessed 29 October 2025), **n.d.**

[53], "Membrane lipids: where they are and how they behave | Nature Reviews Molecular Cell Biology," can be found under https://www.nature.com/articles/nrm2330(accessed 29 October 2025), **n.d.**

[54], "Understanding the diversity of membrane lipid composition | Nature Reviews Molecular Cell Biology," can be found under https://www.nature.com/articles/nrm.2017.138(accessed 29 October 2025), **n.d.**

[55] J. C. Henderson, S. M. Zimmerman, A. A. Crofts, J. M. Boll, L. G. Kuhns, C. M. Herrera, M. S. Trent, "The Power of Asymmetry: Architecture and Assembly of the Gram-Negative Outer Membrane Lipid Bilayer" *Annual Review of Microbiology* **2016**, *70*, 255–278.

[56] J. Hoyo, J. Torrent-Burgués, T. Tzanov, "Physical states and thermodynamic properties of model gram-negative bacterial inner membranes" *Chemistry and Physics of Lipids* **2019**, *218*, 57–64.

[57] C. Sohlenkamp, O. Geiger, "Bacterial membrane lipids: diversity in structures and pathways" *FEMS Microbiol Rev* **2016**, *40*, 133–159.

[58] R. M. Epand, R. F. Epand, "Lipid domains in bacterial membranes and the action of antimicrobial agents" *Biochimica et Biophysica Acta (BBA) - Biomembranes* **2009**, *1788*, 289–294.

[59] T. Řezanka, L. Kyselová, D. J. Murphy, "Archaeal lipids" *Progress in Lipid Research* **2023**, *91*, 101237.

[60] Y. Koga, H. Morii, “Biosynthesis of Ether-Type Polar Lipids in Archaea and Evolutionary Considerations” *Microbiology and Molecular Biology Reviews* **2007**, *71*, 97–120.

[61] C. Jeworrek, F. Evers, M. Erlkamp, S. Grobelny, M. Tolan, P. L.-G. Chong, R. Winter, “Structure and Phase Behavior of Archaeal Lipid Monolayers” *Langmuir* **2011**, *27*, 13113–13121.

[62] B. M. Quinville, N. M. Deschenes, A. E. Ryckman, J. S. Walia, “A Comprehensive Review: Sphingolipid Metabolism and Implications of Disruption in Sphingolipid Homeostasis” *International Journal of Molecular Sciences* **2021**, *22*, 5793.

[63] I. Olsen, E. Jantzen, “Sphingolipids in Bacteria and Fungi” *Anaerobe* **2001**, *7*, 103–112.

[64] J. R. Silvius, “Role of cholesterol in lipid raft formation: lessons from lipid model systems” *Biochimica et Biophysica Acta (BBA) - Biomembranes* **2003**, *1610*, 174–183.

[65] A. B. García-Arribas, A. Alonso, F. M. Goñi, “Cholesterol interactions with ceramide and sphingomyelin” *Chemistry and Physics of Lipids* **2016**, *199*, 26–34.

[66] J. D. Weete, M. Abril, M. Blackwell, “Phylogenetic Distribution of Fungal Sterols” *PLOS ONE* **2010**, *5*, e10899.

[67] M.-A. Hartmann, “Plant sterols and the membrane environment” *Trends in Plant Science* **1998**, *3*, 170–175.

[68] J. Volkman, “Sterols in microorganisms” *Appl Microbiol Biotechnol* **2003**, *60*, 495–506.

[69] R. L. Schnaar, “Glycolipid-mediated cell–cell recognition in inflammation and nerve regeneration” *Archives of Biochemistry and Biophysics* **2004**, *426*, 163–172.

[70] D. M. Boes, A. Godoy-Hernandez, D. G. G. McMillan, “Peripheral Membrane Proteins: Promising Therapeutic Targets across Domains of Life” *Membranes* **2021**, *11*, 346.

[71] C. R. H. Raetz, C. Whitfield, “Lipopolysaccharide Endotoxins” *Annual Review of Biochemistry* **2002**, *71*, 635–700.

[72] C. Weidenmaier, A. Peschel, “Teichoic acids and related cell-wall glycopolymers in Gram-positive physiology and host interactions” *Nat Rev Microbiol* **2008**, *6*, 276–287.

[73] S. Brown, J. P. Santa Maria, S. Walker, “Wall Teichoic Acids of Gram-Positive Bacteria” *Annu. Rev. Microbiol.* **2013**, *67*, 313–336.

[74] S.-V. Albers, B. H. Meyer, “The archaeal cell envelope” *Nat Rev Microbiol* **2011**, *9*, 414–426.

[75] A. Varki, “Biological roles of glycans” *Glycobiology* **2017**, *27*, 3–49.

[76] A. Helenius, M. Aebi, “Roles of N-Linked Glycans in the Endoplasmic Reticulum” *Annual Review of Biochemistry* **2004**, *73*, 1019–1049.

[77] S. J. Singer, G. L. Nicolson, “The Fluid Mosaic Model of the Structure of Cell Membranes” *Science* **1972**, *175*, 720–731.

[78] Management, “How do lipid bilayer components move? - Mechanobiology Institute, National University of Singapore,” can be found under https://www.mbi.nus.edu.sg/mbinfo/how-do-lipid-bilayer-components-move/(accessed 29 October 2025), **2023**.

[79] M.-P. Nieh, F. A. Heberle, J. Katsaras, C. Bowerman, J. C. Bozelli Junior, M. F. Brown, P. D. Butler, C. Chan, X. Cheng, Y. Cherniavskyi, E. Cheung, C. E. Chini, A. F. Craig, C. Dabney-Smith, J. H. Davis, Eds. , *Characterization of biological membranes: structure and dynamics*, De Gruyter, Berlin Boston, **2019**.

[80] F. M. Goñi, “The basic structure and dynamics of cell membranes: An update of the Singer–Nicolson model” *Biochimica et Biophysica Acta (BBA) - Biomembranes* **2014**, *1838*, 1467–1476.

[81] P. J. Quinn, C. Wolf, “Thermotropic and structural evaluation of the interaction of natural sphingomyelins with cholesterol” *Biochimica et Biophysica Acta (BBA) - Biomembranes* **2009**, *1788*, 1877–1889.

[82] X. Gao, W. Liu, J. Mei, J. Xie, “Quantitative Analysis of Cold Stress Inducing Lipidomic Changes in Shewanella putrefaciens Using UHPLC-ESI-MS/MS” *Molecules* **2019**, *24*, 4609.

[83] T. Hamamoto, N. Takata, T. Kudo, K. Horikoshi, “Characteristic presence of polyunsaturated fatty acids in marine psychrophilic vibrios” *FEMS Microbiology Letters* **1995**, *129*, 51–56.

[84] B. Tenchov, E. M. Vescio, G. D. Sprott, M. L. Zeidel, J. C. Mathai, “Salt Tolerance of Archaeal Extremely Halophilic Lipid Membranes*” *Journal of Biological Chemistry* **2006**, *281*, 10016–10023.

[85] M. F. Siliakus, J. van der Oost, S. W. M. Kengen, “Adaptations of archaeal and bacterial membranes to variations in temperature, pH and pressure” *Extremophiles* **2017**, *21*, 651–670.

[86] A. Tamby, J. S. Sinninghe Damsté, L. Villanueva, “Microbial membrane lipid adaptations to high hydrostatic pressure in the marine environment” *Front. Mol. Biosci.* **2023**, *9*, DOI 10.3389/fmolb.2022.1058381.

[87] A. D. Bangham, “Membrane models with phospholipids” *Prog Biophys Mol Biol* **1968**, *18*, 29–95.

[88] A. Laouini, C. Jaafar-Maalej, I. BLOUZA, S. Sfar, C. Charcosset, H. Fessi, “Preparation, Characterization and Applications of Liposomes: State of the Art” *Journal of Colloid Science and Biotechnology* **2012**, *1*, 147–168.

[89] A. D. Bangham, M. W. Hill, N. G. A. Miller in *Methods in Membrane Biology: Volume 1* (Ed.: E.D. Korn), Springer US, Boston, MA, **1974**, pp. 1–68.

[90] J. D. Chodera, D. L. Mobley, "Entropy-Enthalpy Compensation: Role and Ramifications in Biomolecular Ligand Recognition and Design" *Annual Review of Biophysics* **2013**, *42*, 121–142.

[91] T. S. G. Olsson, J. E. Ladbury, W. R. Pitt, M. A. Williams, "Extent of enthalpy–entropy compensation in protein–ligand interactions" *Protein Science* **2011**, *20*, 1607–1618.

[92] F. Peccati, G. Jiménez-Osés, "Enthalpy–Entropy Compensation in Biomolecular Recognition: A Computational Perspective" *ACS Omega* **2021**, *6*, 11122–11130.

[93] Y. Zhang, P. S. Cremer, "Chemistry of Hofmeister Anions and Osmolytes" *Annu. Rev. Phys. Chem.* **2010**, *61*, 63–83.

[94] P. Lo Nostro, B. W. Ninham, "Hofmeister Phenomena: An Update on Ion Specificity in Biology" *Chem. Rev.* **2012**, *112*, 2286–2322.

[95] S. Piera-Velázquez, F. Marhuenda-Egea, E. Cadenas, "Increased stability of malate dehydrogenase from Halobacterium salinarum at low salt concentration in reverse micelles" *Extremophiles* **2002**, *6*, 407–412.

[96] E. Dušeková, K. Garajová, R. Yavaşer, R. Varhač, E. Sedlák, "Hofmeister effect on catalytic properties of chymotrypsin is substrate-dependent" *Biophysical Chemistry* **2018**, *243*, 8–16.

[97] S. Gault, C. S. Cockell, "Perchlorate Salts Exert a Dominant, Deleterious Effect on the Structure, Stability, and Activity of α-Chymotrypsin" *Astrobiology* **2021**, *21*, 405–412.

[98] S. Gault, M. W. Jaworek, R. Winter, C. S. Cockell, "High pressures increase α-chymotrypsin enzyme activity under perchlorate stress" *Commun Biol* **2020**, *3*, 1–9.

[99] C. Vieille, G. J. Zeikus, “Hyperthermophilic Enzymes: Sources, Uses, and Molecular Mechanisms for Thermostability” *Microbiology and Molecular Biology Reviews* **2001**, *65*, 1–43.

[100] S. Srimathi, G. Jayaraman, G. Feller, B. Danielsson, P. R. Narayanan, “Intrinsic halotolerance of the psychrophilic α-amylase from Pseudoalteromonas haloplanktis” *Extremophiles* **2007**, *11*, 505–515.

[101] R. Oliva, N. Jahmidi-Azizi, S. Mukherjee, R. Winter, “Harnessing Pressure Modulation for Exploring Ligand Binding Reactions in Cosolvent Solutions” *J. Phys. Chem. B* **2021**, *125*, 539–546.

[102] N. Jahmidi-Azizi, R. Oliva, S. Gault, C. S. Cockell, R. Winter, “The Effects of Temperature and Pressure on Protein-Ligand Binding in the Presence of Mars-Relevant Salts” *Biology* **2021**, *10*, 687.

[103] T. Ichiye, “Enzymes from piezophiles” *Seminars in Cell & Developmental Biology* **2018**, *84*, 138–146.

[104] H. Frauenfelder, G. Chen, J. Berendzen, P. W. Fenimore, H. Jansson, B. H. McMahon, I. R. Stroe, J. Swenson, R. D. Young, “A unified model of protein dynamics” *Proceedings of the National Academy of Sciences* **2009**, *106*, 5129–5134.

[105] A. F. Mason, N. A. Yewdall, P. L. W. Welzen, J. Shao, M. van Stevendaal, J. C. M. van Hest, D. S. Williams, L. K. E. A. Abdelmohsen, “Mimicking Cellular Compartmentalization in a Hierarchical Protocell through Spontaneous Spatial Organization” *ACS Cent. Sci.* **2019**, *5*, 1360–1365.

[106] R. Saha, J. A. Choi, I. A. Chen, “Protocell Effects on RNA Folding, Function, and Evolution” *Acc. Chem. Res.* **2024**, *57*, 2058–2066.

[107] A. J. Dzieciol, S. Mann, “Designs for life: protocell models in the laboratory” *Chemical Society Reviews* **2012**, *41*, 79–85.

[108] K. Spustova, E. S. Koksal, A. Ainla, I. Gozen, “Subcompartmentalization and Pseudo-Division of Model Protocells” *Biophysical Journal* **2021**, *120*, 101a.

[109] J. Li, L. Jiang, H. Wu, Y. Zou, S. Zhu, Y. Huang, X. Hu, H. Bai, Y. Li, Y. Zou, S. Ding, W. Cheng, “Self-contained G-quadruplex/hemin DNAzyme: a superior ready-made catalyst for in situ imaging analysis” *Nucleic Acids Res* **2025**, *53*, gkaf227.

[110] W. Gilbert, “Origin of life: The RNA world” *Nature* **1986**, *319*, 618–618.

[111] P. G. Higgs, N. Lehman, “The RNA World: molecular cooperation at the origins of life” *Nat Rev Genet* **2015**, *16*, 7–17.

[112] K. Kruger, P. J. Grabowski, A. J. Zaug, J. Sands, D. E. Gottschling, T. R. Cech, “Self-splicing RNA: Autoexcision and autocyclization of the ribosomal RNA intervening sequence of tetrahymena” *Cell* **1982**, *31*, 147–157.

[113] P. Nissen, J. Hansen, N. Ban, P. B. Moore, T. A. Steitz, “The Structural Basis of Ribosome Activity in Peptide Bond Synthesis” *Science* **2000**, *289*, 920–930.

[114] A. Wochner, J. Attwater, A. Coulson, P. Holliger, “Ribozyme-Catalyzed Transcription of an Active Ribozyme” *Science* **2011**, *332*, 209–212.

[115] M. W. Powner, B. Gerland, J. D. Sutherland, “Synthesis of activated pyrimidine ribonucleotides in prebiotically plausible conditions” *Nature* **2009**, *459*, 239–242.

[116] J. P. Ferris, “Montmorillonite-catalysed formation of RNA oligomers: the possible role of catalysis in the origins of life” *Philosophical Transactions of the Royal Society B: Biological Sciences* **2006**, *361*, 1777–1786.

[117] N. V. Hud, B. J. Cafferty, R. Krishnamurthy, L. D. Williams, “The Origin of RNA and ‘My Grandfather’s Axe’” *Chemistry & Biology* **2013**, *20*, 466–474.

[118] B. Kankia, “Quadruplex World” *Orig Life Evol Biosph* **2021**, *51*, 273–286.

[119] A. N. Lane, J. B. Chaires, R. D. Gray, J. O. Trent, “Stability and kinetics of G-quadruplex structures” *Nucleic Acids Res* **2008**, *36*, 5482–5515.

[120] G. Fracchioni, S. Vailati, M. Grazioli, V. Pirota, “Structural Unfolding of G-Quadruplexes: From Small Molecules to Antisense Strategies” *Molecules* **2024**, *29*, 3488.

[121] T. Czerniak, J. P. Saenz, “Lipid membranes modulate the activity of RNA through sequence-dependent interactions” *Proceedings of the National Academy of Sciences* **2022**, *119*, e2119235119.

[122] N. Kundu, D. Mondal, N. Sarkar, “Dynamics of the vesicles composed of fatty acids and other amphiphile mixtures: unveiling the role of fatty acids as a model protocell membrane” *Biophys Rev* **2020**, *12*, 1117–1131.

[123] J. P. Schrum, T. F. Zhu, J. W. Szostak, “The Origins of Cellular Life” *Cold Spring Harb Perspect Biol* **2010**, *2*, a002212.

[124] S. Chatterjee, S. Yadav, “The Coevolution of Biomolecules and Prebiotic Information Systems in the Origin of Life: A Visualization Model for Assembling the First Gene” *Life* **2022**, *12*, 834.

[125] D. Deamer, “The Role of Lipid Membranes in Life’s Origin” *Life* **2017**, *7*, 5.

[126] W. Wang, D. S. Arias, M. Deserno, X. Ren, R. E. Taylor, “Emerging applications at the interface of DNA nanotechnology and cellular membranes: Perspectives from biology, engineering, and physics” *APL Bioeng.* **2020**, *4*, 041507.

[127] G. Wolff, C. E. Melia, E. J. Snijder, M. Bárcena, “Double-Membrane Vesicles as Platforms for Viral Replication” *Trends in Microbiology* **2020**, *28*, 1022–1033.

[128] A. Michanek, N. Kristen, F. Höök, T. Nylander, E. Sparr, “RNA and DNA interactions with zwitterionic and charged lipid membranes — A DSC and QCM-D study” *Biochimica et Biophysica Acta (BBA) - Biomembranes* **2010**, *1798*, 829–838.

[129] A. Khvorova, Y.-G. Kwak, M. Tamkun, I. Majerfeld, M. Yarus, “RNAs that bind and change the permeability of phospholipid membranes” *Proceedings of the National Academy of Sciences* **1999**, *96*, 10649–10654.

[130] D. Morzy, R. Rubio-Sánchez, H. Joshi, A. Aksimentiev, L. Di Michele, U. F. Keyser, “Cations Regulate Membrane Attachment and Functionality of DNA Nanostructures” *J. Am. Chem. Soc.* **2021**, *143*, 7358–7367.

[131] S. Pannwitt, K. Slama, F. Depoix, M. Helm, D. Schneider, “Against Expectations: Unassisted RNA Adsorption onto Negatively Charged Lipid Bilayers” *Langmuir* **2019**, *35*, 14704–14711.

[132] R. C. Monsen, J. O. Trent, J. B. Chaires, “G-quadruplex DNA: A Longer Story” *Acc. Chem. Res.* **2022**, *55*, 3242–3252.

[133] A. Sigel, H. Sigel, R. K. O. Sigel, Eds. , *The Alkali Metal Ions: Their Role for Life*, Springer International Publishing, Cham, **2016**.

[134] J. Gu, J. Leszczynski, “Origin of Na+/K+ Selectivity of the Guanine Tetraplexes in Water: The Theoretical Rationale” *J. Phys. Chem. A* **2002**, *106*, 529–532.

[135] Y. Ma, K. Iida, K. Nagasawa, “Topologies of G-quadruplex: Biological functions and regulation by ligands” *Biochemical and Biophysical Research Communications* **2020**, *531*, 3–17.

[136] D. Bhattacharyya, G. Mirihana Arachchilage, S. Basu, “Metal Cations in G-Quadruplex Folding and Stability” *Front. Chem.* **2016**, *4*, DOI 10.3389/fchem.2016.00038.

[137] A. K. Todd, M. Johnston, S. Neidle, “Highly prevalent putative quadruplex sequence motifs in human DNA” *Nucleic Acids Res* **2005**, *33*, 2901–2907.

[138] C. J. Lech, B. Heddi, A. T. Phan, “Guanine base stacking in G-quadruplex nucleic acids” *Nucleic Acids Res* **2013**, *41*, 2034–2046.

[139] A. Ambrus, D. Chen, J. Dai, R. A. Jones, D. Yang, “Solution Structure of the Biologically Relevant G-Quadruplex Element in the Human c-MYC Promoter. Implications for G-Quadruplex Stabilization” *Biochemistry* **2005**, *44*, 2048–2058.

[140] D. Yang, L. H. Hurley, “Structure of the Biologically Relevant G-Quadruplex in The c-MYC Promoter” *Nucleosides, Nucleotides & Nucleic Acids* **2006**, *25*, 951–968.

[141] M. M. Fay, S. M. Lyons, P. Ivanov, “RNA G-Quadruplexes in Biology: Principles and Molecular Mechanisms” *Journal of Molecular Biology* **2017**, *429*, 2127–2147.

[142] A. N. Lane, “The stability of intramolecular DNA G-quadruplexes compared with other macromolecules” *Biochimie* **2012**, *94*, 277–286.

[143] S. M. Clifford, J. Lasue, E. Heggy, J. Boisson, P. McGovern, M. D. Max, “Depth of the Martian cryosphere: Revised estimates and implications for the existence and detection of subpermafrost groundwater” *Journal of Geophysical Research: Planets* **2010**, *115*, DOI 10.1029/2009JE003462.

[144] R. Orosei, S. E. Lauro, E. Pettinelli, A. Cicchetti, M. Coradini, B. Cosciotti, F. Di Paolo, E. Flamini, E. Mattei, M. Pajola, F. Soldovieri, M. Cartacci, F. Cassenti, A. Frigeri, S. Giuppi, R. Martufi, A. Masdea, G. Mitri, C. Nenna, R. Noschese, M. Restano, R. Seu, “Radar evidence of subglacial liquid water on Mars” *Science* **2018**, *361*, 490–493.

[145] G. L. Jendrasiak, R. Smith, A. A. Ribeiro, "Chaotropic anion-phosphatidylcholine membrane interactions: an ultra high field NMR study" *Biochimica et Biophysica Acta (BBA) - Biomembranes* **1993**, *1145*, 25–32.

[146] M. Fragata, F. Bellemare, E. K. Nénonéné, "Mg(II) Adsorption to a Phosphatidylglycerol Model Membrane Studied by Atomic Absorption and FT-IR Spectroscopy" *J. Phys. Chem. B* **1997**, *101*, 1916–1921.

[147] T. Parasassi, G. De Stasio, A. d'Ubaldo, E. Gratton, "Phase fluctuation in phospholipid membranes revealed by Laurdan fluorescence" *Biophysical Journal* **1990**, *57*, 1179–1186.

[148] S. Lenton, N. H. Rhys, J. J. Towey, A. K. Soper, L. Dougan, "Highly compressed water structure observed in a perchlorate aqueous solution" *Nat Commun* **2017**, *8*, 919.

[149] S. Kriegler, M. Herzog, R. Oliva, S. Gault, C. S. Cockell, R. Winter, "Structural responses of model biomembranes to Mars-relevant salts" *Phys. Chem. Chem. Phys.* **2021**, *23*, 14212–14223.

[150] S. Suladze, S. Cinar, B. Sperlich, R. Winter, "Pressure Modulation of the Enzymatic Activity of Phospholipase A2, A Putative Membrane-Associated Pressure Sensor" *J. Am. Chem. Soc.* **2015**, *137*, 12588–12596.

[151] T. Parasassi, E. Gratton, "Membrane lipid domains and dynamics as detected by Laurdan fluorescence" *J Fluoresc* **1995**, *5*, 59–69.

[152] R. Winter, C. Jeworrek, "Effect of pressure on membranes" *Soft Matter* **2009**, *5*, 3157–3173.

[153] P. Garidel, A. Blume, "Miscibility of phosphatidylethanolamine-phosphatidylglycerol mixtures as a function of pH and acyl chain length" *Eur Biophys J* **2000**, *28*, 629–638.

[154] R. Gaglione, G. Smaldone, A. Cesaro, M. Rumolo, M. De Luca, R. Di Girolamo, L. Petraccone, P. Del Vecchio, R. Oliva, E. Notomista, E. Pedone, A.

Arciello, “Impact of a Single Point Mutation on the Antimicrobial and Fibrillogenic Properties of Cryptides from Human Apolipoprotein B” *Pharmaceuticals* **2021**, *14*, 631.

[155] B. Gironi, R. Oliva, L. Petraccone, M. Paolantoni, A. Morresi, P. Del Vecchio, P. Sassi, “Solvation properties of raft-like model membranes” *Biochimica et Biophysica Acta (BBA) - Biomembranes* **2019**, *1861*, 183052.

[156] R. Bartucci, S. Belsito, L. Sportelli, “Neutral lipid bilayers interacting with chaotropic anions” *Chemistry and Physics of Lipids* **1996**, *79*, 171–180.

[157] W. Patrick Williams, B. A. Cunningham, D. H. Wolfe, G. E. Derbyshire, G. R. Mant, W. Bras, “A combined SAXS/WAXS investigation of the phase behaviour of di-polyenoic membrane lipids” *Biochimica et Biophysica Acta (BBA) - Biomembranes* **1996**, *1284*, 86–96.

[158] J. Castro-Amorim, A. Novo De Oliveira, S. L. Da Silva, A. M. Soares, A. K. Mukherjee, M. J. Ramos, P. A. Fernandes, “Catalytically Active Snake Venom PLA $_2$ Enzymes: An Overview of Its Elusive Mechanisms of Reaction: Miniperspective” *J. Med. Chem.* **2023**, *66*, 5364–5376.

[159] J. E. Burke, E. A. Dennis, “Phospholipase A2 Biochemistry” *Cardiovasc Drugs Ther* **2009**, *23*, 49–59.

[160] R. H. Schaloske, E. A. Dennis, “The phospholipase A2 superfamily and its group numbering system” *Biochimica et Biophysica Acta (BBA) - Molecular and Cell Biology of Lipids* **2006**, *1761*, 1246–1259.

[161] S. M. Kelly, T. J. Jess, N. C. Price, “How to study proteins by circular dichroism” *Biochimica et Biophysica Acta (BBA) - Proteins and Proteomics* **2005**, *1751*, 119–139.

[162] W. R. Burack, R. L. Biltonen, “Lipid bilayer heterogeneities and modulation of phospholipase A2 activity” *Chemistry and Physics of Lipids* **1994**, *73*, 209–222.

[163] J. C. Wilschut, J. Regts, H. Westenberg, G. Scherphof, “Action of phospholipases A2 on phosphatidylcholine bilayers. Effects of the phase transition, bilayer curvature and structural defects” *Biochimica et Biophysica Acta (BBA) - Biomembranes* **1978**, *508*, 185–196.

[164] B.-Z. Yu, J. Rogers, G. R. Nicol, K. H. Theopold, K. Seshadri, S. Vishweshwara, M. K. Jain, “Catalytic Significance of the Specificity of Divalent Cations as KS* and kcat* Cofactors for Secreted Phospholipase A2” *Biochemistry* **1998**, *37*, 12576–12587.

[165] H. M. Verheij, J. J. Volwerk, E. H. J. M. Jansen, W. C. Puyk, B. W. Dijkstra, J. Drenth, G. H. De Haas, “Methylation of histidine-48 in pancreatic phospholipase A2. Role of histidine and calcium ion in the catalytic mechanism” *Biochemistry* **1980**, *19*, 743–750.

[166] A. S. Alekseeva, P. E. Volynsky, I. A. Boldyrev, “Estimation of the Phospholipase A2 Selectivity on POPC/POPG Membranes Using the Interaction Map” *Biochem. Moscow Suppl. Ser. A* **2021**, *15*, 329–333.

[167] J. C. Warren, S. G. Cheatum, “Effect of Neutral Salts on Enzyme Activity and Structure*” *Biochemistry* **1966**, *5*, 1702–1707.

[168] A. F. A. Soudi, O. Farhat, F. Chen, B. C. Clark, M. A. Schneegurt, “Bacterial growth tolerance to concentrations of chlorate and perchlorate salts relevant to Mars” *International Journal of Astrobiology* **2017**, *16*, 229–235.

[169] R. M. Cesur, I. M. Ansari, F. Chen, B. C. Clark, M. A. Schneegurt, “Bacterial Growth in Brines Formed by the Deliquescence of Salts Relevant to Cold Arid Worlds” *Astrobiology* **2022**, *22*, 104–115.

[170] R. Oliva, R. Winter, “Harnessing Pressure-Axis Experiments to Explore Volume Fluctuations, Conformational Substates, and Solvation of Biomolecular Systems” *J. Phys. Chem. Lett.* **2022**, *13*, 12099–12115.

[171] R. Oliva, S. Banerjee, H. Cinar, R. Winter, “Modulation of enzymatic activity by aqueous two-phase systems and pressure – rivalry between kinetic constants” *Chemical Communications* **2020**, *56*, 395–398.

[172] R. Winter, “Interrogating the Structural Dynamics and Energetics of Biomolecular Systems with Pressure Modulation” *Annual Review of Biophysics* **2019**, *48*, 441–463.

[173] C.-C. Wei, D. Jensen, T. Boyle, L. C. O’Brien, C. De Meo, N. Shabestary, D. J. Eder, “Isothermal Titration Calorimetry and Macromolecular Visualization for the Interaction of Lysozyme and Its Inhibitors” *J. Chem. Educ.* **2015**, *92*, 1552–1556.

[174] J. C. Cheetham, P. J. Artymiuk, D. C. Phillips, “Refinement of an enzyme complex with inhibitor bound at partial occupancy: Hen egg-white lysozyme and tri-N-acetylchitotriose at 1.75 Å resolution” *Journal of Molecular Biology* **1992**, *224*, 613–628.

[175] J. F. Darby, A. P. Hopkins, S. Shimizu, S. M. Roberts, J. A. Brannigan, J. P. Turkenburg, G. H. Thomas, R. E. Hubbard, M. Fischer, “Water Networks Can Determine the Affinity of Ligand Binding to Proteins” *J. Am. Chem. Soc.* **2019**, *141*, 15818–15826.

[176] N. Ahalawat, S. Bandyopadhyay, J. Mondal, “On the role of solvent in hydrophobic cavity–ligand recognition kinetics” *J. Chem. Phys.* **2020**, *152*, 074104.

[177] J.-P. Bibring, Y. Langevin, J. F. Mustard, F. Poulet, R. Arvidson, A. Gendrin, B. Gondet, N. Mangold, P. Pinet, F. Forget, M. Berthé, J.-P. Bibring, A. Gendrin, C. Gomez, B. Gondet, D. Jouglet, F. Poulet, A. Soufflot, M. Vincendon, M. Combes, P. Drossart, T. Encrenaz, T. Fouchet, R. Merchiorri, G. Belluci, F. Altieri, V. Formisano, F. Capaccioni, P. Cerroni, A. Coradini, S. Fonti, O. Korablev, V. Kottsov, N. Ignatiev, V. Moroz, D. Titov, L. Zasova, D. Loiseau, N. Mangold, P. Pinet, S. Douté, B. Schmitt, C. Sotin, E. Hauber, H. Hoffmann, R. Jaumann, U. Keller, R. Arvidson, J. F. Mustard, T. Duxbury, F. Forget, G.

Neukum, “Global Mineralogical and Aqueous Mars History Derived from OMEGA/Mars Express Data” *Science* **2006**, *312*, 400–404.

[178] E. G. Rivera-Valentín, V. F. Chevrier, A. Soto, G. Martínez, “Distribution and habitability of (meta)stable brines on present-day Mars” *Nat Astron* **2020**, *4*, 756–761.

[179] R. Oliva, L. Ostermeier, M. W. Jaworek, P. Del Vecchio, N. Gajardo-Parra, E. Cea-Klapp, C. Held, L. Petraccone, R. Winter, “Modulation of protein-saccharide interactions by deep-sea osmolytes under high pressure stress” *International Journal of Biological Macromolecules* **2024**, *255*, 128119.

[180] R. Oliva, M. Niccoli, G. Castronuovo, “Binding and stability properties of PEG2000 to globular proteins: The case of lysozyme” *Journal of Molecular Liquids* **2022**, *360*, 119514.

[181] S. Gault, F. Fonseca, C. S. Cockell, “Preservation of Bacillus subtilis’ cellular liquid state at deep sub-zero temperatures in perchlorate brines” *Commun Biol* **2024**, *7*, 588.

[182] C. Martínez Mir, P. Pisterzi, I. De Poorter, M. Rilou, M. van Kranenburg, B. Heijs, A. Alemany, F. Sage, N. Geijsen, “Spatial multi-omics in whole skeletal muscle reveals complex tissue architecture” *Commun Biol* **2024**, *7*, 1272.

[183] A. D. Bravenec, D. C. Catling, “Effect of Concentration, Cooling, and Warming Rates on Glass Transition Temperatures for NaClO4, Ca(ClO4)2, and Mg(ClO4)2 Brines with Relevance to Mars and Other Cold Bodies” *ACS Earth Space Chem.* **2023**, *7*, 1433–1445.

[184] S. W. Squyres, J. P. Grotzinger, R. E. Arvidson, J. F. Bell, W. Calvin, P. R. Christensen, B. C. Clark, J. A. Crisp, W. H. Farrand, K. E. Herkenhoff, J. R. Johnson, G. Klingelhöfer, A. H. Knoll, S. M. McLennan, H. Y. McSween, R. V. Morris, J. W. Rice, R. Rieder, L. A. Soderblom, “In Situ Evidence for an Ancient Aqueous Environment at Meridiani Planum, Mars” *Science* **2004**, *306*, 1709–1714.

[185] S. J. Chipera, D. T. Vaniman, E. B. Rampe, T. F. Bristow, G. Martínez, V. M. Tu, T. S. Peretyazhko, A. S. Yen, R. Gellert, J. A. Berger, W. Rapin, R. V. Morris, D. W. Ming, L. M. Thompson, S. Simpson, C. N. Achilles, B. Tutolo, R. T. Downs, A. A. Fraeman, E. Fischer, D. F. Blake, A. H. Treiman, S. M. Morrison, M. T. Thorpe, S. Gupta, W. E. Dietrich, G. Downs, N. Castle, P. I. Craig, D. J. D. Marais, R. M. Hazen, A. R. Vasavada, E. Hausrath, P. Sarrazin, J. P. Grotzinger, "Mineralogical Investigation of Mg-Sulfate at the Canaima Drill Site, Gale Crater, Mars" *Journal of Geophysical Research: Planets* **2023**, *128*, e2023JE008041.

[186] J. Huidobro, J. Aramendia, C. García-Florentino, L. Coloma, I. Población, G. Arana, J. M. Madariaga, "Understanding Sulfate Stability on Mars: A Thermo-Raman Spectroscopy Study" *Astrobiology* **2025**, *25*, 189–200.

[187] M. H. Hecht, S. P. Kounaves, R. C. Quinn, S. J. West, S. M. M. Young, D. W. Ming, D. C. Catling, B. C. Clark, W. V. Boynton, J. Hoffman, L. P. DeFlores, K. Gospodinova, J. Kapit, P. H. Smith, "Detection of Perchlorate and the Soluble Chemistry of Martian Soil at the Phoenix Lander Site" *Science* **2009**, *325*, 64–67.

[188] M. M. Osterloo, V. E. Hamilton, J. L. Bandfield, T. D. Glotch, A. M. Baldridge, P. R. Christensen, L. L. Tornabene, F. S. Anderson, "Chloride-Bearing Materials in the Southern Highlands of Mars" *Science* **2008**, *319*, 1651–1654.

[189] E. K. Leask, B. L. Ehlmann, "Evidence for Deposition of Chloride on Mars From Small-Volume Surface Water Events Into the Late Hesperian-Early Amazonian" *AGU Advances* **2022**, *3*, e2021AV000534.

[190] N. H. Thomas, B. L. Ehlmann, P.-Y. Meslin, W. Rapin, D. E. Anderson, F. Rivera-Hernández, O. Forni, S. Schröder, A. Cousin, N. Mangold, R. Gellert, O. Gasnault, R. C. Wiens, "Mars Science Laboratory Observations of Chloride Salts in Gale Crater, Mars" *Geophysical Research Letters* **2019**, *46*, 10754–10763.

[191] J. S. Kargel, J. Z. Kaye, J. W. Head, G. M. Marion, R. Sassen, J. K. Crowley, O. P. Ballesteros, S. A. Grant, D. L. Hogenboom, "Europa's Crust and

Ocean: Origin, Composition, and the Prospects for Life" *Icarus* **2000**, *148*, 226–265.

[192] W. B. McKinnon, M. E. Zolensky, "Sulfate Content of Europa's Ocean and Shell: Evolutionary Considerations and Some Geological and Astrobiological Implications" *Astrobiology* **2003**, *3*, 879–897.

[193] E. M. Spiers, B. E. Schmidt, "Variable Salinity and Hydrogen Production in Europa's Ocean" *Journal of Geophysical Research: Planets* **2023**, *128*, e2023JE008028.

[194] D. Sieme, N. Rezaei-Ghaleh, "Water dynamics in eutectic solutions of sodium chloride and magnesium sulfate: implications for life in Europa's subsurface ocean and ice shell" *Physical Chemistry Chemical Physics* **2024**, *26*, 105–115.

[195] A. H. Stevens, C. S. Cockell, "The Water Activity of Mars-relevant Multicomponent Brines: The Changing Influence of Perchlorate on Habitability over Time" *Planet. Sci. J.* **2023**, *4*, 6.

[196] G. V. Barbosa-Cánovas, A. J. Fontana, S. J. Schmidt, T. P. Labuza, Eds. , *Water activity in foods: fundamentals and applications*, Wiley-Blackwell, Hoboken, NJ, **2020**.

[197] D. Kessel, "Artifacts in Fluorescence Emission Spectroscopy Related to Wood's Anomaly" *Photochemistry and Photobiology* **1991**, *54*, 481–483.

[198] J. R. Lakowicz, B. R. Masters, "Principles of Fluorescence Spectroscopy, Third Edition" *J. Biomed. Opt.* **2008**, *13*, 029901.

[199] A. Velázquez Campoy, E. Freire, "ITC in the post-genomic era…? Priceless" *Biophysical Chemistry* **2005**, *115*, 115–124.

[200] W. Humphrey, A. Dalke, K. Schulten, "VMD: Visual molecular dynamics" *Journal of Molecular Graphics* **1996**, *14*, 33–38.

[201] I. Son, Y. L. Shek, D. N. Dubins, T. V. Chalikian, “Volumetric Characterization of Tri-N-acetylglucosamine Binding to Lysozyme” *Biochemistry* **2012**, *51*, 5784–5790.

[202] T. Odijk, “Mean-field theory of the interaction of the magnesium ion with biopolymers: the case of lysozyme” *J Biol Phys* **2021**, *47*, 521–528.

[203] J. W. Bye, R. J. Falconer, “Thermal stability of lysozyme as a function of ion concentration: A reappraisal of the relationship between the Hofmeister series and protein stability” *Protein Science* **2013**, *22*, 1563–1570.

[204] L. Medda, M. Monduzzi, A. Salis, “The molecular motion of bovine serum albumin under physiological conditions is ion specific” *Chem. Commun.* **2015**, *51*, 6663–6666.

[205] D. I. Cattoni, S. B. Kaufman, F. L. G. Flecha, “Kinetics and thermodynamics of the interaction of 1-anilino-naphthalene-8-sulfonate with proteins” *Biochimica et Biophysica Acta (BBA) - Proteins and Proteomics* **2009**, *1794*, 1700–1708.

[206] F. Tanaka, L. S. Forster, P. K. Pal, J. A. Rupley, “The circular dichroism of lysozyme.” *Journal of Biological Chemistry* **1975**, *250*, 6977–6982.

[207] G. D. Fasman, Ed. , *Circular Dichroism and the Conformational Analysis of Biomolecules*, Springer US, Boston, MA, **1996**.

[208] M.-C. Bellissent-Funel, A. Hassanali, M. Havenith, R. Henchman, P. Pohl, F. Sterpone, D. van der Spoel, Y. Xu, A. E. Garcia, “Water Determines the Structure and Dynamics of Proteins” *Chem. Rev.* **2016**, *116*, 7673–7697.

[209] J.-F. Chang, K. Phillips, T. Lundbäck, M. Gstaiger, J. E. Ladbury, B. Luisi, “Oct-1 POU and octamer DNA co-operate to recognise the Bob-1 transcription co-activator *via* induced folding1” *Journal of Molecular Biology* **1999**, *288*, 941–952.

[210] M. Bastos, O. Abian, C. M. Johnson, F. Ferreira-da-Silva, S. Vega, A. Jimenez-Alesanco, D. Ortega-Alarcon, A. Velazquez-Campoy, "Isothermal titration calorimetry" *Nat Rev Methods Primers* **2023**, *3*, 1–23.

[211] B. Damer, D. Deamer, "The Hot Spring Hypothesis for an Origin of Life" *Astrobiology* **2020**, *20*, 429–452.

[212] M. P. Robertson, G. F. Joyce, "The Origins of the RNA World" *Cold Spring Harb Perspect Biol* **2012**, *4*, a003608.

[213] G. F. Joyce, "The antiquity of RNA-based evolution" *Nature* **2002**, *418*, 214–221.

[214] Y. Kagaya, Z. Zhang, N. Ibtehaz, X. Wang, T. Nakamura, P. D. Punuru, D. Kihara, "NuFold: end-to-end approach for RNA tertiary structure prediction with flexible nucleobase center representation" *Nat Commun* **2025**, *16*, 881.

[215] V. J. Sahayasheela, H. Sugiyama, "RNA G-quadruplex in functional regulation of noncoding RNA: Challenges and emerging opportunities" *Cell Chemical Biology* **2024**, *31*, 53–70.

[216] S. E. Butcher, A. M. Pyle, "The Molecular Interactions That Stabilize RNA Tertiary Structure: RNA Motifs, Patterns, and Networks" *Acc. Chem. Res.* **2011**, *44*, 1302–1311.

[217] M. Egli, "DNA and RNA Structure" **2022**, DOI 10.1039/9781837671328-00020.

[218] M. Abraham, O. Dror, R. Nussinov, H. J. Wolfson, "Analysis and classification of RNA tertiary structures" *RNA* **2008**, *14*, 2274–2289.

[219] P. Kharel, P. Ivanov, "RNA G-quadruplexes and stress: emerging mechanisms and functions" *Trends in Cell Biology* **2024**, *34*, 771–784.

[220] A. N. Lane, J. B. Chaires, R. D. Gray, J. O. Trent, "Stability and kinetics of G-quadruplex structures" *Nucleic Acids Research* **2008**, *36*, 5482–5515.

[221] D. Bhattacharyya, G. Mirihana Arachchilage, S. Basu, “Metal Cations in G-Quadruplex Folding and Stability” *Front. Chem.* **2016**, *4*, DOI 10.3389/fchem.2016.00038.

[222] H. Guiset Miserachs, D. Donghi, R. Börner, S. Johannsen, R. K. O. Sigel, “Distinct differences in metal ion specificity of RNA and DNA G-quadruplexes” *J Biol Inorg Chem* **2016**, *21*, 975–986.

[223] D. Rhodes, H. J. Lipps, “G-quadruplexes and their regulatory roles in biology” *Nucleic Acids Res* **2015**, *43*, 8627–8637.

[224] V. S. Chambers, G. Marsico, J. M. Boutell, M. Di Antonio, G. P. Smith, S. Balasubramanian, “High-throughput sequencing of DNA G-quadruplex structures in the human genome” *Nat Biotechnol* **2015**, *33*, 877–881.

[225] T. Janas, T. Janas, M. Yarus, “Specific RNA binding to ordered phospholipid bilayers” *Nucleic Acids Res* **2006**, *34*, 2128–2136.

[226] K. Suga, H. Umakoshi, H. Tomita, T. Tanabe, T. Shimanouchi, R. Kuboi, “Liposomes destabilize tRNA during heat stress” *Biotechnology Journal* **2010**, *5*, 526–529.

[227] K. L. Reddy, J. M. Zullo, E. Bertolino, H. Singh, “Transcriptional repression mediated by repositioning of genes to the nuclear lamina” *Nature* **2008**, *452*, 243–247.

[228] A. Michanek, M. Yanez, H. Wacklin, A. Hughes, T. Nylander, E. Sparr, “RNA and DNA Association to Zwitterionic and Charged Monolayers at the Air–Liquid Interface” *Langmuir* **2012**, *28*, 9621–9633.

[229] D. Harries, S. May, A. Ben-Shaul, “Counterion release in membrane–biopolymer interactions” *Soft Matter* **2013**, *9*, 9268–9284.

[230] S. Pramanik, H. Tateishi-Karimata, N. Sugimoto, “Organelle-mimicking liposome dissociates G-quadruplexes and facilitates transcription” *Nucleic Acids Res* **2014**, *42*, 12949–12959.

[231] C. R. Cantor, M. M. Warshaw, H. Shapiro, “Oligonucleotide interactions. III. Circular dichroism studies of the conformation of deoxyoligonucleolides” *Biopolymers* **1970**, *9*, 1059–1077.

[232] A. S. Ladokhin, S. Jayasinghe, S. H. White, “How to Measure and Analyze Tryptophan Fluorescence in Membranes Properly, and Why Bother?” *Analytical Biochemistry* **2000**, *285*, 235–245.

[233] Z. Huang, R. P. Haugland, “Partition coefficients of fluorescent probes with phospholipid membranes” *Biochemical and Biophysical Research Communications* **1991**, *181*, 166–171.

[234] R. del Villar-Guerra, J. O. Trent, J. B. Chaires, “G-Quadruplex Secondary Structure Obtained from Circular Dichroism Spectroscopy” *Angewandte Chemie International Edition* **2018**, *57*, 7171–7175.

[235] M. Campanile, R. Oliva, P. D. Vecchio, R. Winter, L. Petraccone, “The anticancer peptide LL-III binds with nanomolar affinity to human telomeric and cMyc G-quadruplexes” *Chem. Commun.* **2023**, *59*, 6179–6182.

[236] L. D. Hughes, R. J. Rawle, S. G. Boxer, “Choose Your Label Wisely: Water-Soluble Fluorophores Often Interact with Lipid Bilayers” *PLOS ONE* **2014**, *9*, e87649.

[237] M. J. Sarmento, A. Llorente, T. Petan, D. Khnykin, I. Popa, M. Nikolac Perkovic, M. Konjevod, M. Jaganjac, “The expanding organelle lipidomes: current knowledge and challenges” *Cell. Mol. Life Sci.* **2023**, *80*, 237.

[238] R. Dazzoni, C. Buré, E. Morvan, A. Grélard, C. Gounou, J.-M. Schmitter, A. Loquet, B. Larijani, E. J. Dufourc, “Tandem NMR and Mass Spectrometry Analysis of Human Nuclear Membrane Lipids” *Anal. Chem.* **2020**, *92*, 6858–6868.

[239] A. Melcrová, S. Pokorna, S. Pullanchery, M. Kohagen, P. Jurkiewicz, M. Hof, P. Jungwirth, P. S. Cremer, L. Cwiklik, “The complex nature of calcium cation interactions with phospholipid bilayers” *Sci Rep* **2016**, *6*, 38035.

[240] S. Matsumoto, H. Tateishi-Karimata, S. Takahashi, T. Ohyama, N. Sugimoto, “Effect of Molecular Crowding on the Stability of RNA G-Quadruplexes with Various Numbers of Quartets and Lengths of Loops” *Biochemistry* **2020**, *59*, 2640–2649.

[241] A. P. Singh, J. Prabhu, S. Vanni, “RNA Order Regulates Its Interactions with Zwitterionic Lipid Bilayers” *Nano Lett.* **2025**, *25*, 77–83.

[242] L. Chen, J. Dickerhoff, S. Sakai, D. Yang, “DNA G-Quadruplex in Human Telomeres and Oncogene Promoters: Structures, Functions, and Small Molecule Targeting” *Acc. Chem. Res.* **2022**, *55*, 2628–2646.

[243] R. Oliva, P. Del Vecchio, M. I. Stellato, A. M. D’Ursi, G. D’Errico, L. Paduano, L. Petraccone, “A thermodynamic signature of lipid segregation in biomembranes induced by a short peptide derived from glycoprotein gp36 of feline immunodeficiency virus” *Biochimica et Biophysica Acta (BBA) - Biomembranes* **2015**, *1848*, 510–517.

[244] R. Oliva, S. Mukherjee, M. Manisegaran, M. Campanile, P. Del Vecchio, L. Petraccone, R. Winter, “Binding Properties of RNA Quadruplex of SARS-CoV-2 to Berberine Compared to Telomeric DNA Quadruplex” *International Journal of Molecular Sciences* **2022**, *23*, 5690.

[245] S. Hadži, J. Lah in *Prokaryotic Gene Regulation: Methods and Protocols* (Eds.: E. Peeters, I. Bervoets), Springer US, New York, NY, **2022**, pp. 239–257.

[246] P. L. Privalov, A. I. Dragan, C. Crane-Robinson, “Interpreting protein/DNA interactions: distinguishing specific from non-specific and electrostatic from non-electrostatic components” *Nucleic Acids Res* **2011**, *39*, 2483–2491.

[247] S. A. Korono, J. F. Nagle, “Closer look at the calorimetric lower transition in lipid bilayers” *Chemistry and Physics of Lipids* **2024**, *259*, 105366.

[248] R. L. Biltonen, D. Lichtenberg, “The use of differential scanning calorimetry as a tool to characterize liposome preparations” *Chemistry and Physics of Lipids* **1993**, *64*, 129–142.

6 List of publications

Publications related to the thesis

- Attila Tortorella, Rosario Oliva, Concetta Giancola, Luigi Petraccone and Roland Winter, Bacterial model membranes under the harsh subsurface conditions of Mars, ***Phys. Chem. Chem. Phys.***, 2024,**26**, 760-769

- Attila Tortorella, Rosario Oliva, Luigi Petraccone, Concetta Giancola, Thermodynamic characterization of lysozyme-NAG3 binding in salt-rich mimetic extraterrestrial environments: Implications for protein function, ***Journal of Molecular Liquids*** 438 (2025) 128720

- Attila Tortorella, Rosario Oliva, Roland Winter, Concetta Giancola, and Luigi Petraccone, RNA and DNA G-quadruplexes interact differently with membranes depending on lipid composition and G-quadruplex topology, ***in preparation***

Publications non related to the thesis

- Attila Tortorella, Linda Leone, Angelina Lombardi, Elio Pizzo, Andrea Bosso, Roland Winter, Luigi Petraccone, Pompea Del Vecchio & Rosario Oliva, The impact of N-glycosylation on the properties of the antimicrobial peptide LL-III, ***Scientific Reports*** volume 13, Article number: 3733 (2023)
- Attila Tortorella and Giuseppe Graziano, Molecular-Scale Liquid Density Fluctuations and Cavity Thermodynamics, ***Entropy*** 2024, 26(8), 620
- Attila Tortorella, and Giuseppe Graziano, A van der Waals Model of Solvation Thermodynamics, ***Entropy*** 2024, 26(8), 714
- Ilaria Di Donato, Attila Tortorella, Marco Campanile, Andreas Rumpel, Linda Leone, Andrea Bosso, Luigi Petraccone, Angelina Lombardi, Roland Winter, Pompea Del Vecchio and Rosario Oliva, Preserving antimicrobial efficacy while extending peptide longevity: effects of residue glycosylation, ***Archives of Biochemistry and Biophysics*** 771 (2025) 110526